國 立 交 通 大 學

電 子 物 理 研 究 所

碩　士　論　文

Sideband 的不對稱性與電子在雙頻率調變下的量子傳輸特性

Sideband Asymmetry Characteristics and Dual-frequency Modulation on a Quantum Dot

研 究 生：黃宇廷

指導教授：朱仲夏

中華民國 九十四年 七月

Sideband 的不對稱性與電子在雙頻率調變下的量子傳輸特性

Sideband Asymmetry Characteristics and Dual-frequency Modulation on a Quantum Dot

研 究 生：黃宇廷　　Student: Yu-Ting Huang

指導教授：朱仲夏　　Advisor: Chon-Saar Chu

國立交通大學
電子物理研究所
碩士論文

A Dissertation
Submitted to Institute of Electrophysics
College of Science
National Chiao Tung University
in Partial Fulfillment of the Requirements
for the Degree of
Master of Science
in
Electrophysics
July 2005
Hsinchu, Taiwan, Republic of China

中華民國 九十四年 七月

Sideband 的不對稱性與電子在雙頻率調變下的量子傳輸特性

研究生：黃宇廷　　指導教授：朱仲夏

國立交通大學電子物理研究所

摘要

電子穿透在一維窄通道裡面受到時變電場影響的量子點時，喜好藉由吸收光子到達量子點的共振態，並且藉由此共振態穿透量子點。在這個研究裡面，我們利用兩個不隨時間變化的靜態位能障來模擬我們的量子點，並且提出了單-光子的方法來計算 sideband 的不對稱性。單-光子的方法精確的估算了電子在窄通道裡對量子點的穿透，並且我們從這個方法得到了清楚的物理圖像，也因此了解 sideband 不對稱的由來。我們也在窄通道裡面也嘗試了不同的物理結構。不同的結構左右兩邊的電子對系統的穿透有很大的差異性。另外，我們探討量子點在雙頻率的電場調變之下，電子對它所產生的穿透特性。我們並且注意到量子點的共振能階會因為時變電場偏壓的影響而產生漂移的現象，我們也因此模擬了幾個不同情況的量子點，探討共振能階漂移的現象。最後我們計算了系統在時變電場的調變之下所產生的淨電流。

Sideband Asymmetry Characteristics and Dual-frequency Modulation on a Quantum Dot

Student: Yu-Ting Huang Advisor: Chon-Saar Chu

Department of Electrophysics

National Chiao-Tung University

Abstract

Electrons are apt to make transition through the quantum dot by absorbing photons. We model our quantum dot with double static delta-profile barriers, and we study sideband asymmetry features through the quantum dot. We then propose one-photon approximation which gives concrete physical pictures for the main transport process, and successfully depicts this phenomenon of asymmetric sidebands. We also study quantum transport under different configurations. Quantum transport characteristics are much different for electrons incident from the opposite sides of the system in barrier-well configuration. Then we demonstrate transport characteristics under dual-frequency modulation and the pumped current. Shifting of resonance states under time-dependent modulation is also studied within our work.

Acknowledgement

在這兩年的研究所生涯裡，特別感謝朱老師的指導，以及唐志雄、王律堯、鄔其君學長與鍾淑維學姐熱心的協助，讓我除了在物理的領域獲得更多的知識以外，對於為人處世的態度亦獲益良多；另外，也要感謝實驗室同學們與蔡佩芸的扶持與關照，讓這些日子更增添了色彩。最後，也感謝陪伴我這麼多年的家人一路走來給我的支持。

Contents

List of Figures

Chapter 1
Introduction

In mesoscopic physics, time-dependent quantum transport has been an active field in recent years. These studies focus on coherent inelastic scattering. Electrons in mesoscopic regime possess a sufficient long phase-coherent length compared to the dimension of the structure we study, thus phase become of much important to the transport properties in this regime. Among the structures being studied, quantum point contact (QPC) is the most popular one for its simplicity. Many other devices such as "electron waveguide", "quantum dot"…etc. are based on this structure.

QPCs can be formed by applying negative bias on the split metal gates that are fabricated the top of a GaAs-Al_xGa_{1-x} hetrostructure, and its width can be controlled by the biasing electrode. Due to the fabrication technologies, nearly perfect two-dimensional electron gas (2DEG) of sufficient long phase-coherent length is formed in the hetrostructure, making possible the measurement of experiments.

Study of transport properties in mesoscopic scale is first proposed by Landauer [1-3], and then Büttiker gave a more general formulism based on Landauer's theory [4-6]. Landauer- Büttiker formulation successfully explained quite a number of results of mesoscopic experiments. Landauer- Büttiker formulism thus becomes one of the most important theories in mesoscopic physics.

Adiabatic quantum pumping (AQP) also attracts much attention in recent years. The idea was firstly proposed by Thouless [7], and then Niu [8] proposed several one-dimensional time-dependent potentials for adiabatic quantum pumping. In AQP, finite amount of net charges are transferred through the unbiased system in each cycle of the deformation parameters. Subsequently, Brouwer [9] derived a terse analytical

formulation of AQP. Furthermore, Switkes *et al.* [10] successfully conducted an experiment in confirmation of AQP. They introduce a phase difference into the two metal gates with ac voltage biasing the open quantum dot.

Beyond adiabatic regime, the importance of nonadiabatic quantum charge pumping has been pointed out. C.S.Tang and C.S. Chu [11] proposed a scattering-matrix method in calculation of nonadiabatic quantum charge pumping under time-dependent modulation. In addition, S.W. Chung *et al.* [12] proposed a new configuration, finger-gate array (FGA), to achieve quantum charge pumping (QCP). A pair of FGAs with finite number of finger-gates is set on the top of a narrow channel. The pair of FGAs is ac biased with a phase difference between each other.

In the beginning, we tried an alternative approach for QCP in a narrow channel. We apply dual-frequency barriers in a narrow channel beyond adiabatic regime to destroy the translational invariance for occurrence of quantum charge pumping, and we also study sideband characteristics of a quantum dot under dual-frequency modulation. We set up our quantum dot by a pair of delta-profile barriers in a one-dimensional narrow channel where the channel, as shown in Fig.1, is acquired by a negatively biased narrow constriction. QCP will be achieved whenever translational invariance is destroyed.

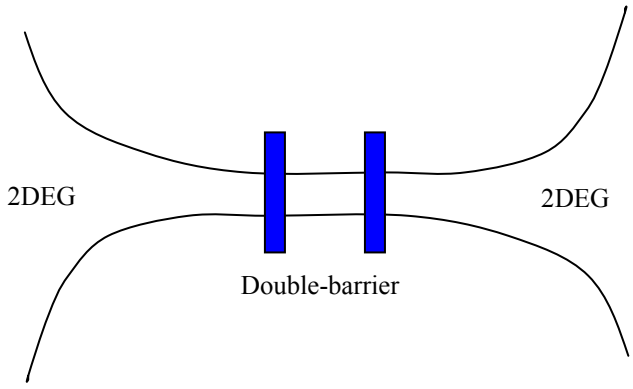

Fig.1. Sketch of the model of our quantum dot.

QCP was achieved by dual-dual frequency modulation, and we also discovered yet another interesting feature of a quantum dot in mono-frequency modulation-sideband asymmetry. Sideband band channels open when ac voltages are applied on the quantum dot, and we find that sideband channels higher than the resonance state are asymmetric to those lower than the resonance state. We might intuitively consider sideband channels to be symmetric for electrons may have the same photon absorption and emission probability, but the asymmetric sideband features give rise to the implication that electrons are more likely to make transition through the quantum dot by absorbing photons than by emitting photons within the scattering process. We then study sideband asymmetry features in our work as well.

We utilized one-sideband approximation method [13] and then we proposed one-photon approximation (OPA) for studying sideband asymmetry. When the amplitude of applied ac potential is not strong, or when the confining double-barrier is comparatively strong, one-sideband approximation gives good numerical results of transport properties. OPA also gives good numerical results compared to exact numerical calculation even when the oscillation amplitudes are strong. Thus, we obtain a clear physical picture for the causes of sideband asymmetry. It is worthy to note that one-sideband approximation can be multi-photon processes, within the energy regime $E - \hbar\Omega < E < E + \hbar\Omega$. However, OPA only allows electrons to absorb or emit a single photon once within the scattering region.

In this work, we give the formulation for exact numerical calculation and derivation of OPA in Ch. 2, and then we give sideband asymmetry characteristics and comparison of OPA with exact numerical calculation in Ch. 3. We also study sideband features of different configurations in Ch. 3. In Ch. 4, we present sideband features of a quantum dot under dual-frequency modulations. Resonance states in the quantum dot are found to shift when ac voltage is applied in a quantum dot; hence we

demonstrate shifting of resonance levels under time-dependent modulation in Ch. 5. Ch. 6 gives the pumped current of dual-frequency modulating quantum dot and mono-frequency modulating barrier-well configuration system. A few unresolved yet interesting results are collected in Ch. 7. Finally, Ch. 8 presents a conclusion.

Chapter 2
Formulation

We start the formulation with time-dependent mode matching approach. For analytical solution, we then do one-sideband approximation, and finally we give the one-photon approximation approach. Schematic sketch of our system is given in Fig. 2.1.

We do the numerical calculations by time-dependent mode matching approach. From the numerical results given in Ch. 3, we found an interesting sideband feature-sideband asymmetry. This contradicts our intuitive prediction. As known from Fermi's golden rule, electrons have the same probability of absorbing or emitting a photon.

In order to further study the causes of sideband asymmetry, we simplify our cases to the regime where one-sideband approximation is sufficient to dominate. It's an inspiration that sideband asymmetry sill exists in such regime.

Finally, to get a clearer physical picture, we further propose the one-photon approximation approach. This comes directly after the simplification of the analytical results from one-sideband approximation. Comparisons of exact numerical calculation with one-photon approximation are given in Sec. 3.5.

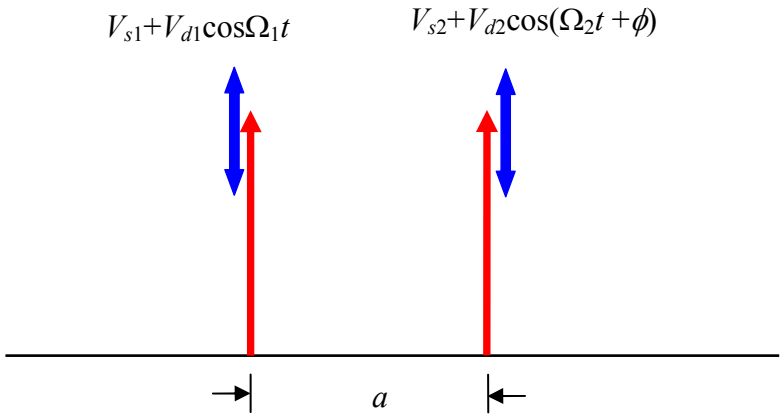

Fig. 2.1. Sketch of the time-dependent model we study.

2.1 Time-dependent Mode Matching Approach

In the system we study, we have the Hamiltonian

$$H=-\frac{\hbar}{2m^*}[\frac{\partial^2}{\partial x^2}+\frac{\partial^2}{\partial y^2}]+V_1\delta(x+\frac{a}{2})+V_2\delta(x-\frac{a}{2})+V_c(y), \tag{2.1}$$

where electrons transport in x-direction, and the y-direction is confined by a parabolic potential.

Furthermore, with the units of energy $E^*=E_F=\frac{\hbar^2k_F^2}{2m^*}=9\text{meV}$, frequency $\Omega^*=\frac{\hbar k_F^2}{m^*}=13.6\text{THz}$, and length $a^*=\frac{1}{k_F}=79.6\text{Å}$, the dimensionless Hamiltonian becomes

$$H=-[\frac{\partial^2}{\partial x^2}+\frac{\partial^2}{\partial y^2}]+V_1\delta(x+\frac{a}{2})+V_2\delta(x-\frac{a}{2})+V_c(y), \tag{2.2}$$

where,

$V_1=V_{s1}+V_{d1}\cos\Omega_1 t$,

$V_2=V_{s2}+V_{d2}\cos(\Omega_2 t+\phi)$,

$\Omega_2=N\Omega_1$ (N is any integer),

$V_c(y)=\omega_y{}^2y^2$.

The total wave function can thus be expressed of the form

$$\psi(\vec{r},t)=\sum_n \phi_n(y)\psi_n(x,t)\,, \tag{2.3}$$

where *n* is the subband index.

For the wavefunction incident from the left in the *n*-th mode with total energy *E*, we define the kinetic energy μ_n along transport direction, and $\mu_n = E-\varepsilon_n$,where $\varepsilon_n=(2n+1)\omega_y$ is the eigen energy due to the parabolic confining potential.

Then the wavefunction in transport direction becomes

$$\psi_n(x,t)=\begin{cases} e^{ik_n(0)x}e^{-i\mu_n(0)t}+\sum_m r_n(m)e^{-ik_n(m)x}e^{-i\mu_n(m)t} & ,x<\dfrac{-a}{2} \\ \sum_m A_n(m)e^{ik_n(m)x}e^{-i\mu_n(m)t}+\sum_m B_n(m)e^{-ik_n(m)x}e^{-i\mu_n(m)t} & ,|x|<\dfrac{a}{2} \\ \sum_m t_n(m)e^{ik_n(m)x}e^{-i\mu_n(m)t} & ,x>\dfrac{a}{2} \end{cases} \tag{2.4}$$

where $k_n(m)=\sqrt{\mu_n(m)}$ and $\mu_n(m)=\mu_n+m\Omega_1$.

In order to calculate the energy dependence of conductance *G*, we start to match the boundary conditions at *x*=–*a*/2. Continuous of ψ_n gives

$$e^{-ik_n(0)\frac{a}{2}}+\sum_m r_n(m)e^{ik_n(m)\frac{a}{2}}e^{-im\Omega_1 t}=\sum_m A_n(m)e^{-ik_n(m)\frac{a}{2}}e^{-im\Omega_1 t}+\sum_m B_n(m)e^{ik_n(m)\frac{a}{2}}e^{-im\Omega_1 t}\,,$$

and the boundary condition for ψ_n' gives

$$\begin{aligned} & k_n(0)e^{-ik_n(0)\frac{a}{2}} \\ & -\sum_m\left(r_n(m)k_n(m)e^{ik_n(m)\frac{a}{2}}+A_n(m)k_n(m)e^{-ik_n(m)\frac{a}{2}}-B_n(m)k_n(m)e^{ik_n(m)\frac{a}{2}}\right)e^{-im\Omega_1 t} \\ & +\frac{1}{i}\sum_m\left(A_n(m)e^{-ik_n(m)\frac{a}{2}}+B_n(m)e^{ik_n(m)\frac{a}{2}}\right)\frac{V_{d1}}{2}(e^{-i(m-1)\Omega_1 t}+e^{-i(m+1)\Omega_1 t}) \\ & +\frac{1}{i}V_{s1}\sum_m\left(A_n(m)e^{-ik_n(m)\frac{a}{2}}+B_n(m)e^{ik_n(m)\frac{a}{2}}\right)e^{-im\Omega_1 t} \\ & =0 \end{aligned}\,.$$

Then we match the boundary conditions at *x*=*a*/2. Continuous of ψ_n gives

$$\sum_m A_n(m)e^{ik_n(m)\frac{a}{2}}e^{-im\Omega_1 t}+\sum_m B_n(m)e^{-ik_n(m)\frac{a}{2}}e^{-im\Omega_1 t}=\sum_m t_n(m)e^{ik_n(m)\frac{a}{2}}e^{-im\Omega_1 t}\,,$$

and continuous of ψ_n' gives

$$\sum_m \left(A_n(m)k_n(m)e^{ik_n(m)\frac{a}{2}} - B_n(m)k_n(m)e^{-ik_n(m)\frac{a}{2}} - t_n(m)k_n(m)e^{ik_n(m)\frac{a}{2}} \right) e^{-im\Omega_1 t}$$
$$+\frac{1}{i}\sum_m \left(A_n(m)e^{ik_n(m)\frac{a}{2}} + B_n(m)e^{-ik_n(m)\frac{a}{2}} \right) \frac{V_{d2}}{2}\left(e^{-i(m-N)\Omega_1 t}e^{i\phi} + e^{-i(m+N)\Omega_1 t}e^{-i\phi} \right)$$
$$+\frac{1}{i}V_{s2}\sum_m \left(A_n(m)e^{ik_n(m)\frac{a}{2}} + B_n(m)e^{-ik_n(m)\frac{a}{2}} \right) e^{-im\Omega_1 t}$$
$$= 0$$

Thus we have the following equations

$$\delta_{m,0}e^{-ik_n\frac{a}{2}} + r_n(m)e^{ik_n(m)\frac{a}{2}} = A_n(m)e^{-ik_n(m)\frac{a}{2}} + B_n(m)e^{ik_n(m)\frac{a}{2}}, \tag{2.5}$$

$$\begin{aligned}
&\delta_{m,0}k_n e^{-ik_n\frac{a}{2}} - r_n(m)k_n(m)e^{ik_n(m)\frac{a}{2}} \\
&-A_n(m)k_n(m)e^{-ik_n(m)\frac{a}{2}} + B_n(m)k_n(m)e^{ik_n(m)\frac{a}{2}} \\
&+\frac{V_{s1}}{i}\left(A_n(m)e^{-ik_n(m)\frac{a}{2}} + B_n(m)e^{ik_n(m)\frac{a}{2}} \right) \\
&+\frac{1}{i}\frac{V_{d1}}{2}\delta_{m',m+1}\left(A_n(m')e^{-ik_n(m')\frac{a}{2}} + B_n(m')e^{ik_n(m')\frac{a}{2}} \right) \\
&+\frac{1}{i}\frac{V_{d1}}{2}\delta_{m',m-1}\left(A_n(m')e^{-ik_n(m')\frac{a}{2}} + B_n(m')e^{ik_n(m')\frac{a}{2}} \right) \\
&= 0
\end{aligned} \tag{2.6}$$

$$A_n(m)e^{ik_n(m)\frac{a}{2}} + B_n(m)e^{-ik_n(m)\frac{a}{2}} = t_n(m)e^{ik_n(m)\frac{a}{2}}, \tag{2.7}$$

and

$$\begin{aligned}
&A_n(m)k_n(m)e^{ik_n(p)\frac{a}{2}} - B_n(m)k_n(m)e^{-ik_n(m)\frac{a}{2}} - t_n(m)k_n(m)e^{ik_n(m)\frac{a}{2}} \\
&+\frac{V_{s2}}{i}\left(A_n(m)e^{ik_n(m)\frac{a}{2}} + B_n(m)e^{-ik_n(m)\frac{a}{2}} \right) \\
&+\frac{1}{i}\frac{V_{d2}}{2}e^{i\phi}\delta_{m',m+N}\left(A_n(m')e^{ik_n(m')\frac{a}{2}} + B_n(m')e^{-ik_n(m')\frac{a}{2}} \right) \\
&+\frac{1}{i}\frac{V_{d2}}{2}e^{-i\phi}\delta_{m',m-N}\left(A_n(m')e^{ik_n(m')\frac{a}{2}} + B_n(m')e^{-ik_n(m')\frac{a}{2}} \right) \\
&= 0
\end{aligned} \tag{2.8}$$

Hence, for the purpose of numerical calculation, we are able to set up the matrix equation

$$\begin{bmatrix} C_1 \\ C_2 \end{bmatrix} = \begin{bmatrix} M_{11} & M_{12} \\ M_{21} & M_{22} \end{bmatrix} \begin{bmatrix} A_n \\ B_n \end{bmatrix}. \tag{2.9}$$

Coefficients of $A_n(m)$ and $B_n(m)$ can be solved by Eq. (2.9). Equation (2.5) and (2.7) gives

$$\begin{aligned} r_n(m) &= A_n(m)e^{-ik_n(m)a} + B_n(m) - \delta_{p,0}e^{-i\left(k_n + k_n(m)\right)\frac{a}{2}} \\ t_n(m) &= A_n(m) + B_n(m)e^{-ik_n(m)a} \end{aligned}. \tag{2.10}$$

Thus, we can set up the matrix equation

$$\begin{bmatrix} r_n \\ t_n \end{bmatrix} = \begin{bmatrix} P_{11} & P_{12} \\ P_{21} & P_{22} \end{bmatrix} \begin{bmatrix} A_n \\ B_n \end{bmatrix} + \begin{bmatrix} D_1 \\ D_2 \end{bmatrix} \tag{2.11}$$

for the numerical calculations of $r_n(m)$ and $t_n(m)$. Details for the set-up of these matrices will be given in Appendix A. Hence, the transmission and reflection coefficient can be solved. Similarly, for electrons incident from the right of the system, $\tilde{t}_n(m)$ and $\tilde{r}_n(m)$ can be solved in the same way. Finally, we can calculate the transmission probability of each sideband channel by the equation

$$T_n(m) = \frac{k_n(m)}{k_n(0)}\left|t_n(m)\right|^2, \tag{2.12}$$

and total current transmission by

$$T_{\rightarrow}(E) = \sum_n \sum_m T_n(m). \tag{2.13}$$

Similarly, for electrons incident from the right,

$$\tilde{T}_n(m) = \frac{k_n(m)}{k_n(0)}\left|\tilde{t}_n(m)\right|^2,$$

and (2.14)

$$T_{\leftarrow}(E) = \sum_n \sum_m \tilde{T}_n(m). \tag{2.15}$$

Total transmission current would be given by the equation

$$I = -\frac{2e}{h}\int_0^{E_f} dE\left[T_{\rightarrow}(E) - T_{\leftarrow}(E)\right], \tag{2.16}$$

where E_f denotes the Fermi-energy.

2.2 One-Sideband Approximation

When the confining barrier is strong, or the oscillating amplitude is comparatively weak, we presume that electrons are only able to make transition through the first sideband. From Fig. 3.6 and 3.7, we can see that one-sideband approximation gives appropriate result. Furthermore, features of sideband asymmetry still exist.

In order to get a clearer physical picture, analytical expressions are necessary. One-sideband approximation here is done in preparation of one-photon approximation of the next section. Thus, we start with an electron scattering with a single time-dependent barrier.

Consider a time-dependent potential $V_I = V_s + V_d\left(\cos\Omega t + \phi\right)$ applied at x=0. We then define $r_m^I(\mu)$ and $t_m^I(\mu)$ as the reflection and transmission coefficients of the electron with kinetic energy μ incident from the left of the barrier; the superscript I specifies the interface (barrier) we're dealing with, and the subscript m is the sideband channel index. Respectively, $\tilde{r}_m^I(\mu)$ and $\tilde{t}_m^I(\mu)$ are the reflection and transmission coefficients of the electron incident from the right.

Total wave function of the electron incident from the left

$$\psi(x,t)=\begin{cases} e^{ik(0)x}e^{-i\mu(0)t}+\sum_{m=-1}^{1} r_m^I(\mu)e^{-ik(m)x}e^{-i\mu(m)t} & ,x<0 \\ \sum_{m=-1}^{1} t_m^I(\mu)e^{ik(m)x}e^{-i\mu(m)t} & ,x>0 \end{cases}, \tag{2.19}$$

where μ is the kinetic energy along transport direction, and

$\mu(m)=\mu+m\Omega$,

$k(m)=\sqrt{\mu(m)}$.

In order to derive the analytical expressions for the reflection and transmission coefficients, we then have to conduct the time-dependent mode matching. Continuous of ψ gives

$$\begin{aligned} &e^{-i\mu(0)t}+r_1^I(\mu)e^{-i\mu(1)t}+r_0^I(\mu)e^{-i\mu(0)t}+r_{-1}^I(\mu)e^{-i\mu(-1)t} \\ &=t_1^I(\mu)e^{-i\mu(1)t}+t_0^I(\mu)e^{-i\mu(0)t}+t_{-1}^I(\mu)e^{-i\mu(-1)t} \end{aligned},$$

and continuous of ψ' gives

$$\begin{aligned} &ik(0)e^{-i\mu(0)t}-i\left[k(1)r_1^I(\mu)e^{-i\mu(1)t}+k(0)r_0^I(\mu)e^{-i\mu(0)t}+k(-1)r_{-1}^I(\mu)e^{-i\mu(-1)t}\right] \\ &-i\left[k(1)t_1^I(\mu)e^{-i\mu(1)t}+k(0)t_0^I(\mu)e^{-i\mu(0)t}+k(-1)t_{-1}^I(\mu)e^{-i\mu(-1)t}\right] \\ &+V_s\left[t_1^I(\mu)e^{-i\mu(1)t}+t_0^I(\mu)e^{-i\mu(0)t}+t_{-1}^I(\mu)e^{-i\mu(-1)t}\right] \\ &+\frac{V_d}{2}e^{i\phi}\left[t_1^I(\mu)e^{-i\mu(0)t}+t_0^I(\mu)e^{-i\mu(-1)t}+t_{-1}^I(\mu)e^{-i\mu(-2)t}\right] \\ &+\frac{V_d}{2}e^{-i\phi}\left[t_1^I(\mu)e^{-i\mu(2)t}+t_0^I(\mu)e^{-i\mu(1)t}+t_{-1}^I(\mu)e^{-i\mu(0)t}\right] \\ &=0 \end{aligned}.$$

Hence, $r_1^I(\mu), r_0^I(\mu), r_{-1}^I(\mu), t_1^I(\mu), t_0^I(\mu)$, and $t_{-1}^I(\mu)$ can be solved analytically. Analytical expressions for these coefficients are given in appendix B. For electrons incident from the right, $\tilde{r}_m^I(\mu)=r_m^I(\mu)$, and $\tilde{t}_m^I(\mu)=t_m^I(\mu)$.

When the potential is applied at interface *II* ($x=a$), the corresponding reflection and transmission coefficients are given in the following equations

$$\begin{cases} r_m^{II}(\mu) = r_m^I(\mu) e^{i[k(m)+k(0)]a} \\ t_m^{II}(\mu) = t_m^I(\mu) e^{-i[k(m)-k(0)]a} \end{cases},$$

and

$$\begin{cases} \tilde{r}_m^{II}(\mu) = r_m^I(\mu) e^{-i[k(m)+k(0)]a} \\ \tilde{t}_m^{II}(\mu) = t_m^I(\mu) e^{i[k(m)-k(0)]a} \end{cases}.$$

Under one-sideband approximation, total transmission would be

$$T_{\rightarrow}(E) = \sum_n \sum_{m=-1}^{1} T_n(m) \tag{2.20}$$

$$T_{\leftarrow}(E) = \sum_n \sum_{m=-1}^{1} \tilde{T}_n(m). \tag{2.21}$$

2.3 One-Photon Approximation

It is worthy to note that one-sideband approximation can be multi-photon processes, while one-photon approximation only allows electrons to absorb or emit a single photon within the scattering process.

In order to acquire a concrete physical picture, we propose the one-photon approximation approach. This comes from the simplification of one-sideband approximation. In Sec. 2.2, we get the analytical expressions of reflection and transmission coefficients of both interface *I* and *II*. V_d^2 in the denominators of the coefficients can be further expanded into series with $(V_d^2)^n$ terms involved. This simply implies that electrons encounter multiple-photon process when scattering with the potentials.

Therefore, for our consideration of one-photon approximation, we omit V_d^2 terms in the denominators or numerators of the coefficients. Hence, the coefficients are related to V_d only, which means that electrons interact with the potential "once." Finally, we deal the transmission of electrons through the double-barrier with

multiple-scattering process between interface *I* and *II*.

After reducing and simplification, the transmission and reflection coefficients become of interface *I* become

$$t_1^I(\mu) = \frac{-ik(0)V_d e^{-i\phi}}{\left[2k(0)+iV_s\right]\left[iV_s+2k(1)\right]}, \tag{2.22}$$

$$t_0^I(\mu) = \frac{2k(0)}{\left[2k(0)+iV_s\right]}, \tag{2.23}$$

$$t_{-1}^I(\mu) = \frac{-ik(0)V_d e^{i\phi}}{\left[2k(0)+iV_s\right]\left[iV_s+2k(-1)\right]}, \tag{2.24}$$

$$r_1^I(\mu) = \frac{-ik(0)V_d e^{-i\phi}}{\left[2k(0)+iV_s\right]\left[iV_s+2k(1)\right]}, \tag{2.25}$$

$$r_0^I(\mu) = \frac{-iV_s}{\left[2k(0)+iV_s\right]}, \tag{2.26}$$

$$r_{-1}^I(\mu) = \frac{-ik(0)V_d e^{i\phi}}{\left[2k(0)+iV_s\right]\left[iV_s+2k(-1)\right]}, \tag{2.27}$$

and $\tilde{r}_m^I(\mu) = r_m^I(\mu)$, and $\tilde{t}_m^I(\mu) = t_m^I(\mu)$.

Similarly, as in Sec. 2.2, coefficients of interface *II* can be obtained by the following equations

$$\begin{cases} r_m^{II}(\mu) = r_m^I(\mu)e^{i[k(m)+k(0)]a} \\ t_m^{II}(\mu) = t_m^I(\mu)e^{-i[k(m)-k(0)]a} \end{cases},$$

and

$$\begin{cases} \tilde{r}_m^{II}(\mu) = r_m^I(\mu)e^{-i[k(m)+k(0)]a} \\ \tilde{t}_m^{II}(\mu) = t_m^I(\mu)e^{i[k(m)-k(0)]a} \end{cases}.$$

We then define $t_1(\mu)$ the transmission coefficient of electrons making transition through the system by means of absorbing a photon. Furthermore, $t_1(\mu)$ can be further

separated into four processes:

$$t_1(\mu) = t\left(t_1^I, \mu\right) + t\left(t_1^{II}, \mu\right) + t\left(\tilde{r}_1^I, \mu\right) + t\left(r_1^{II}, \mu\right) \tag{2.28}$$

The definition of each process in Eq. (2.28) is given by

$t\left(t_1^I, \mu\right)$-transmission absorption at interface *I*,

$t\left(t_1^{II}, \mu\right)$-transmission absorption at interface *II*,

$t\left(\tilde{r}_1^I, \mu\right)$-reflection absorption at interface *I*, and

$t\left(r_1^{II}, \mu\right)$-reflection absorption at interface *II*.

We can express each of the four processes as a sum of infinite series:

$$t\left(t_1^I, \mu\right) = \sum_{n=0}^{\infty} t_1^I(\mu)\left[r_0^{II}(\mu+\Omega)\tilde{r}_0^I(\mu+\Omega)\right]^n t_0^{II}(\mu+\Omega)$$

$$t\left(t_1^{II}, \mu\right) = \sum_{n=0}^{\infty} t_0^I(\mu)\left[r_0^{II}(\mu)\tilde{r}_0^I(\mu)\right]^n t_1^{II}(\mu)$$

$$t\left(\tilde{r}_1^I, \mu\right) = \sum_{m=0}^{\infty}\sum_{n=0}^{\infty} t_0^I(\mu) r_0^{II}(\mu)\left[\tilde{r}_0^I(\mu) r_0^{II}(\mu)\right]^n \tilde{r}_1^I(\mu)\left[r_0^{II}(\mu+\Omega)\tilde{r}_0^I(\mu+\Omega)\right]^m t_0^{II}(\mu+\Omega)$$

$$t\left(r_1^{II}, \mu\right) = \sum_{m=0}^{\infty}\sum_{n=0}^{\infty} t_0^I(\mu)\left[r_0^{II}(\mu)\tilde{r}_0^I(\mu)\right]^n r_1^{II}(\mu)\tilde{r}_0^I(\mu+\Omega)\left[r_0^{II}(\mu+\Omega)\tilde{r}_0^I(\mu+\Omega)\right]^m t_0^{II}(\mu+\Omega)$$

Fig. 2.2 to 2.5 depict the physical picture of the four processes above.

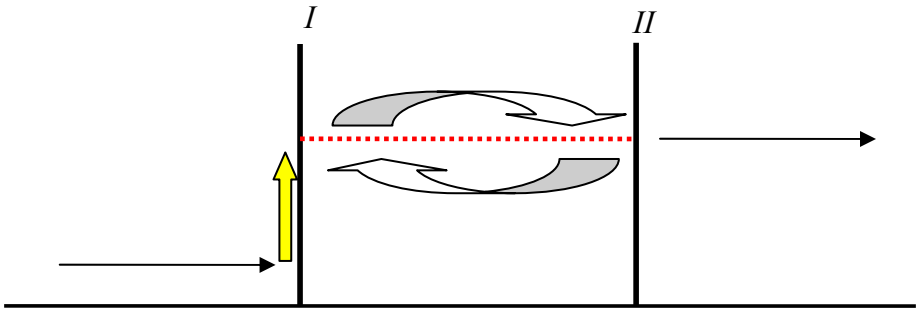

Fig. 2.2. Schematic sketch of $t\left(t_1^I, \mu\right)$. Electrons absorb a photon at interface *I*, and then encounter multiple scattering process before transmitting through interface *II*.

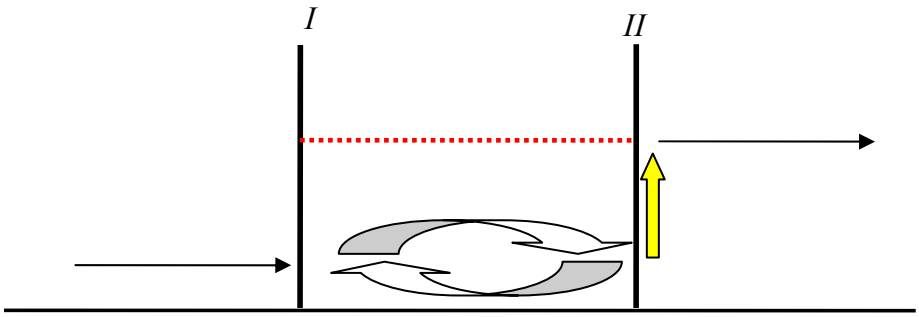

Fig. 2.3. Schematic sketch of $t\left(t_1^{II},\mu\right)$. Electrons tunnel through interface *I* and encounter multiple scattering process between in interface *I* and *II*, and then make transition through interface *II* by transmission absorption.

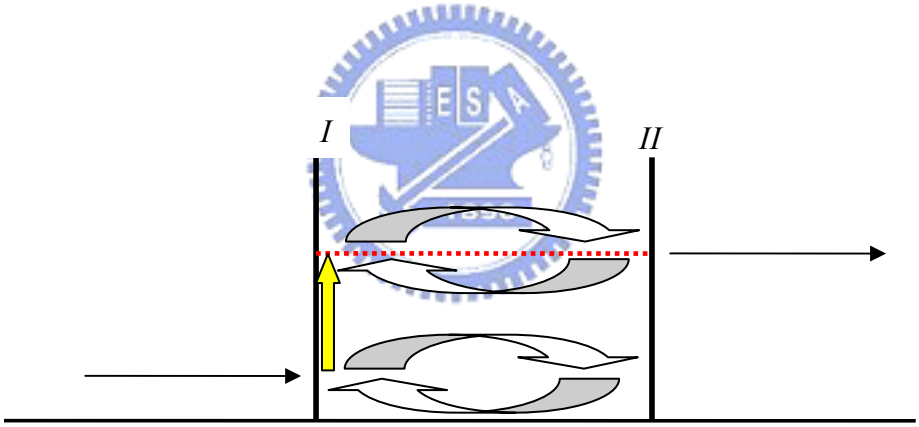

Fig. 2.4. Schematic sketch of $t\left(\tilde{r}_1^{I},\mu\right)$. Electrons tunnel through interface *I* and have multiple scattering process between interface *I* and *II*. Then they absorb a photon by reflection absorption at interface *I*, and then they make transition through interface *II* after the multiple scattering process at the resonance state.

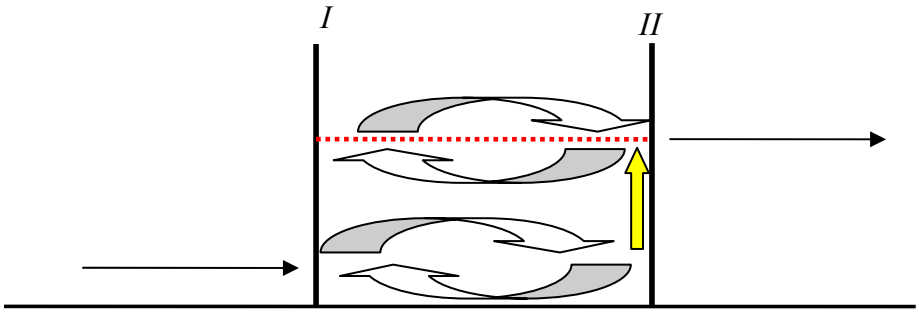

Fig. 2.5. Schematic sketch of $t\left(r_1^{II},\mu\right)$. Electrons tunnel through interface *I*, having a multiple scattering process, and then absorb a photon by reflection absorption at interface *II*. Finally, they make transition through interface *II* after the multiple scattering process at the resonance state.

Similarly, we can define $t_{-1}(\mu)$ the transmission coefficient of electrons making transition through the system by emitting a single photon:

$$t_{-1}\left(\mu\right)=t\left(t_{-1}^{I},\mu\right)+t\left(t_{-1}^{II},\mu\right)+t\left(\tilde{r}_{-1}^{I},\mu\right)+t\left(r_{-1}^{II},\mu\right). \tag{2.29}$$

The definition of each term in Eq. (2.29) is given as

$t\left(t_{-1}^{I},\mu\right)$-transmission emission at interface *I*,

$t\left(t_{-1}^{II},\mu\right)$-transmission emission at interface *II*,

$t\left(\tilde{r}_{-1}^{I},\mu\right)$-reflection emission at interface *I*, and

$t\left(r_{-1}^{II},\mu\right)$-reflection emission at interface *II*.

Expressed with sum of infinite series, the four processes become

$$t\left(t_{-1}^{I},\mu\right)=\sum_{n=0}^{\infty}t_{-1}^{I}\left(\mu\right)\left[r_{0}^{II}\left(\mu-\Omega\right)\tilde{r}_{0}^{I}\left(\mu-\Omega\right)\right]^{n}t_{0}^{II}\left(\mu-\Omega\right),$$

$$t\left(t_{-1}^{II},\mu\right)=\sum_{n=0}^{\infty}t_{0}^{I}\left(\mu\right)\left[r_{0}^{II}\left(\mu\right)\tilde{r}_{0}^{I}\left(\mu\right)\right]^{n}t_{-1}^{II}\left(\mu\right),$$

$$t\left(\tilde{r}_{-1}^{I},\mu\right)=\sum_{m=0}^{\infty}\sum_{n=0}^{\infty}t_{0}^{I}\left(\mu\right)r_{0}^{II}\left(\mu\right)\left[\tilde{r}_{0}^{I}\left(\mu\right)r_{0}^{II}\left(\mu\right)\right]^{n}\tilde{r}_{-1}^{I}\left(\mu\right)\left[r_{0}^{II}\left(\mu-\Omega\right)\tilde{r}_{0}^{I}\left(\mu-\Omega\right)\right]^{m}t_{0}^{II}\left(\mu-\Omega\right)$$

$$t\left(r_{-1}^{II},\mu\right)=\sum_{m=0}^{\infty}\sum_{n=0}^{\infty}t_{0}^{I}\left(\mu\right)\left[r_{0}^{II}\left(\mu\right)\tilde{r}_{0}^{I}\left(\mu\right)\right]^{n}r_{-1}^{II}\left(\mu\right)\tilde{r}_{0}^{I}\left(\mu-\Omega\right)\left[r_{0}^{II}\left(\mu-\Omega\right)\tilde{r}_{0}^{I}\left(\mu-\Omega\right)\right]^{m}t_{0}^{II}\left(\mu-\Omega\right)$$

Fig. 2.6 to 2.9 give the physical picture of the four processes above.

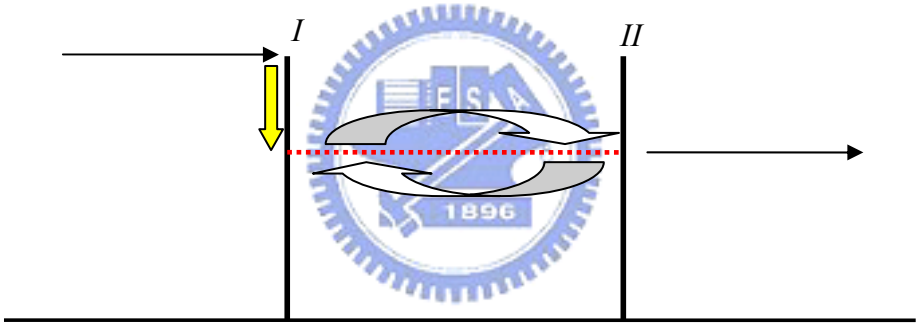

Fig. 2.6. Schematic sketch of $t\left(t_{-1}^{I},\mu\right)$. Electrons emit a photon at interface *I* by transmission emission, and make transition through the system after the multiple scattering process between interface *I* and *II*.

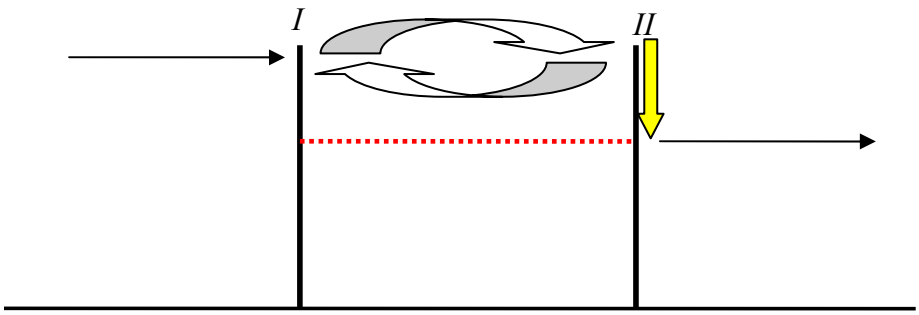

Fig. 2.7. Schematic sketch of $t\left(t_{-1}^{II},\mu\right)$. Electrons tunnel through interface *I* and have multiple scattering process between interface *I* and *II*. Then they make transition through interface *II* by transmission emission.

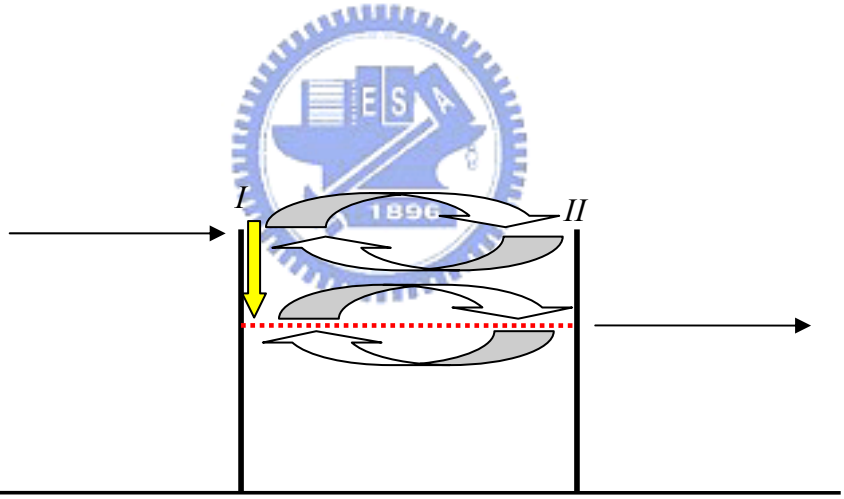

Fig. 2.8. Schematic sketch of $t\left(\tilde{r}_{-1}^{I},\mu\right)$. Electrons tunnel through interface I, having multiple scattering process. Then they emit a photon by reflection emission at interface *I*. Finally, they transmit through interface *II* after the multiple scattering process at the resonance state.

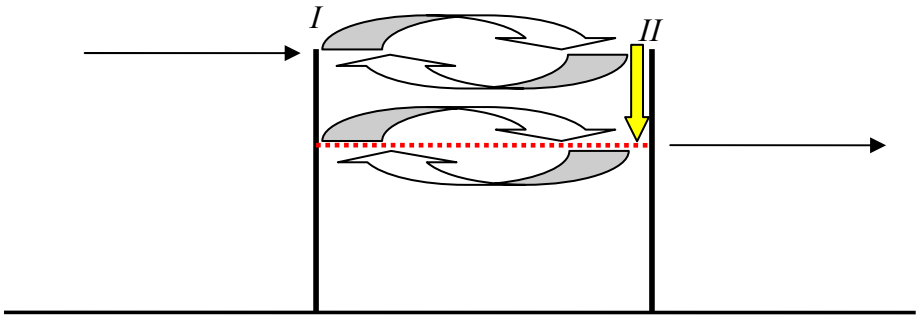

Fig. 2.9. Schematic sketch of $t\left(r_{-1}^{II},\mu\right)$. Electrons tunnel through interface *I*, having multiple scattering process. Then they emit a photon by reflection emission at interface *II*. Finally, they transmit through interface *II* after the multiple scattering process at the resonance state.

Analytical expressions for the 8 processes of Fig. 2.2 to 2.9 will be given in detail in Appendix B.

Under one-photon approximation, the total transmission,

$$T_1(\mu)=\left|t\left(t_1^I,\mu\right)+t\left(t_1^{II},\mu\right)+t\left(\tilde{r}_1^I,\mu\right)+t\left(r_1^{II},\mu\right)\right|^2\frac{k(1)}{k(0)} \tag{2.30}$$

$$T_{-1}(\mu)=\left|t\left(t_{-1}^I,\mu\right)+t\left(t_{-1}^{II},\mu\right)+t\left(\tilde{r}_{-1}^I,\mu\right)+t\left(r_{-1}^{II},\mu\right)\right|^2\frac{k(-1)}{k(0)} \tag{2.31}$$

We go through one-sideband approximation to one-photon approximation. Thus, we are able to compare numerical results of one-sideband approximation and one-photon approximation with direct numerical result. The complete comparisons are given in Ch. 3.

Although one-photon approximation approach gives good numerical calculations compared to exact numerical results, yet we do not understand the formation of sideband asymmetry. Hence, we examine each term contributing to total transmission current.

From Eq. (2.30), $T_1(\mu)=\left|t\left(t_1^I,\mu\right)+t\left(t_1^{II},\mu\right)+t\left(\tilde{r}_1^I,\mu\right)+t\left(r_1^{II},\mu\right)\right|^2\frac{k(1)}{k(0)}$, and

$$\begin{aligned}
&\left|t\left(t_1^I,\mu\right)+t\left(t_1^{II},\mu\right)+t\left(\tilde{r}_1^I,\mu\right)+t\left(r_1^{II},\mu\right)\right|^2\\
&=\left(\left|t\left(t_1^I,\mu\right)\right|^2+\left|t\left(t_1^{II},\mu\right)\right|^2+\left|t\left(\tilde{r}_1^I,\mu\right)\right|^2+\left|t\left(r_1^{II},\mu\right)\right|^2\right)\\
&+2\,\mathrm{Re}\left[t\left(t_1^I,\mu\right)t\left(t_1^{II},\mu\right)^*\right]+2\,\mathrm{Re}\left[t\left(t_1^I,\mu\right)t\left(\tilde{r}_1^I,\mu\right)^*\right]+2\,\mathrm{Re}\left[t\left(t_1^I,\mu\right)t\left(r_1^{II},\mu\right)\right]\\
&+2\,\mathrm{Re}\left[t\left(t_1^{II},\mu\right)t\left(\tilde{r}_1^I,\mu\right)^*\right]+2\,\mathrm{Re}\left[t\left(t_1^{II},\mu\right)t\left(r_1^{II},\mu\right)^*\right]+2\,\mathrm{Re}\left[t\left(\tilde{r}_1^I,\mu\right)t\left(r_1^{II},\mu\right)^*\right]
\end{aligned}$$

From Eq. (2.31), $T_{-1}(\mu)=\left|t\left(t_{-1}^I,\mu\right)+t\left(t_{-1}^{II},\mu\right)+t\left(\tilde{r}_{-1}^I,\mu\right)+t\left(r_{-1}^{II},\mu\right)\right|^2\frac{k(-1)}{k(0)}$, and

$$\begin{aligned}
&\left|t\left(t_{-1}^I,\mu\right)+t\left(t_{-1}^{II},\mu\right)+t\left(\tilde{r}_{-1}^I,\mu\right)+t\left(r_{-1}^{II},\mu\right)\right|^2\\
&=\left(\left|t\left(t_{-1}^I,\mu\right)\right|^2+\left|t\left(t_{-1}^{II},\mu\right)\right|^2+\left|t\left(\tilde{r}_{-1}^I,\mu\right)\right|^2+\left|t\left(r_{-1}^{II},\mu\right)\right|^2\right)\\
&+2\,\mathrm{Re}\left[t\left(t_{-1}^I,\mu\right)t\left(t_{-1}^{II},\mu\right)^*\right]+2\,\mathrm{Re}\left[t\left(t_{-1}^I,\mu\right)t\left(\tilde{r}_{-1}^I,\mu\right)^*\right]+2\,\mathrm{Re}\left[t\left(t_{-1}^I,\mu\right)t\left(r_{-1}^{II},\mu\right)\right]\\
&+2\,\mathrm{Re}\left[t\left(t_{-1}^{II},\mu\right)t\left(\tilde{r}_{-1}^I,\mu\right)^*\right]+2\,\mathrm{Re}\left[t\left(t_{-1}^{II},\mu\right)t\left(r_{-1}^{II},\mu\right)^*\right]+2\,\mathrm{Re}\left[t\left(\tilde{r}_{-1}^I,\mu\right)t\left(r_{-1}^{II},\mu\right)^*\right]
\end{aligned}$$

We can see from Fig. 3.12 that $\left|t\left(t_1^I,\mu\right)\right|^2\frac{k(1)}{k(0)}$ contributes the most in total current transmission of $\varepsilon_r-\Omega_1$ channel (ε_r denotes the resonance energy), whereas $\left|t\left(t_{-1}^I,\mu\right)\right|^2\frac{k(-1)}{k(0)}$ contributes the most of $\varepsilon_r+\Omega_1$ channel.

For interference terms of $T_1(\mu)$ and $T_{-1}(\mu)$, we see from Fig. 3.14 and 3.15 that $2\,\mathrm{Re}\left[t\left(t_1^I,\mu\right)t\left(\tilde{r}_1^I,\mu\right)^*\right]\frac{k(1)}{k(0)}$ and $2\,\mathrm{Re}\left[t\left(t_1^I,\mu\right)t\left(r_1^{II},\mu\right)\right]\frac{k(1)}{k(0)}$ have the most contribution to $\varepsilon_r-\Omega_1$ channel, while $2\,\mathrm{Re}\left[t\left(t_{-1}^I,\mu\right)t\left(\tilde{r}_{-1}^I,\mu\right)^*\right]\frac{k(-1)}{k(0)}$ and $2\,\mathrm{Re}\left[t\left(t_{-1}^I,\mu\right)t\left(r_{-1}^{II},\mu\right)\right]\frac{k(-1)}{k(0)}$ have the most (negative) effect on $\varepsilon_r+\Omega_1$ channel. Further discussions of these interference terms are given in Appendix C.

Chapter 3
A Study on the Sideband Asymmetry in Time-modulated Transport

We found the asymmetric feature of photon sidebands under double-barrier configuration by mono-frequency modulation. This strongly aroused our interests, and hence, we did one-photon approximation, as in Sec. 2.3, to get the physical picture and more understanding of the formation of sideband asymmetry. Contribution of each term in one-photon approximation is given in Sec. 3.4 in this chapter.

In addition, sideband asymmetry features under different static-barrier configurations are different. Results of sideband features under different configuration are also given in this chapter including double-barrier, double-well, and barrier-well configurations. Electrons tend to absorb or emit photons under specific conditions. Within in this chapter, oscillation frequencies and amplitudes of both barriers are set to be the same.

Transmission under one-sideband approximation is given in Sec. 3.4, in proving of the validity of one-photon approximation, because one-photon approximation is derived from one-sideband approximation.

Resonance states are found to shift when barriers are time-dependent, and the detail discussions will be presented in Ch. 5. We also found some interesting result under strong oscillation conditions, and when resonance level is close to subband bottom. Numerical results of these results are given in Ch. 7.

3.1 Double-barrier

In this section, we find the feature of sideband asymmetry under double-barrier configuration. We can see asymmetric sideband features both in Fig. 3.1 and 3.2, and Fig. 3.2 exhibits more sidebands channels due to stronger oscillation amplitude. In Fig. 3.3, we introduce a phase difference-π into the system, and sideband features are much more balanced.

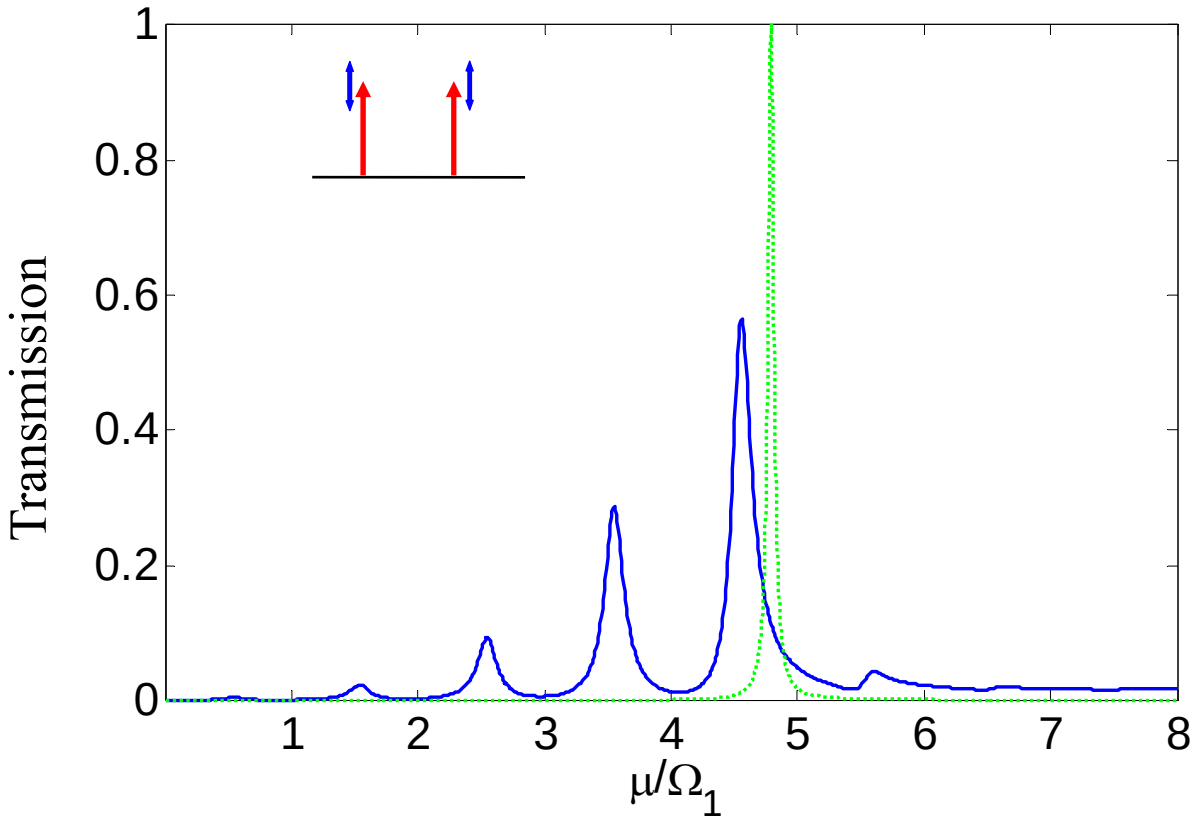

Fig. 3.1. Transmission as a function of μ for a=15, V_{s1}=V_{s2}=3, V_{d1}=V_{d2}=2.5, and Ω_2=Ω_1=0.0084. Dotted line is the resonance state of double-barrier of V_{s1}=V_{s2}=3. Electrons are more probable to make transition through the resonance state by absorbing photons. Resonance state shifts towards lower energy level. Discussion of level-shifting will be given in Ch. 5.

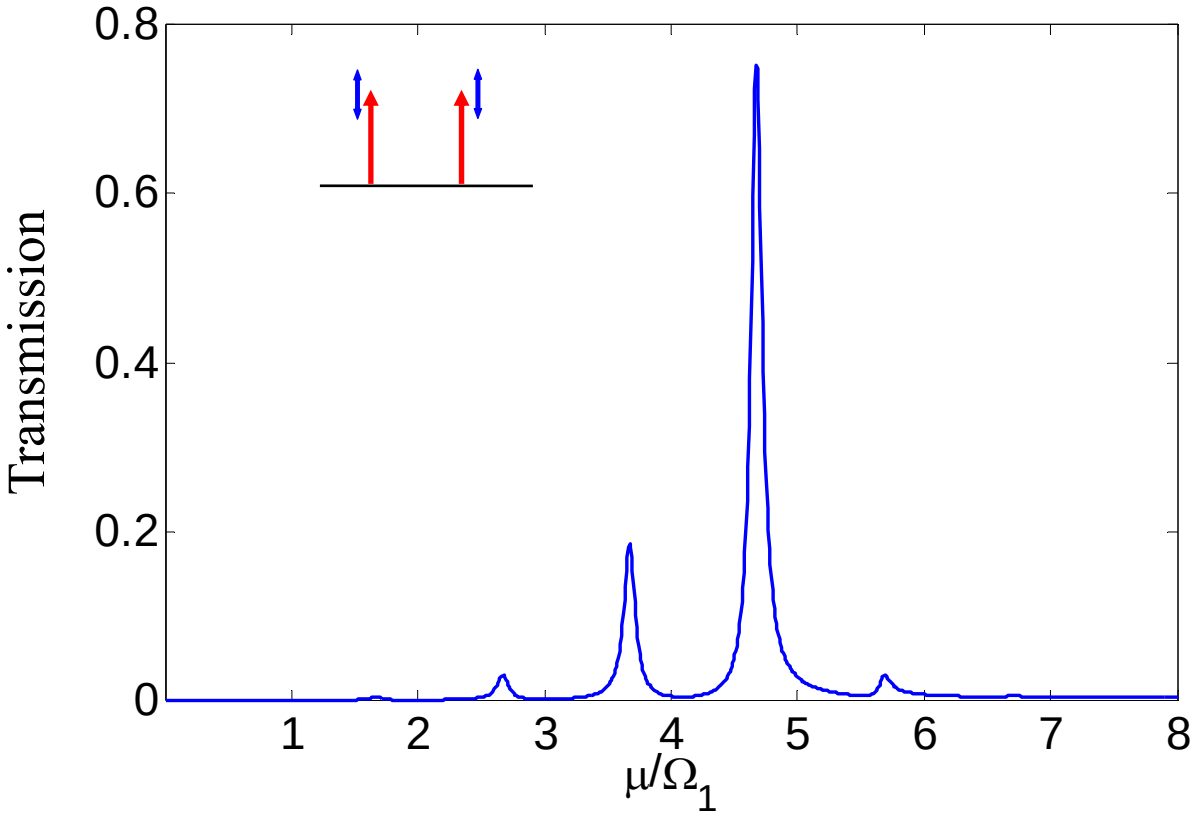

Fig. 3.2. Transmission as a function for μ for a=15, V_{s1}=V_{s2}=3, V_{d1}=V_{d2}=2, and Ω_2=Ω_1=0.0084. Sideband features are not as strong when oscillation amplitudes are weakened comparing to Fig. 3.1.

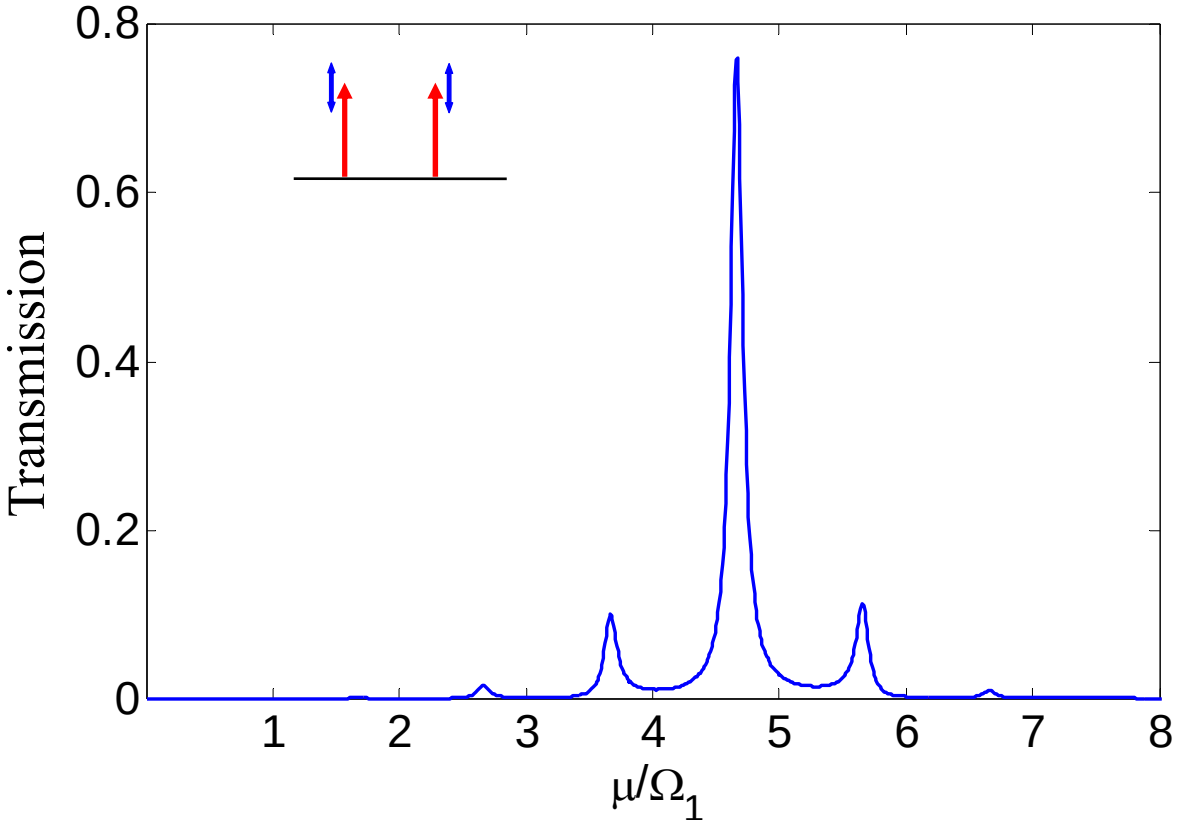

Fig. 3.3. Transmission as a function of μ for a=15, V_{s1}=V_{s2}=3, V_{d1}=V_{d2}=2, Ω_2=Ω_1=0.0084, and ϕ=π. As shown in the figure, asymmetry features will be more balanced when we introduce a phase difference between the barriers.

3.2 Double-well

After doing double-barrier configuration, we are curious whether the asymmetry features still exists in double-well configuration. Consequently, we find yet another interesting feature. Asymmetric sideband features still exist, but electrons tend to emit photons rather than absorb photons.

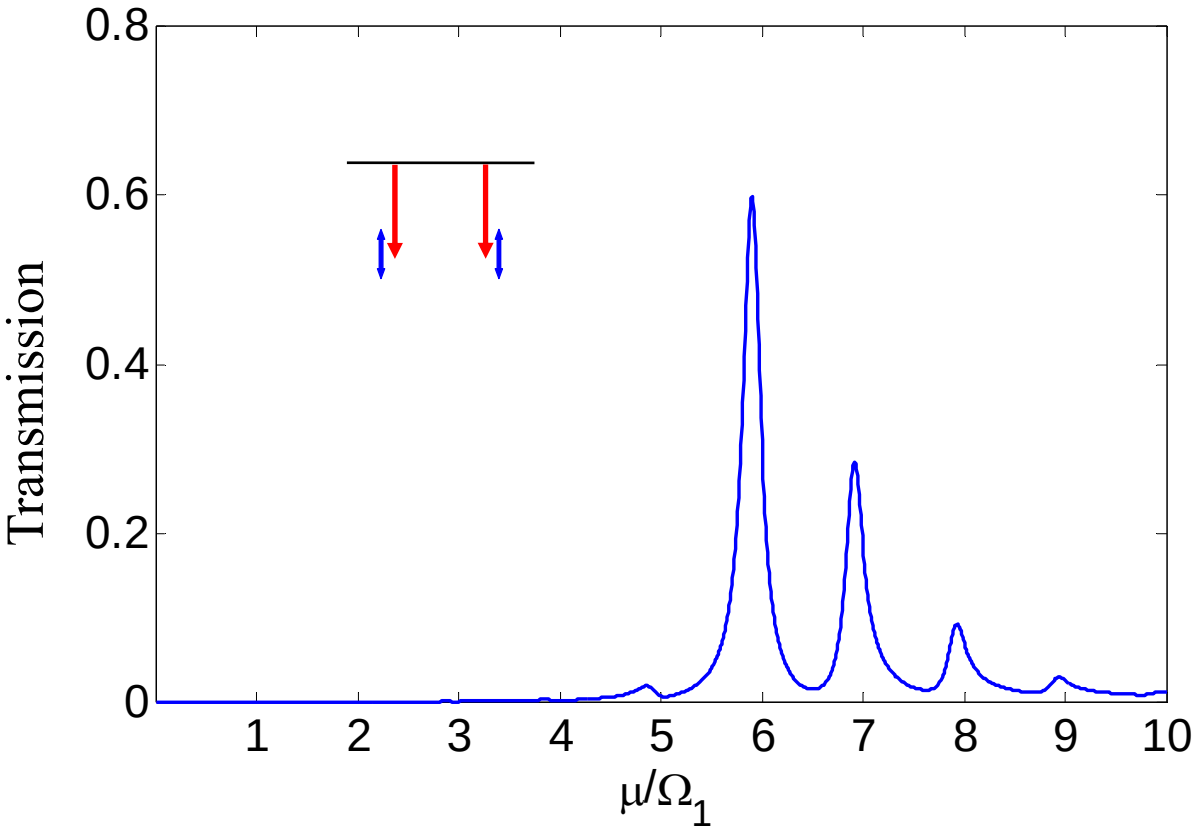

Fig. 3.4. Transmission as a function of μ for a=15, V_{s1}=V_{s2}=-3, V_{d1}=V_{d2}=2, and Ω_2=Ω_1=0.0084. Electrons are more probable to make transition through resonance state by emitting photons.

As shown in Fig. 3.2 and 3.4, sideband features are much different under different configurations. We have to note that we study the small oscillation amplitude regime in this chapter ($V_d < V_s$). Results of strong oscillation are given in Ch. 7.

3.3 Barrier-well

We do barrier-well configuration after doing double-barrier and double-well configurations. As shown in Fig. 3.5, $T_{\rightarrow}$ and $T_{\leftarrow}$ show different sideband characteristics in this case. From Fig. 3.2, we can see that when an electron scatters with time-dependent barriers, it is more likely to absorb photons and make transition through the resonance state; on the other hand, from Fig. 3.4, we see that if an electron scatters with time-dependent wells, it tends to make transition by emitting photons. In Fig. 3.5, due to the barrier-well configuration, we find that electrons incident from the left tend to make transition by absorbing photons, while electrons incident from the right are more likely to make transition by emitting photons.

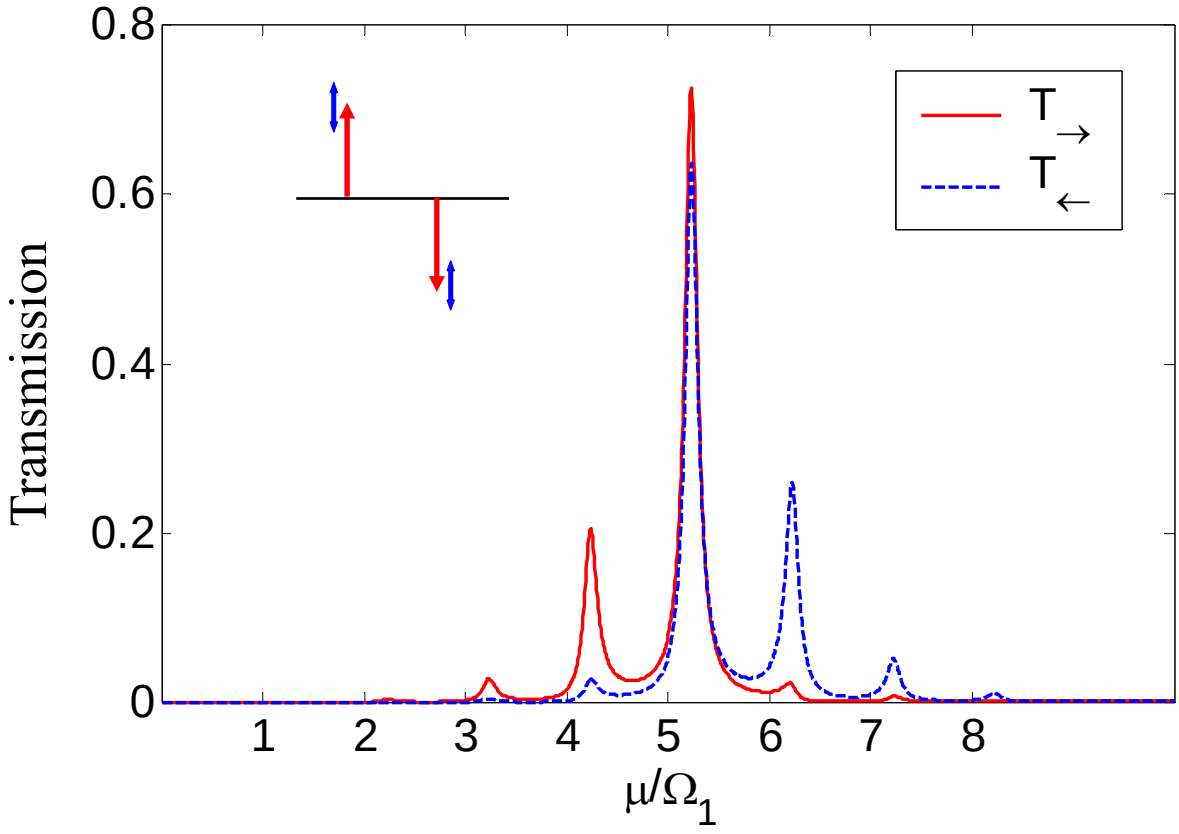

Fig. 3.5. Transmission as a function of μ for a=15, V_{s1}=3, V_{s2}=-3, V_{d1}=V_{d2}=2, and Ω_2=Ω_1=0.0084.

3.4 One-sideband Approximation

In Fig. 3.6 and 3.7, we see that numerical calculation under one-sideband approximation is better when oscillation amplitudes are smaller. Approximations in both Fig. 3.5 and 3.7 are good. As mentioned in Ch. 2, we advance our one-photon approximation under conditions where one-sideband approximation gives good numerical results. Sidepband channels specified by arrows in Fig. 3.6 and 3.7 are the ones we will study in Sec. 3.5.

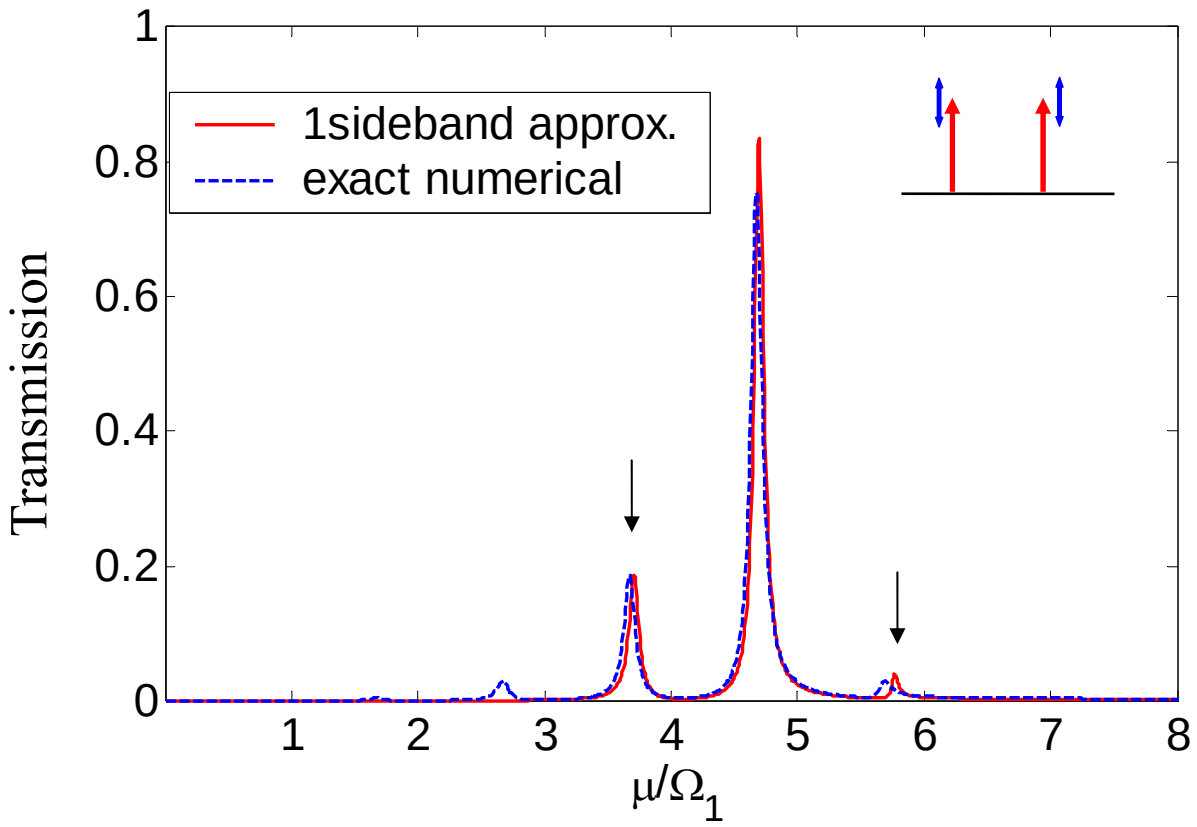

Fig. 3.6. Transmission as a function of μ for a=15, V_{s1}=V_{s2}=3, V_{d1}=V_{d2}=2, and Ω_2=Ω_1=0.0084. Solid line is the calculation under one-sideband approximation, and dashed-line is the exact numerical calculation.

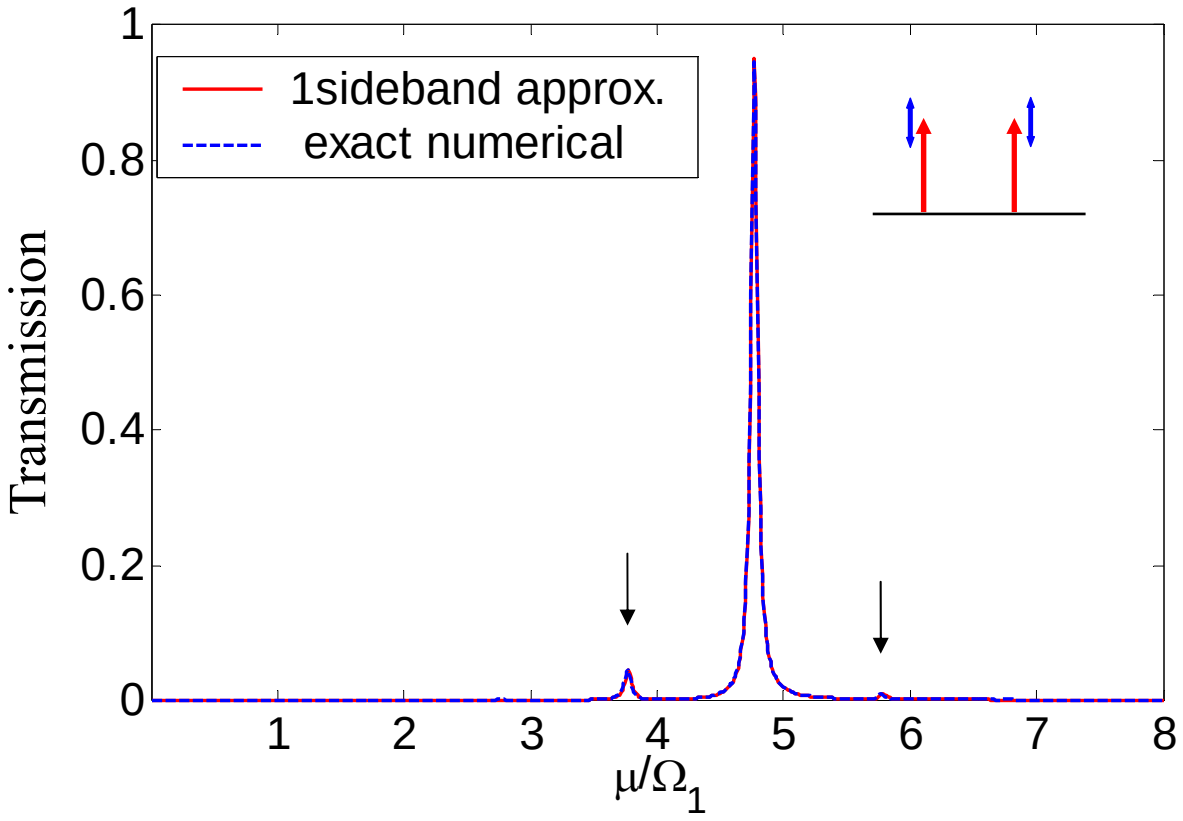

Fig. 3.7. Transmission as a function of μ for a=15, V_{s1}=V_{s2}=3, V_{d1}=V_{d2}=1, and Ω_2=Ω_1=0.0084. Solid line represents the numerical results under one-sideband approximation.

3.5 One-photon Approximation

Formulation of one-photon approximation is given in Sec. 2.3. In this subsection, we demonstrate the result of one-photon approximation of double-barrier configuration. The causes of sideband asymmetry are clearer by one-photon approximation. Fig. 3.8 and 3.9 gives one-photon approximation without phase difference, while Fig. 3.10 and 3.11 gives one-photon approximation with phase difference π. Fig. 3.12 to 3.15 are the analysis of Fig. 3.9.

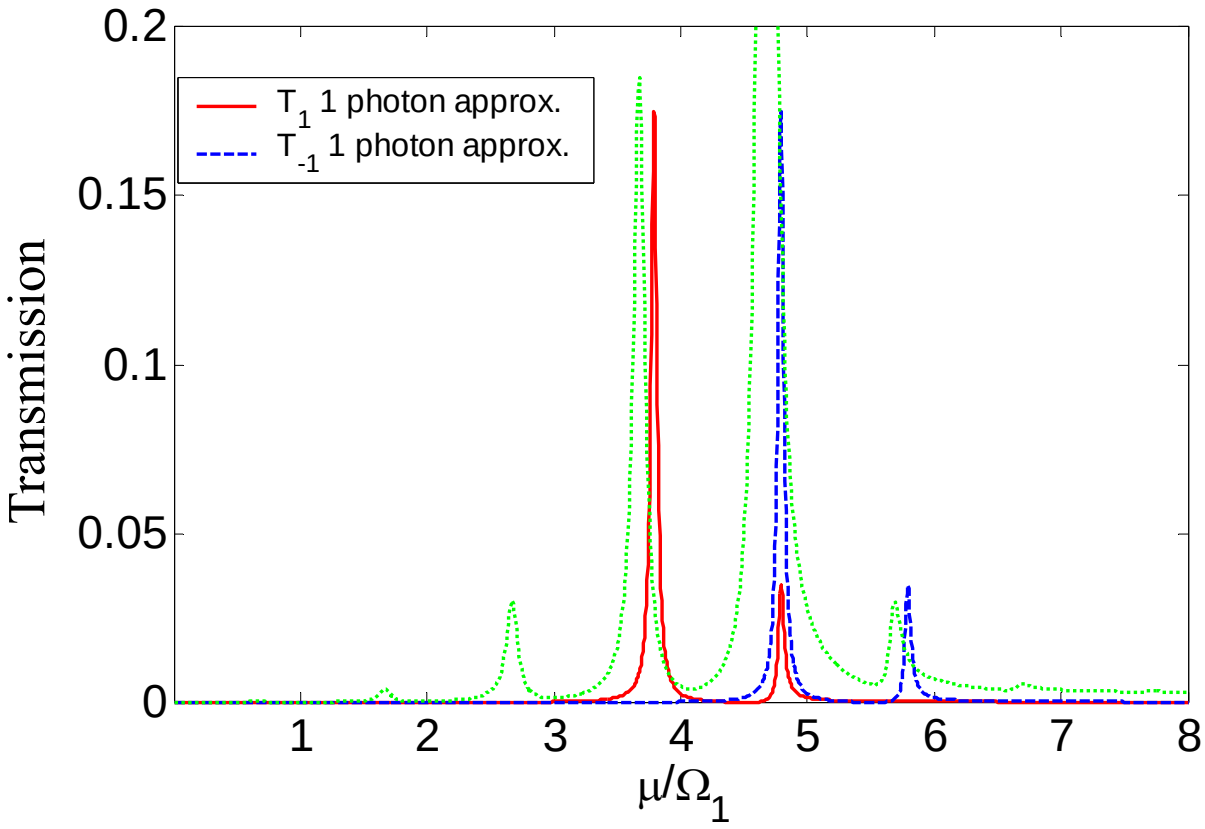

Fig. 3.8. Transmission as a function of μ for a=15, V_{s1}=V_{s2}=3, V_{d1}=V_{d2}=2, and Ω_2=Ω_1=0.0084. Dotted line indicates the exact numerical calculation.

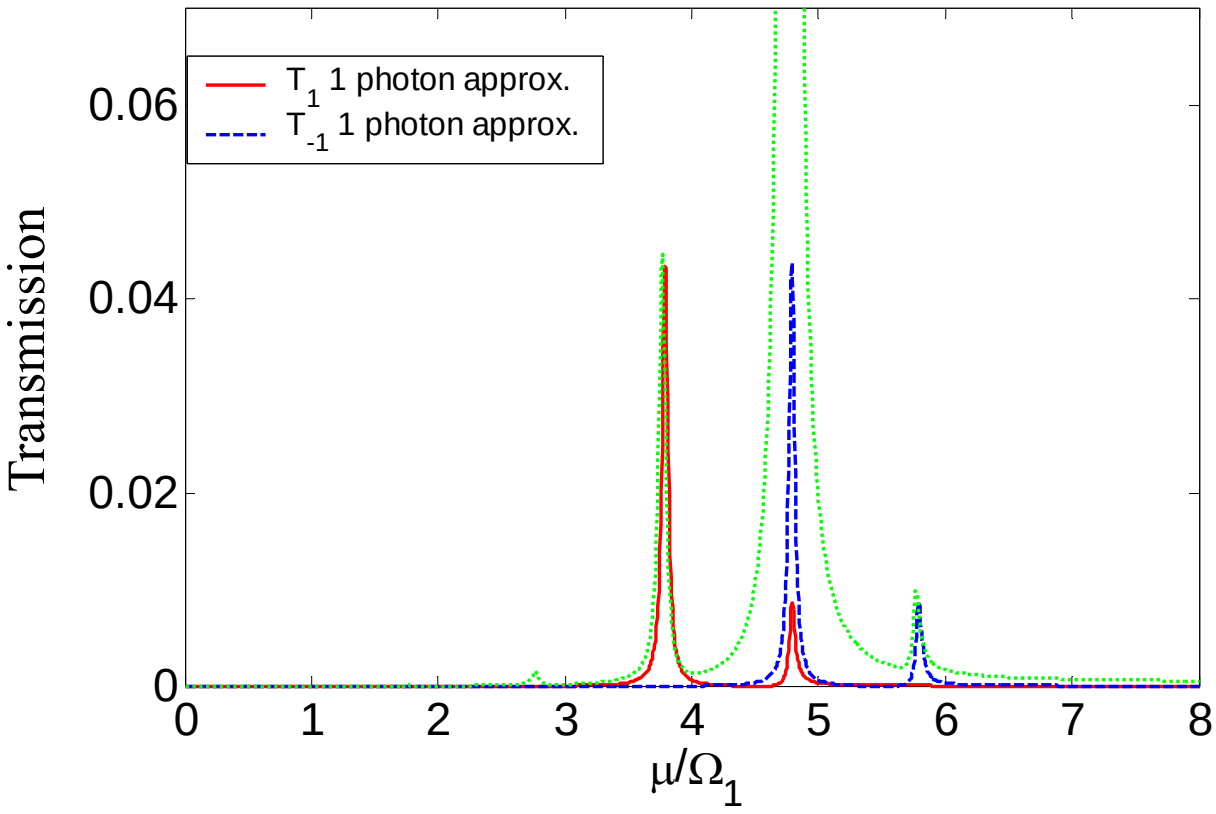

Fig. 3.9. Transmission as a function of μ for a=15, V_{s1}=V_{s2}=3, V_{d1}=V_{d2}=1, and Ω_2=Ω_1=0.0084. Dotted line indicates the exact numerical calculation.

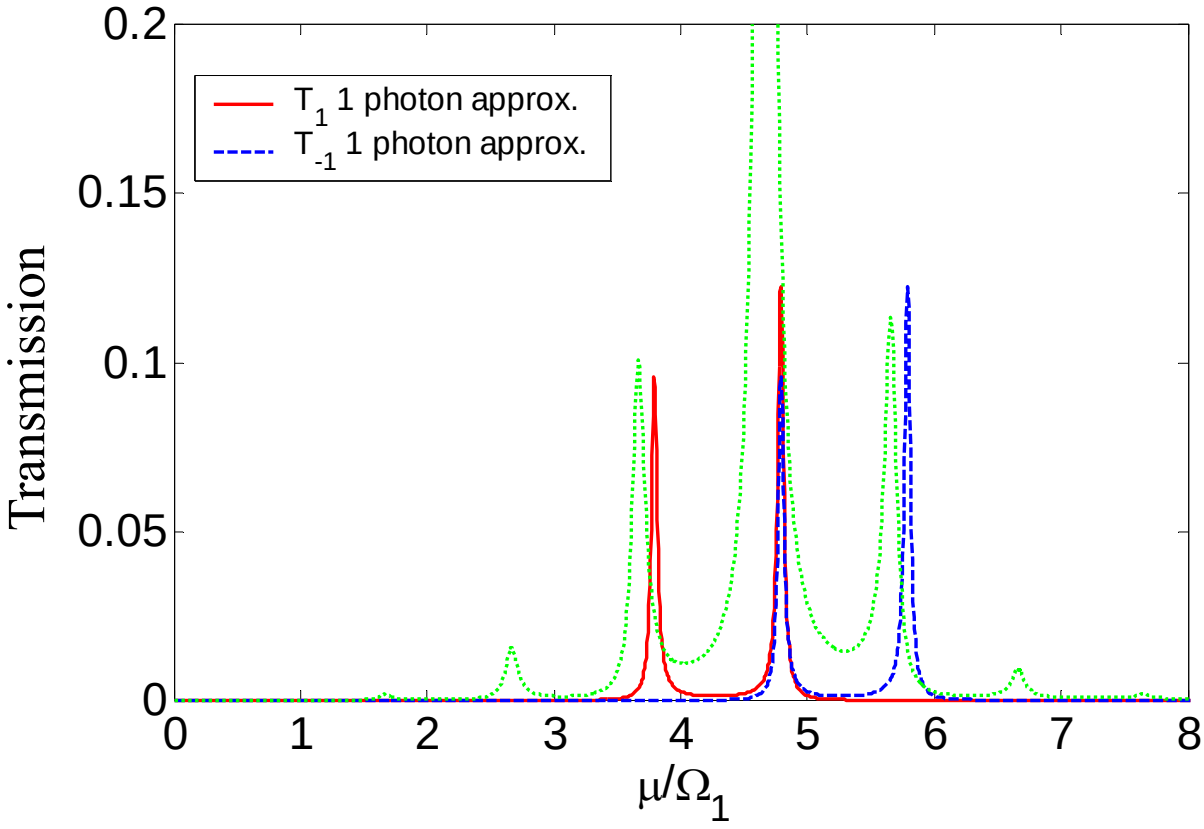

Fig. 3.10. Transmission as a function of μ for a=15, V_{s1}=V_{s2}=3, V_{d1}=V_{d2}=2, Ω_2=Ω_1=0.0084, and ϕ=π. Dotted line indicates the exact numerical calculation.

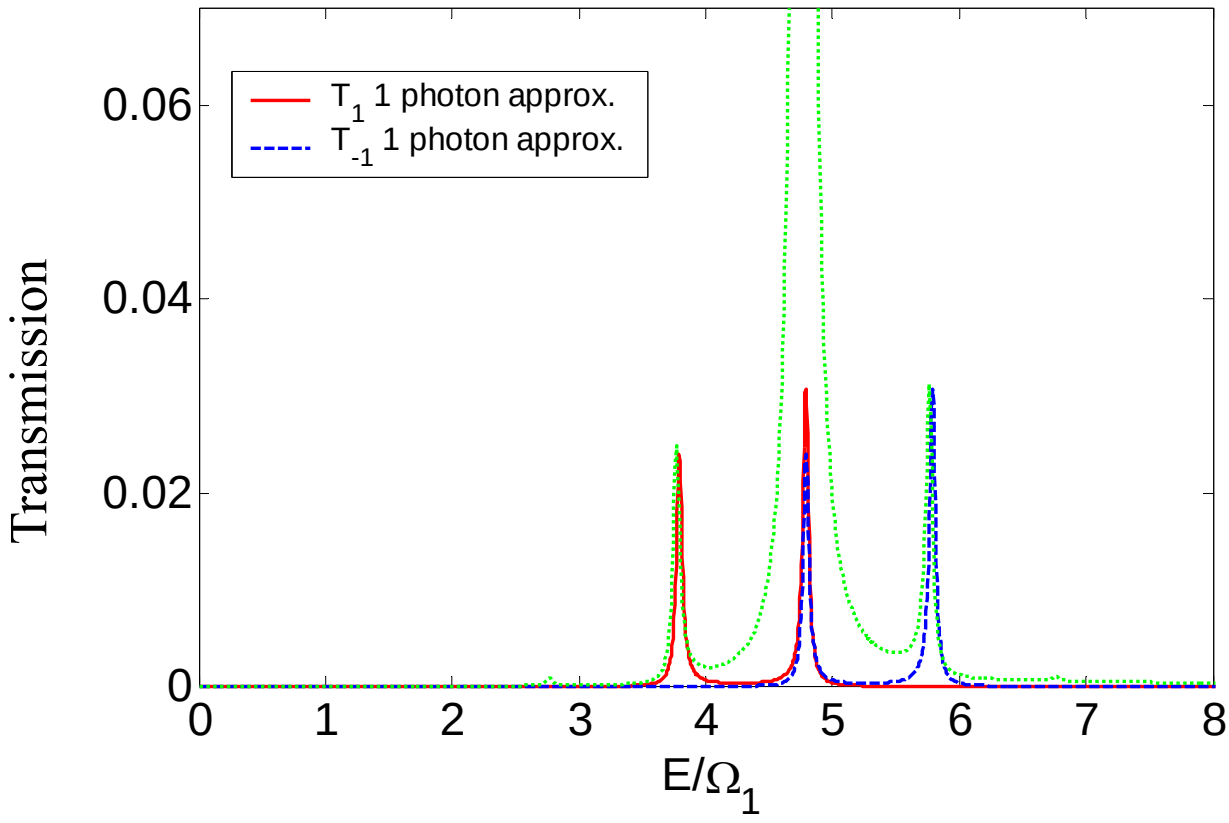

Fig. 3.11. Transmission as a function of μ for a=15, V_{s1}=V_{s2}=3, V_{d1}=V_{d2}=1, Ω_2=Ω_1=0.0084, and ϕ=π. Dotted line indicates the exact numerical calculation.

From Fig. 3.8 and 3.10, we see that one-photon approximation gives good numerical calculation in explaining the asymmetry of sidebands even though the oscillation amplitude is strong, such as V_d=2. Thus, the validity of one-photon approximation is not just limited in small oscillation regime.

The following figures are the contribution of each term of T_1 and T_{-1} in one-photon approximation. We can see from Fig. 3.14 and 3.15 that the interference terms of Fig. 3.14 and 3.15 contribute different parities to transmission at the specific sideband channels where we're interested in.

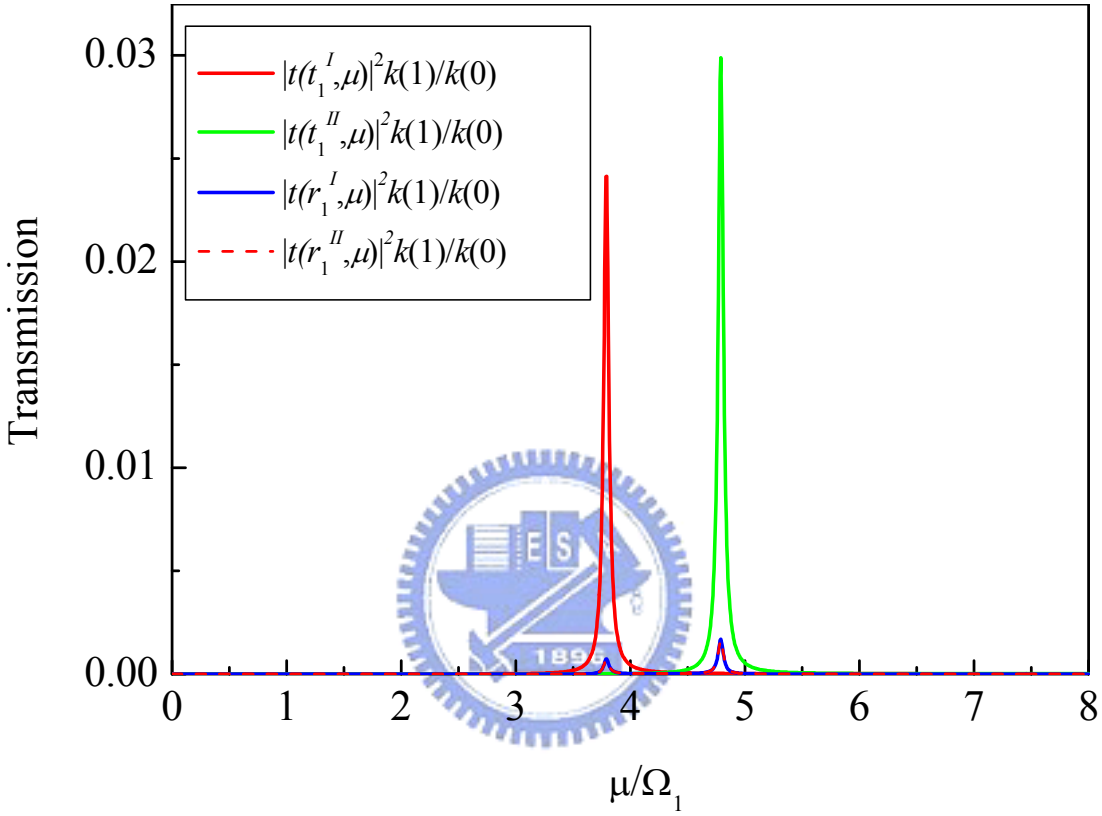

Fig. 3.12. Transmission as a function of μ for a=15, V_{s1}=V_{s2}=3, V_{d1}=V_{d2}=1, and Ω_2=Ω_1=0.0084. Curves in this figure are the transmission contributions of $t\left(t_1^I,\mu\right)$, $t\left(t_1^{II},\mu\right)$, $t\left(\tilde{r}_1^I,\mu\right)$, and $t\left(r_1^{II},\mu\right)$.

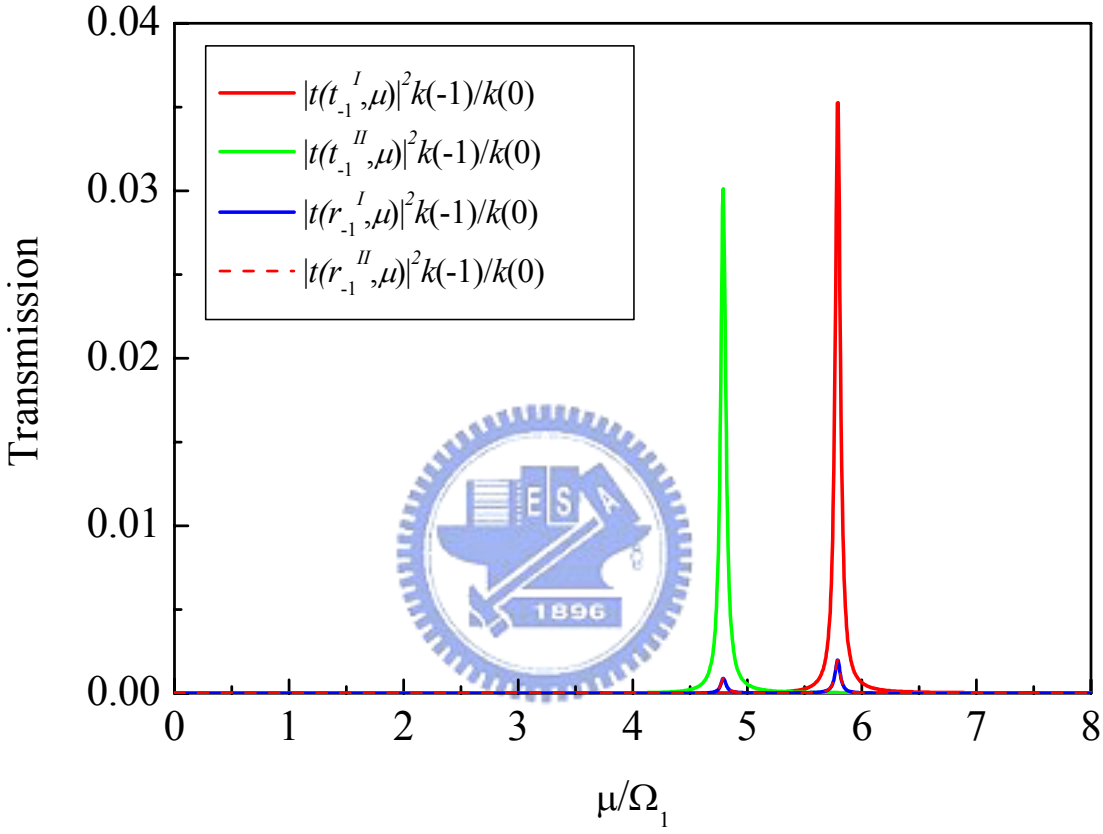

Fig. 3.13. Transmission as a function of μ for a=15, V_{s1}=V_{s2}=3, V_{d1}=V_{d2}=1, and Ω_2=Ω_1=0.0084. Curves in this figure are the transmission contributions of $t\left(t_{-1}^{I},\mu\right)$, $t\left(t_{-1}^{II},\mu\right)$, $t\left(\tilde{r}_{-1}^{I},\mu\right)$, and $t\left(r_{-1}^{II},\mu\right)$.

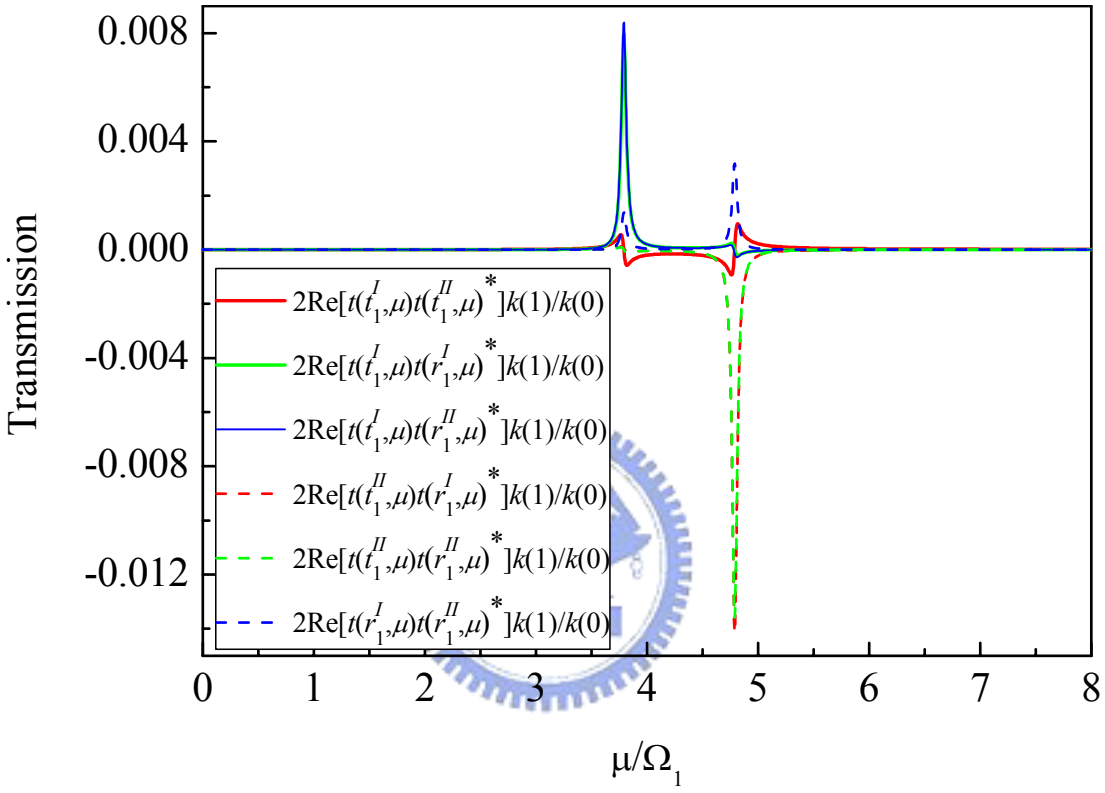

Fig. 3.14. Transmission as a function of μ for a=15, V_{s1}=V_{s2}=3, V_{d1}=V_{d2}=1, and Ω_2=Ω_1=0.0084. The six curves in this figure are the interference terms of the four processes defined in Sec. 2.3. We have six interference terms from $t\left(t_1^I,\mu\right)$, $t\left(t_1^{II},\mu\right)$, $t\left(\tilde{r}_1^I,\mu\right)$, and $t\left(r_1^{II},\mu\right)$.

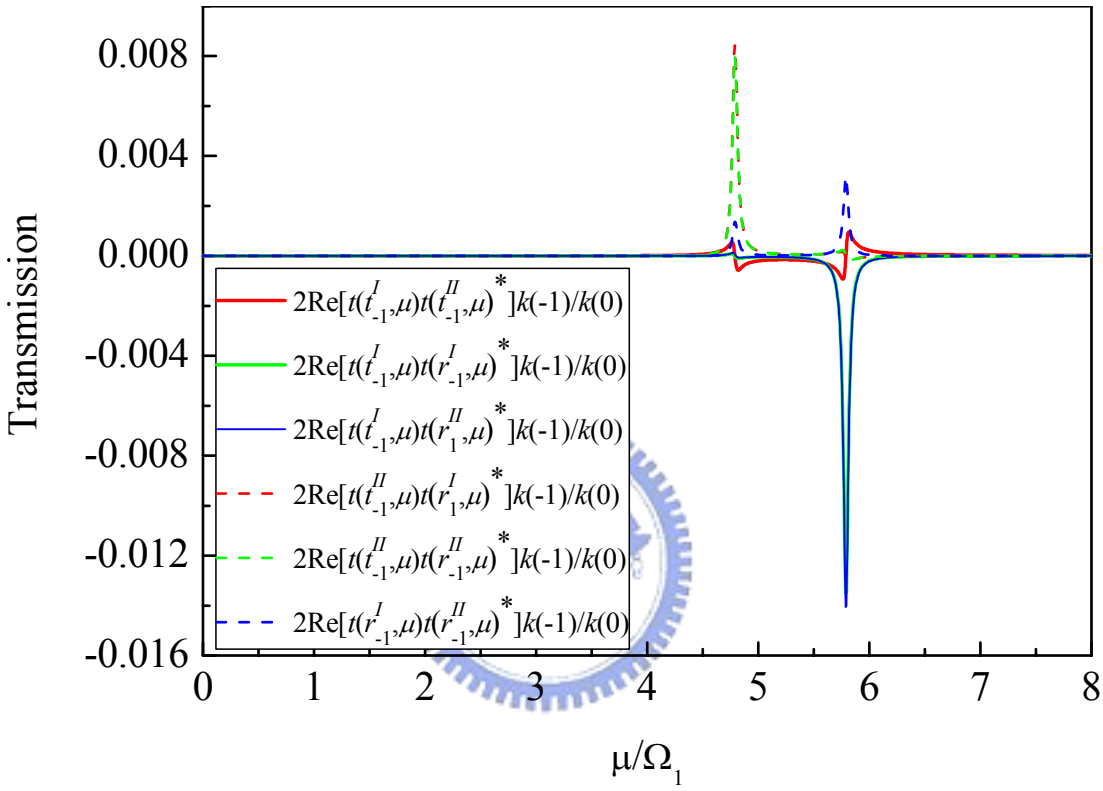

Fig. 3.15. Transmission as a function of μ for a=15, V_{s1}=V_{s2}=3, V_{d1}=V_{d2}=1, and Ω_2=Ω_1=0.0084. The six curves in this figure are the interference terms of the four processes defined in Sec. 2.3. Same as Fig. 3.14, we have six interference terms from $t\left(t_{-1}^{I},\mu\right)$, $t\left(t_{-1}^{II},\mu\right)$, $t\left(\tilde{r}_{-1}^{I},\mu\right)$, and $t\left(r_{-1}^{II},\mu\right)$.

We are able to conclude from Fig. 3.12 to 3.15 that the cause of sideband asymmetry comes mainly from interference terms.

Chapter 4
A Study on the Dual-frequency Modulation in Time-modulated Transport

In this chapter, we mainly study sideband characteristics under dual-frequency modulation on double-barrier configurations because sideband features are notable in existence of resonance state. We start with single time-dependent oscillating barrier in Sec. 4.1, and then the dual-frequency double time-dependent oscillating barriers in Sec. 4.2. Formulations for numerical calculation are derived in Sec. 2.1. Electrons incident from opposite sides of the system exhibit different sideband characteristics. We also compare sideband features of different ratio of Ω_2/Ω_1. Same as that in Ch. 3, we study the regime where $V_d < V_s$. Strong oscillation modulations are given in Ch. 7.

Quantum charge pumping can be achieved by introducing a phase difference in to a pair of time-dependent oscillating potentials. We try an alternative way of dual-frequency modulation to achieved quantum charge pumping effect. Result of net pumped current will be given in Ch. 6.

4.1 One Oscillating Barrier on Top of a Static Double Barrier

In this section, we consider single oscillating barrier in each case, that is, either $V_{d1}\cos\Omega_1 t$ or $V_{d2}\cos\Omega_2 t$ is applied at one time. From Fig 4.1 and 4.2, we can see that

$T_{\rightarrow}$ and $T_{\leftarrow}$ exhibit different sideband characteristics in each case. In Fig. 4.1, $T_{\rightarrow}$ shows notable n-Ω_1 sideband features while $T_{\leftarrow}$ possesses more notable n-Ω_2 sideband features. We also see the shifting of resonance states and this will be further discussed in Ch. 5.

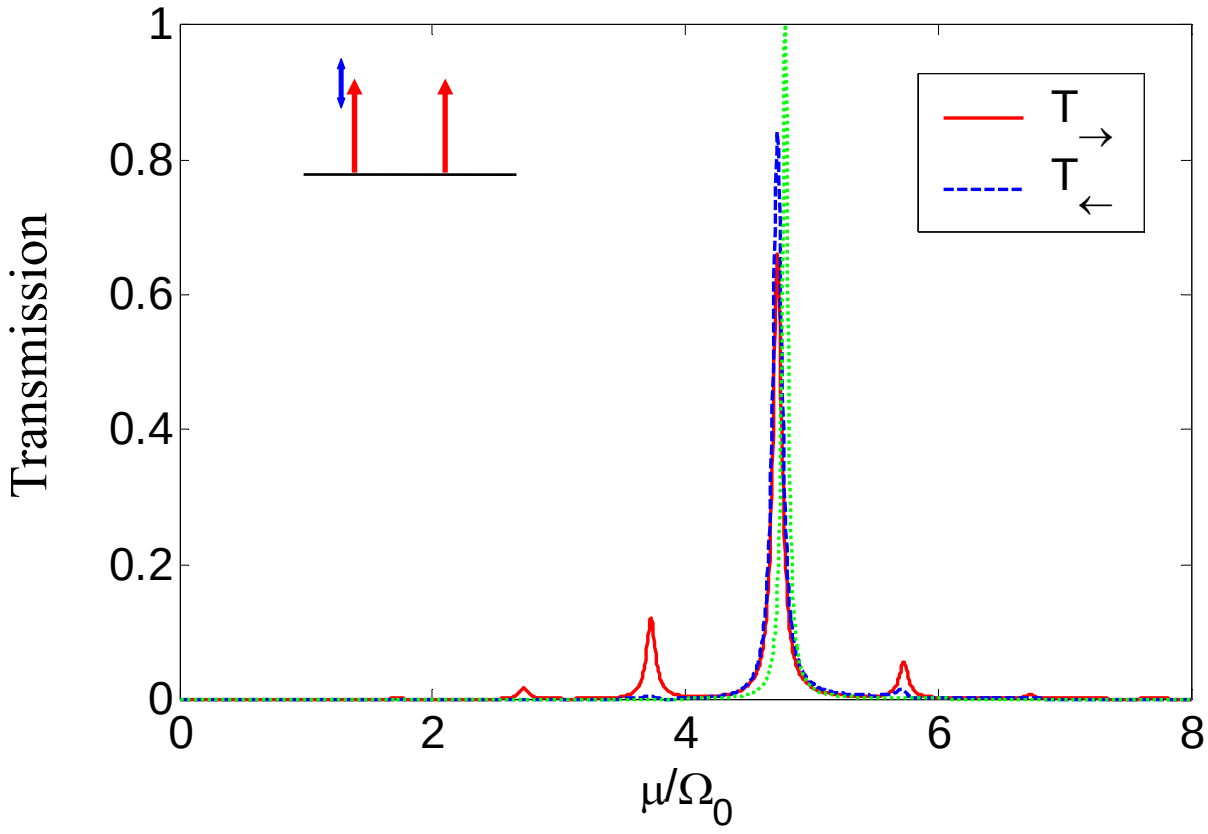

Fig. 4.1. Transmission as a function of μ for a=15, V_{s1}=V_{s2}=3, V_{d1}=2, V_{d2}=0, and Ω_1=Ω_0=0.0084. Electrons incident from the left exhibit stronger sideband features than electrons incident from the right. Dotted line depicts the resonance state without time-dependent potentials.

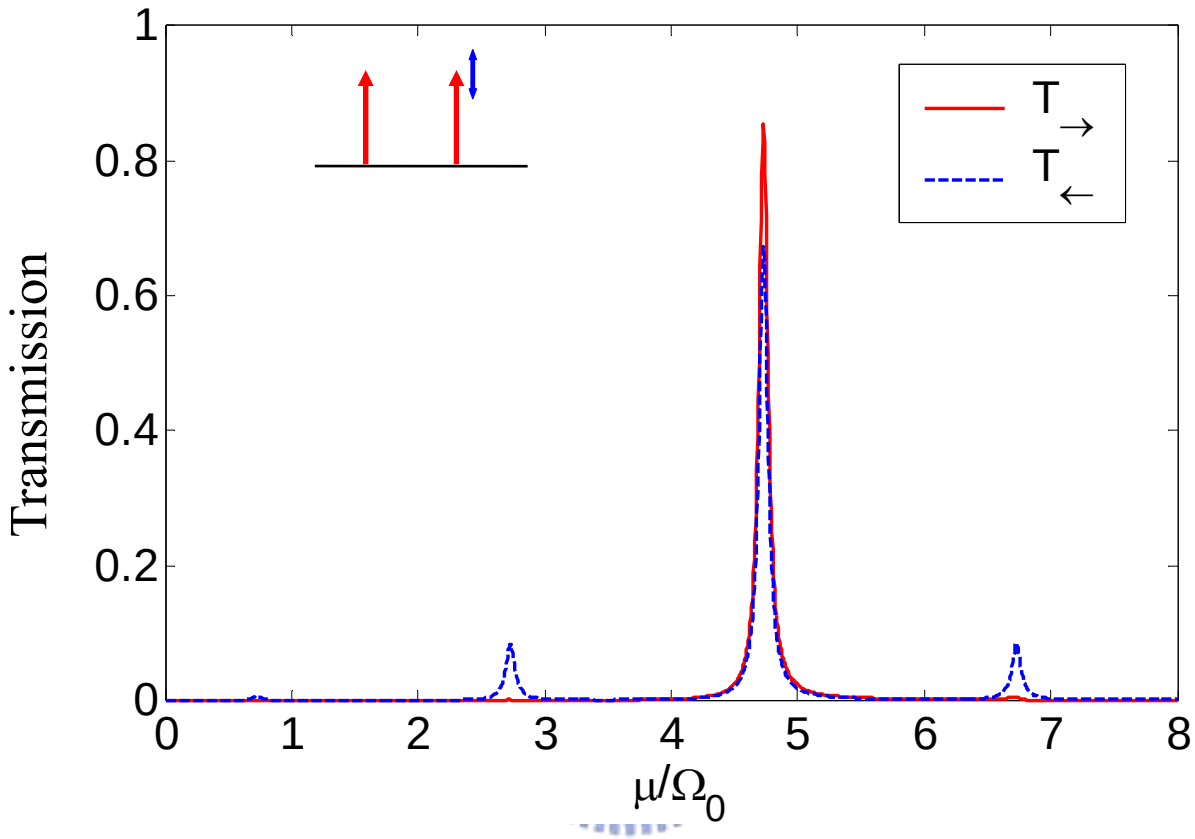

Fig. 4.2. Transmission as a function of μ for a=15, V_{s1}=V_{s2}=3, V_{d1}=0, V_{d2}=2, and Ω_2=2Ω_0=0.0168. Electrons incident from the right exhibit stronger sideband features than electrons incident from the left.

From Fig. 4.1 and 4.2, we can see that electrons exhibit weak sideband features if they scatter are screened by a static barrier before interacting with a time-dependent potential.

4.2 Two Oscillating Barriers on Top of a Static Double Barrier

In this subsection, we study the time-dependent transport phenomena when both $V_{d1}\cos\Omega_1 t$ and $V_{d2}\cos\Omega_2 t$ are applied to the system. Electrons incident from both sides of the system interact with the time-dependent potentials, but still, $T_{\rightarrow}$ and $T_{\leftarrow}$ exhibit much different sideband characteristics.

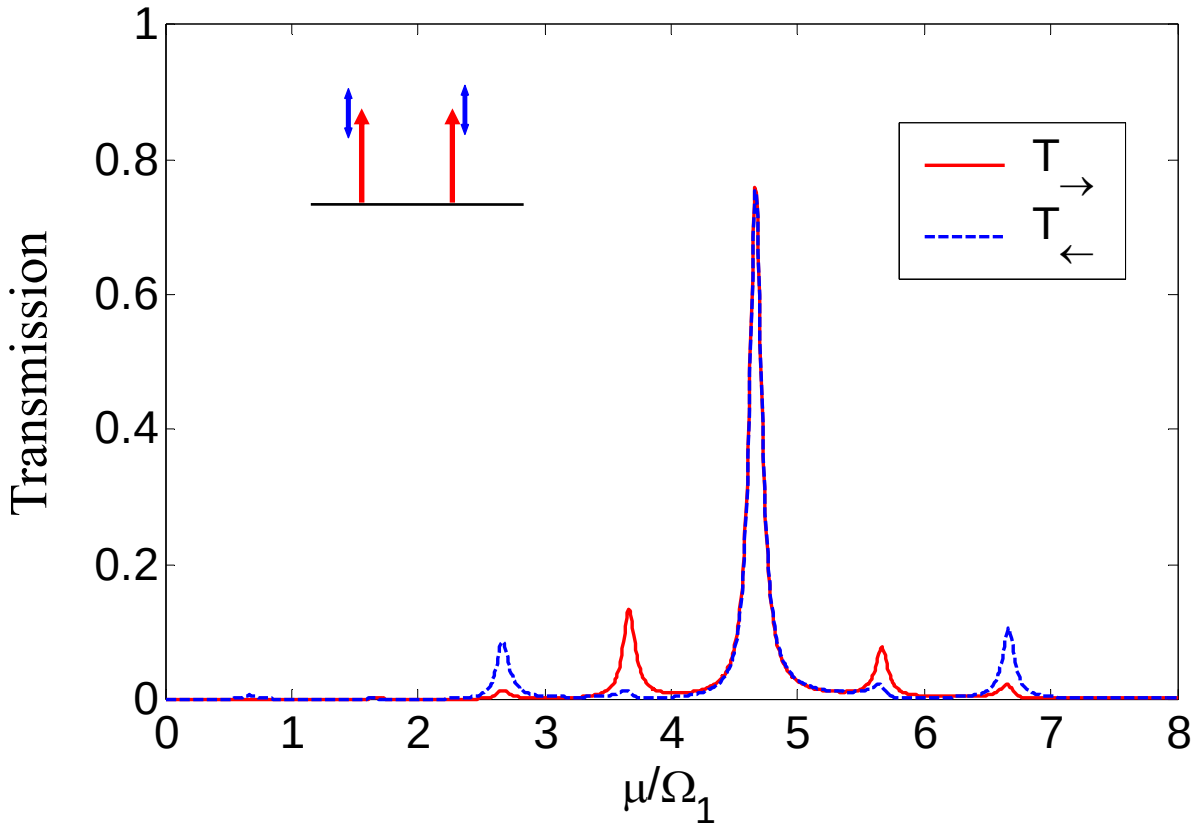

Fig. 4.3. Transmission as a function of μ for a=15, $V_{s1}=V_{s2}=3$, $V_{d1}=V_{d2}=2$, $\Omega_1=0.0084$, and $\Omega_2=2\Omega_1=0.0168$.

Electrons incident from the left of the system scatter with oscillating barrier of frequency Ω_1 first, thus they have more notable n-Ω_1 sideband features. Conversely, electrons incident from the right of the barrier exhibit stronger n-Ω_2 sideband features.

4.3 Cases of Different Dual Frequency Pairs

Both of the oscillating barriers are turned on under dual-frequency modulation. In this subsection, we set $\Omega_2=3\Omega_1$ in Fig. 4.4, and $\Omega_2=4\Omega_1$ in Fig. 4.5. Still, as in Sec. 4.2, electrons incident from the left possess more notable n-Ω_1 sideband features, whereas electrons incident from the right possess notable n-Ω_2 sideband features.

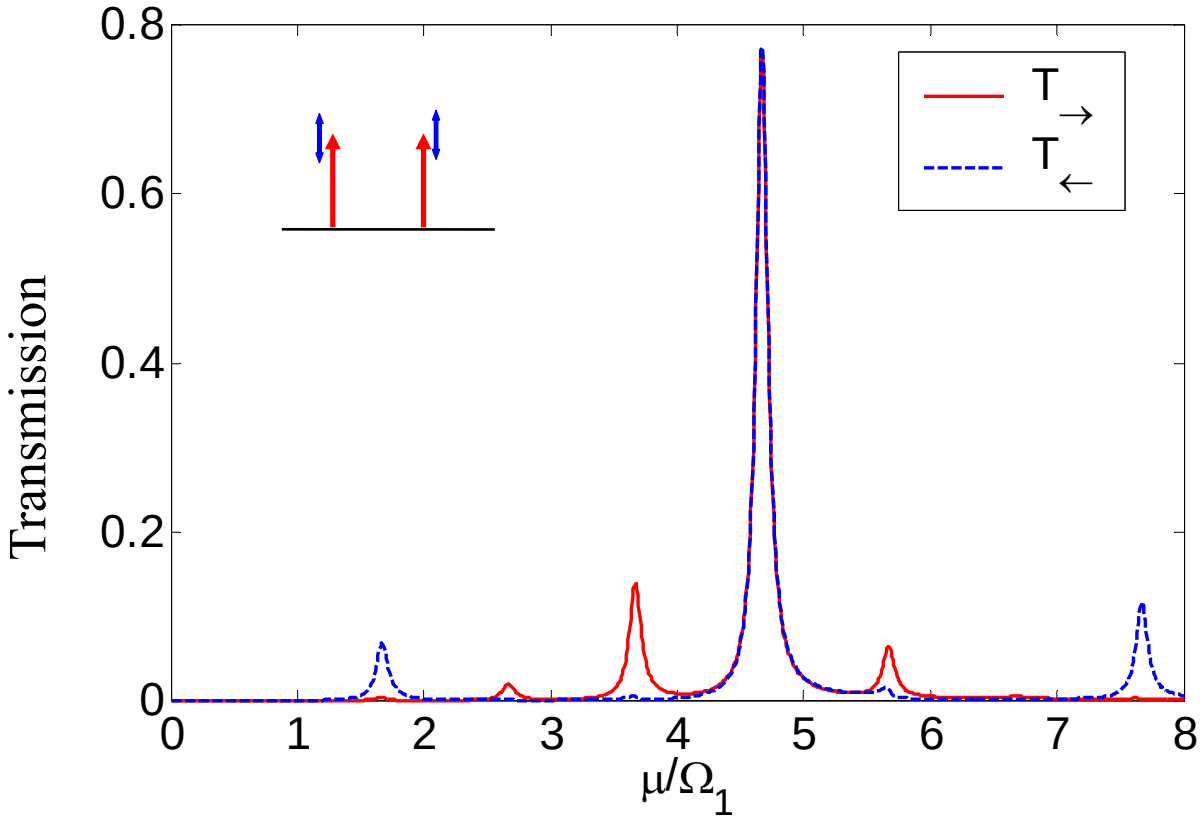

Fig. 4.4. Transmission as a function of μ for a=15, $V_{s1}=V_{s2}=3$, $V_{d1}=V_{d2}=2$, $\Omega_1=0.0084$, and $\Omega_2=3\Omega_1=0.0252$.

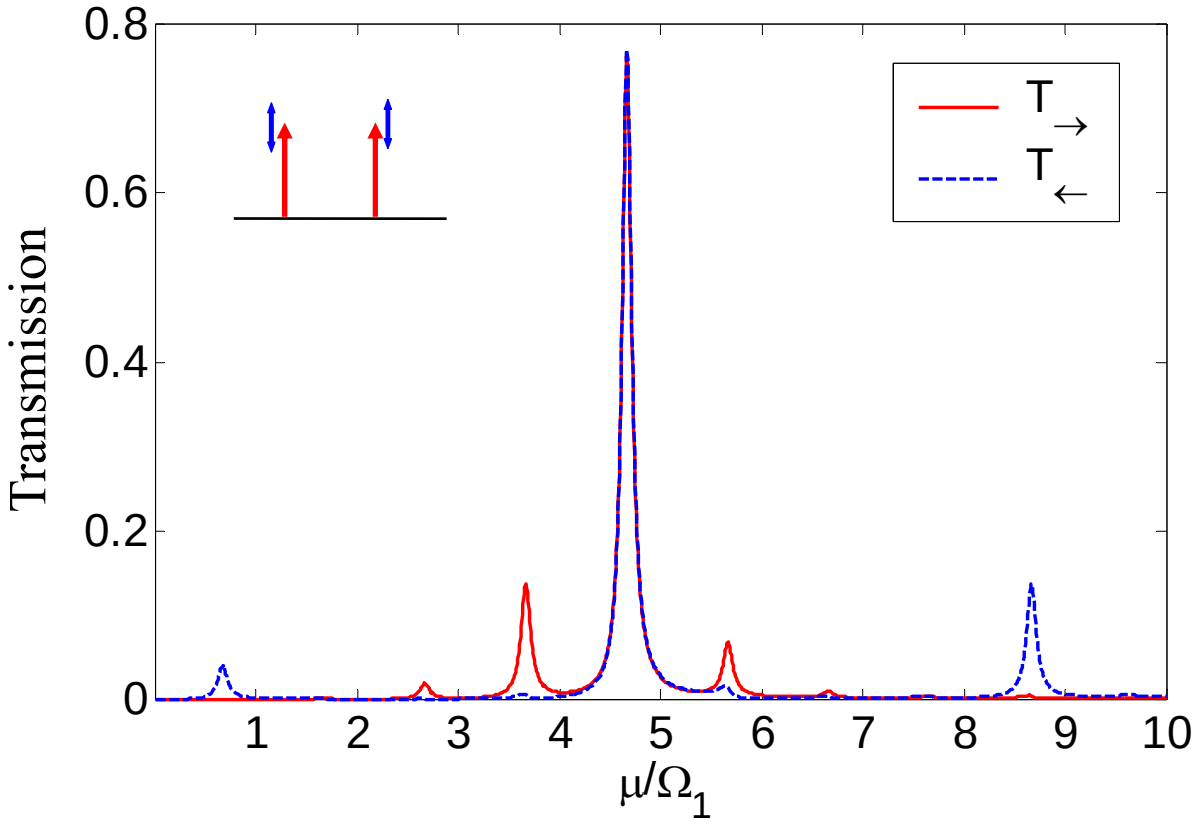

Fig. 4.5. Transmission as a function of μ for a=15, V_{s1}=V_{s2}=3, V_{d1}=V_{d2}=2, Ω_1=0.0084, and Ω_2=4Ω_1=0.0336.

Chapter 5
A Study on the Level Shifting in Time-modulated Transport

In this chapter, we demonstrate the resonance levels of several different conditions. Shifting of these states would be clearer under the numerical demonstrations in this section. We mentioned shifting of resonance states in Ch. 3 and Ch. 4, and we can further conclude that resonance states will shift under time-dependent modulations by the numerical results.

In the beginning of this section, we start with the formation of resonance states within symmetric static double barriers, and asymmetric static double barriers. Then, to see how the states shift, we modulate the barriers with time-dependent potentials including single-oscillation, and double-oscillation.

5.1 Static Symmetric Double Barriers

Resonance states are formed within in double-barrier configurations. These resonance levels, which correspond to longer life time, will be sharper and narrower if the confining potentials are strong. On contrary, resonance levels will be broader if the confining potentials are weak. Fig. 5.1 demonstrates resonance states of static double-barrier configuration with different confining amplitude.

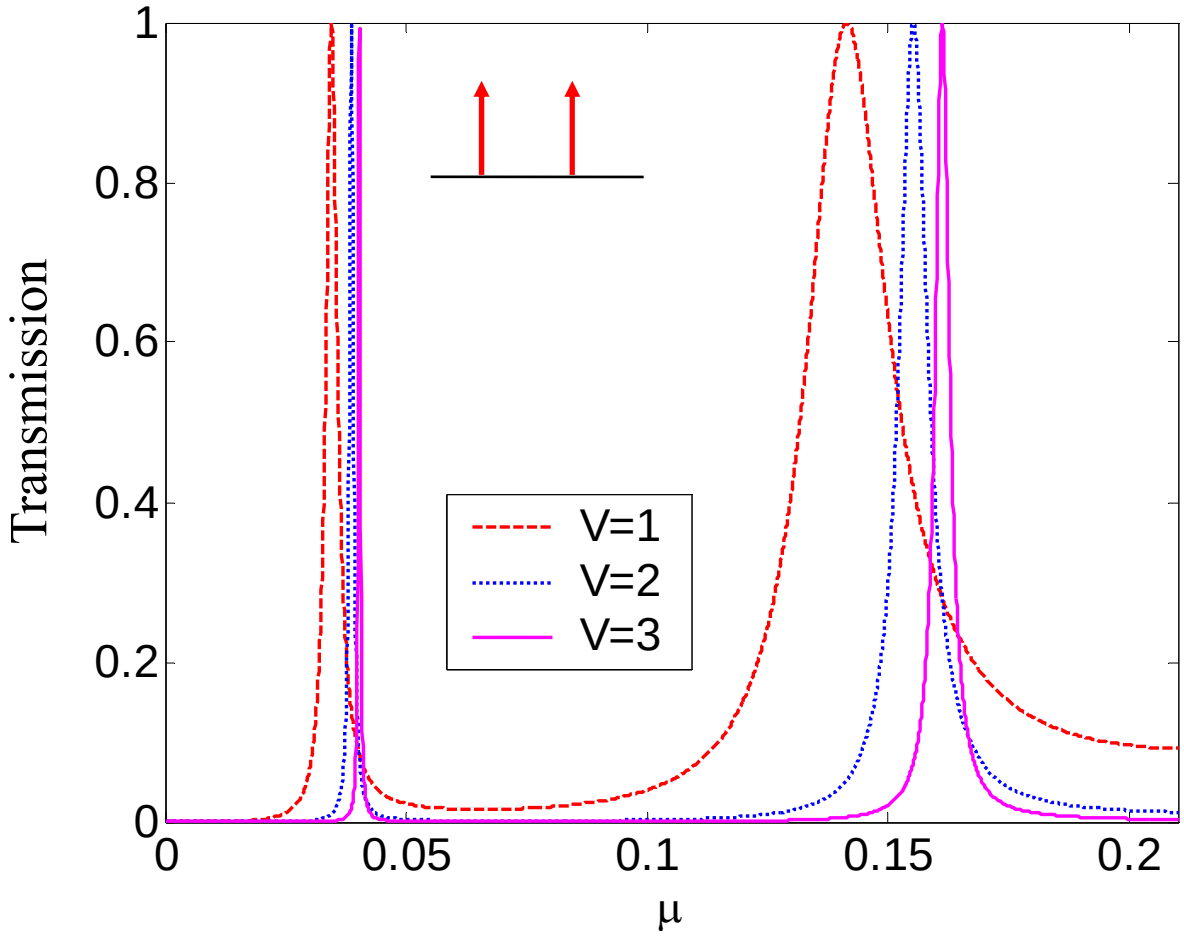

Fig. 5.1. Transmission as a function of μ for a=15, and $V_{s1}=V_{s2}=V$.

5.2 Static Asymmetric Double Barriers

We set up asymmetric double barriers to see how resonance states are apt to shift. In Fig. 5.2, we see that resonance states shift towards higher energy levels when δV is positive. Contrarily, resonance states shift towards lover energy levels if δV is negative. We also find that the peak value of resonance state in asymmetric double barriers will not achieve 1.

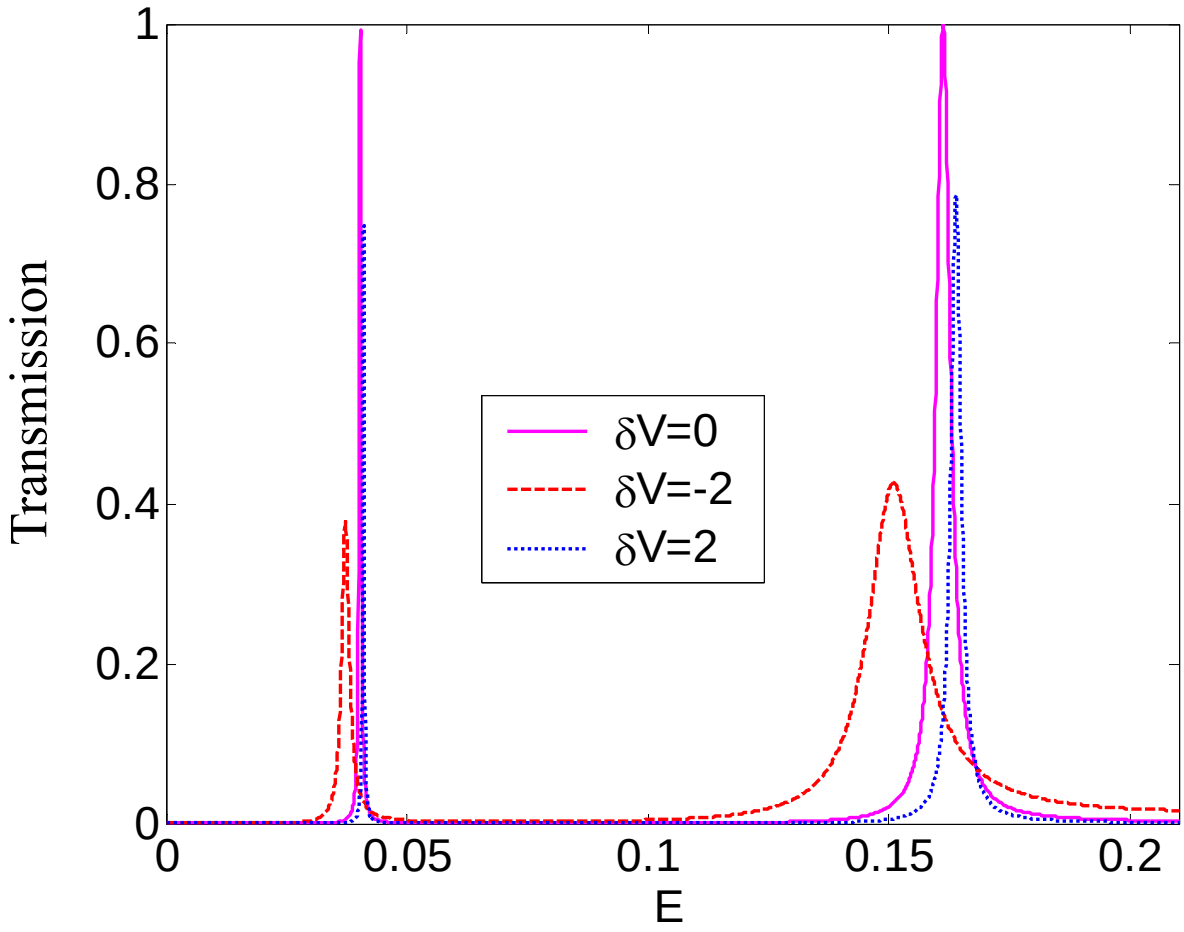

Fig. 5.2 . Transmission as a function of μ for a=15, V_{s1}=3, $V_{s2}=V+\delta V$.

5.3 Oscillating Barriers on Top of a Static Double Barrier

When applying time-dependent potentials, the magnitude of the confining barrier will change periodically. Therefore, resonance levels will also shift with time, but the overall effect (after time averaging) of the shift is towards lower-energy end. This can be referred back to Fig. 5.2. The degree of shifting towards lower energy is greater than that of shifting towards higher energy, making the overall effect shift to the left.

Fig. 5.3 and 5.4 demonstrate shifting of resonance state under time-dependent modulation. The amount of shifting will be enhanced, as shown in Fig. 5.4, when both of the barriers are time-dependent.

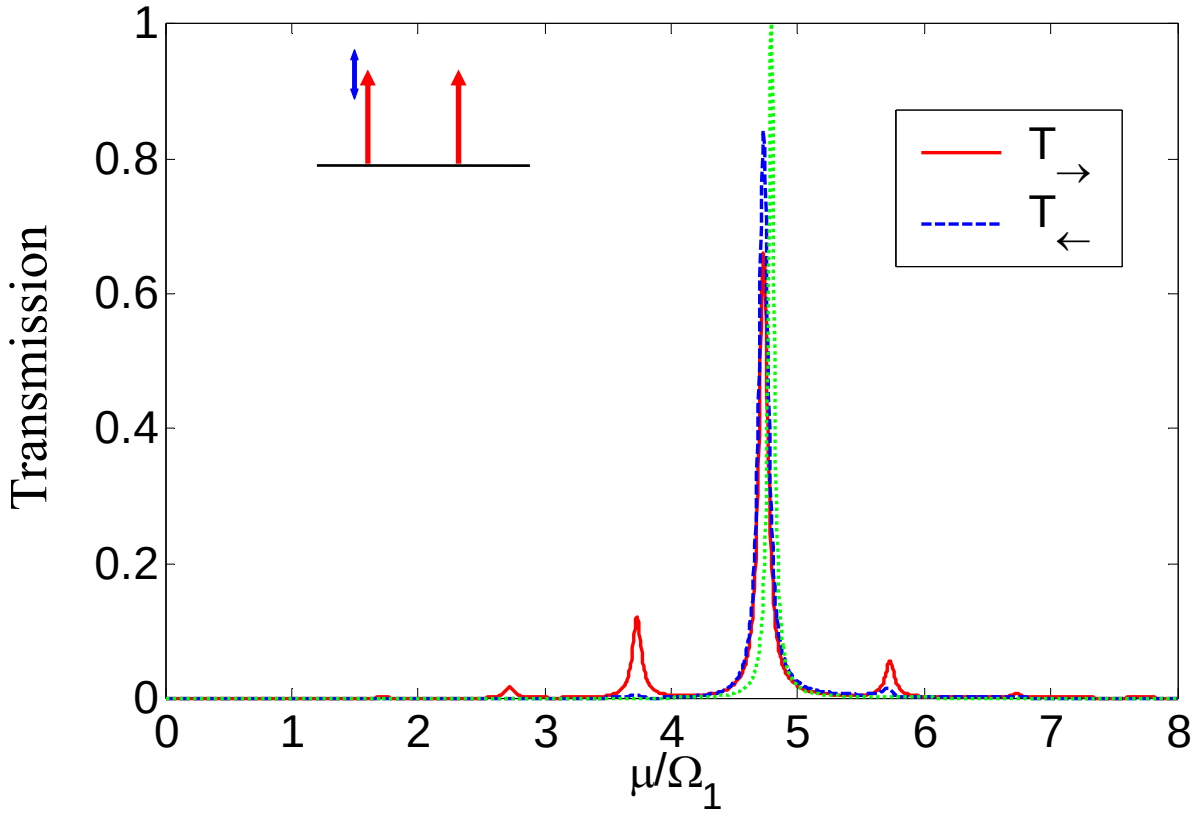

Fig. 5.3. Transmission as a function of μ for a=15, V_{s1}=V_{s2}=3, V_{d1}=2, V_{d2}=0, and Ω_1=0.0084. Dotted line represents the resonance state of the quantum dot without time-dependent potentials.

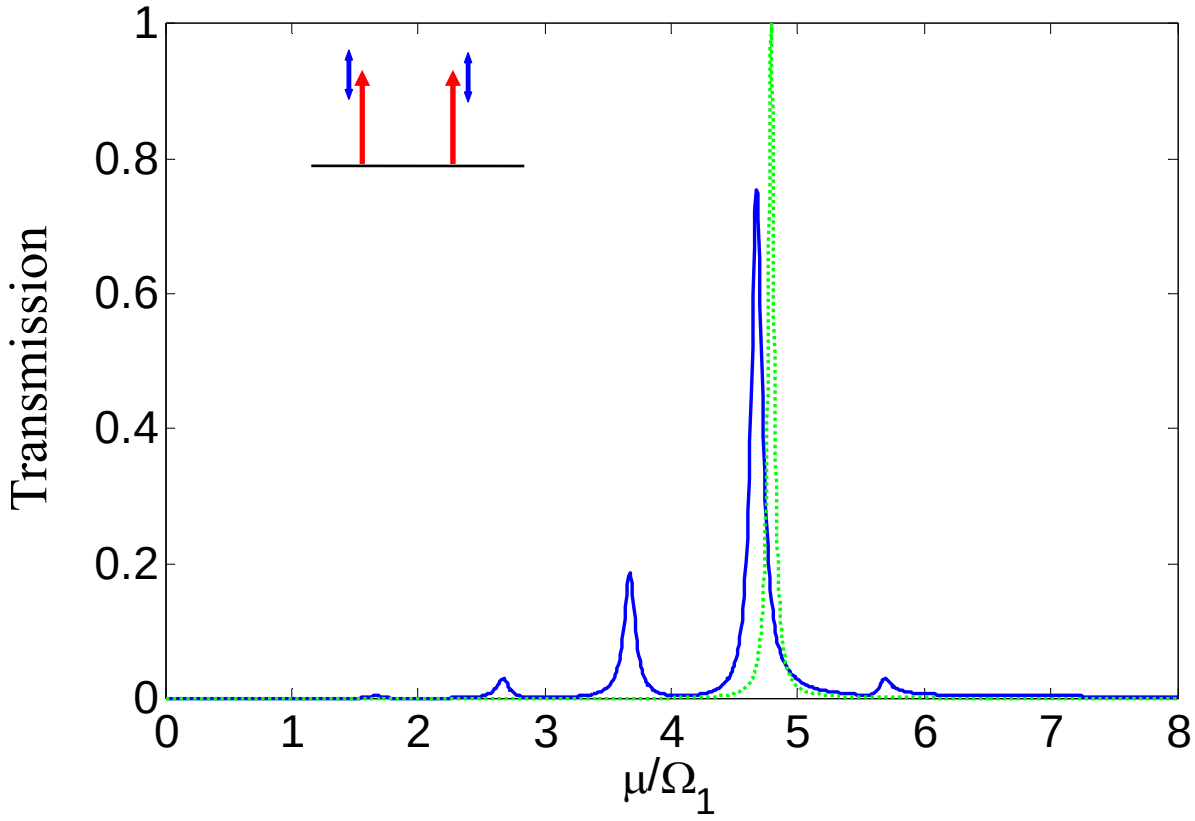

Fig. 5.4. Transmission as a function of μ for a=15, V_{s1}=V_{s2}=3, V_{d1}=V_{d2}=2, and Ω_1=Ω_2=0.0084. Dotted line represents the resonance state of the quantum dot without time-dependent potentials. When both the barriers are time-dependent, the amount of shifting is greater than that of Fig. 5.3.

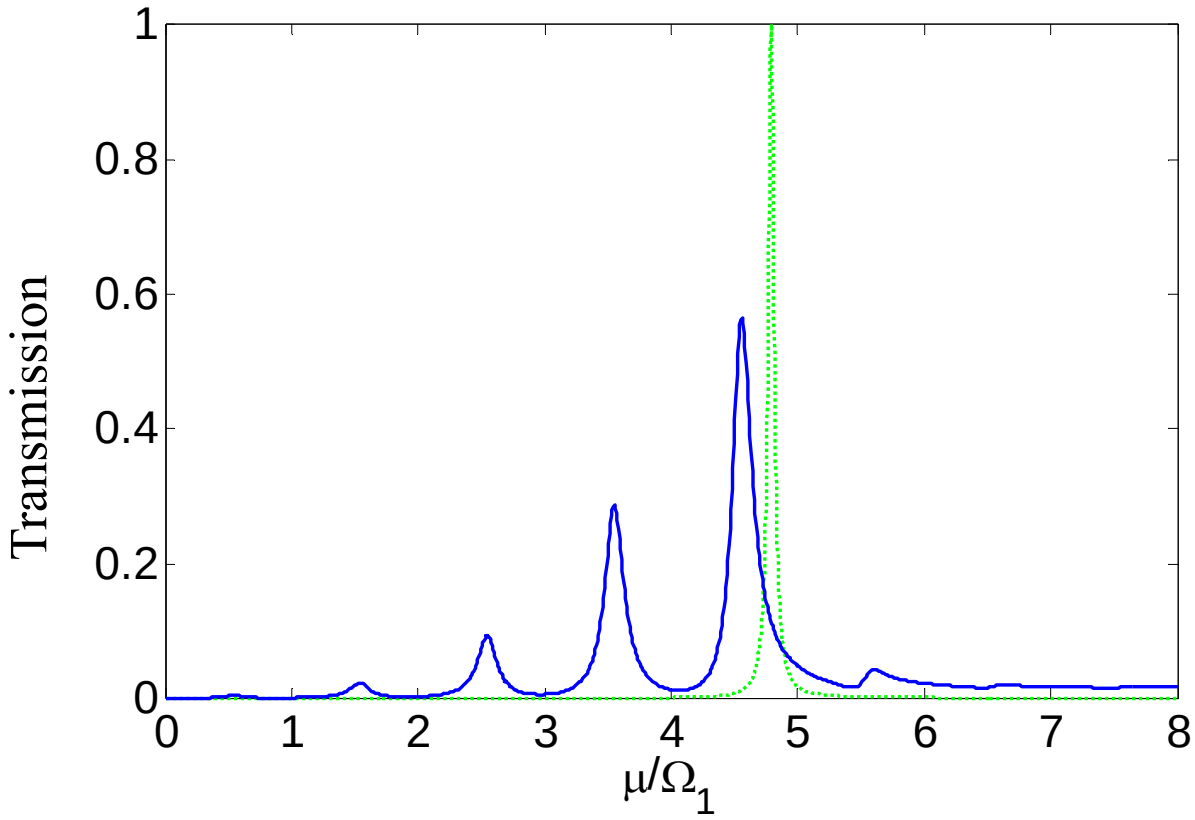

Fig. 5.5. Transmission as a function of μ for a=15, V_{s1}=V_{s2}=3, V_{d1}=V_{d2}=2.5, and Ω_1=Ω_2=0.0084.

Comparing Fig. 5.5 to Fig. 5.4, we can see that the amount of shifting of resonance state is also enhanced when the oscillation amplitude is stronger.

Chapter 6
Pumped Current

In Sec. 3.3, we see that $T_{\rightarrow}$ and $T_{\leftarrow}$ are much different under barrier-well configuration. Asymmetry of $T_{\rightarrow}$ and $T_{\leftarrow}$ is also shown in dual-frequency modulation. We calculated the pumped current of barrier-well configuration of same frequency modulation, and dual-frequency modulation, single oscillation of double-barrier configuration. In this chapter, we calculate the right-going transmission current by the equation

$$I = -\frac{2e}{h}\int_0^{E_F} dE\left[T_{\rightarrow}(E) - T_{\leftarrow}(E)\right]. \tag{6.1}$$

6.1 Barrier-well Configuration

Dependence of pumped current and transmission in barrier-configuration is given in Fig. 6.1. As shown in Fig. 6.1(a), pumped current is always negative within the energy range we calculate. This corresponds to the transmission feature in Fig. 6.1(b). $T_{\rightarrow}$ is greater than $T_{\leftarrow}$ in the energy scale $\mu < \varepsilon_r$ (ε_r is the resonance energy), hence the pumped current is negative by the definition in Eq. (6.1). The minimum value of the pumped current occurs at about at $\mu = \varepsilon_r$. When coming to the energy scale $\mu > \varepsilon_r$, $T_{\leftarrow}$ is greater than $T_{\rightarrow}$, thus electrons in this energy scale transport in the different direction, contributing positive current by the current definition given in Eq. (6.1). Therefore, pumped current starts to increase from the minimum value.

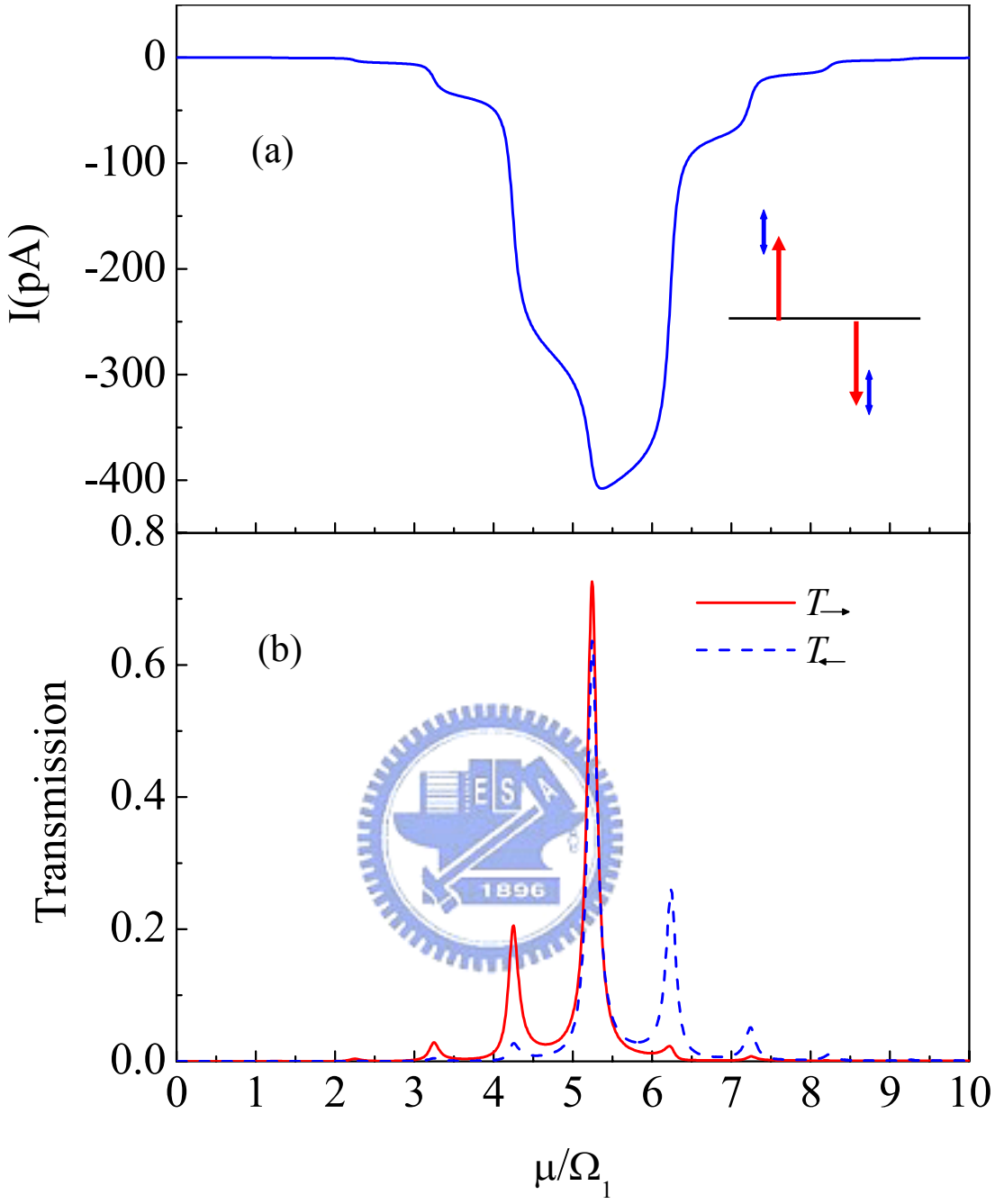

Fig. 6.1. (a) Pumped current for a=15, V_{s1}=3, V_{s2}=-3, V_{d1}=V_{d2}=2, and Ω_2=Ω_1=0.0084. (b) Transmission of the same parameters in (a).

6.2 Dual-frequency Modulation

From Fig. 6.2 (a), we can see that the pumped current has a plateau between μ=3Ω_1 and μ=3.5Ω_1. This is because current contribution of sideband channel ε_r–2Ω_1 is positive, and both $T_{\rightarrow}$ and $T_{\leftarrow}$ are almost zero within this scale. The similar effect also occurs between μ=6 Ω_1 and μ=6.5 Ω_1.

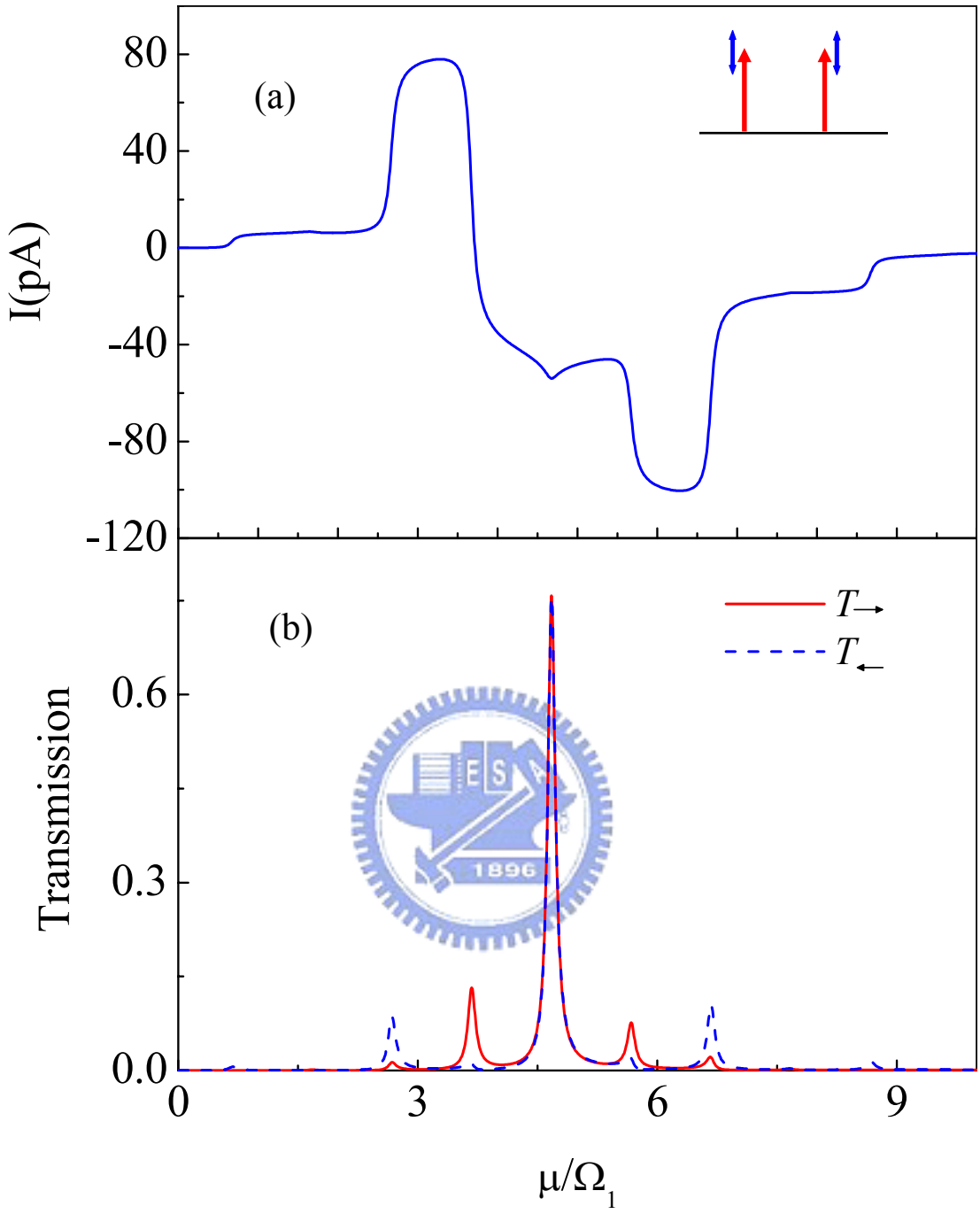

Fig. 6.2. (a) Pumped current for a=15, V_{s1}=V_{s2}=3, V_{d1}=V_{d2}=2, Ω_1=0.0084, and Ω_2=2Ω_1=0.0168. (b) Transmission of the same parameters in (a).

6.3 One Oscillating Barrier on Top of a Static Double Barrier

As shown in Fig. 6.3, the pumped current has a plateau between μ=2.5Ω_0 and μ=4.8Ω_0 because current contribution of sideband channel ε_r–2Ω_0 is positive, and

both $T_{\rightarrow}$ and $T_{\leftarrow}$ are almost zero within this scale.

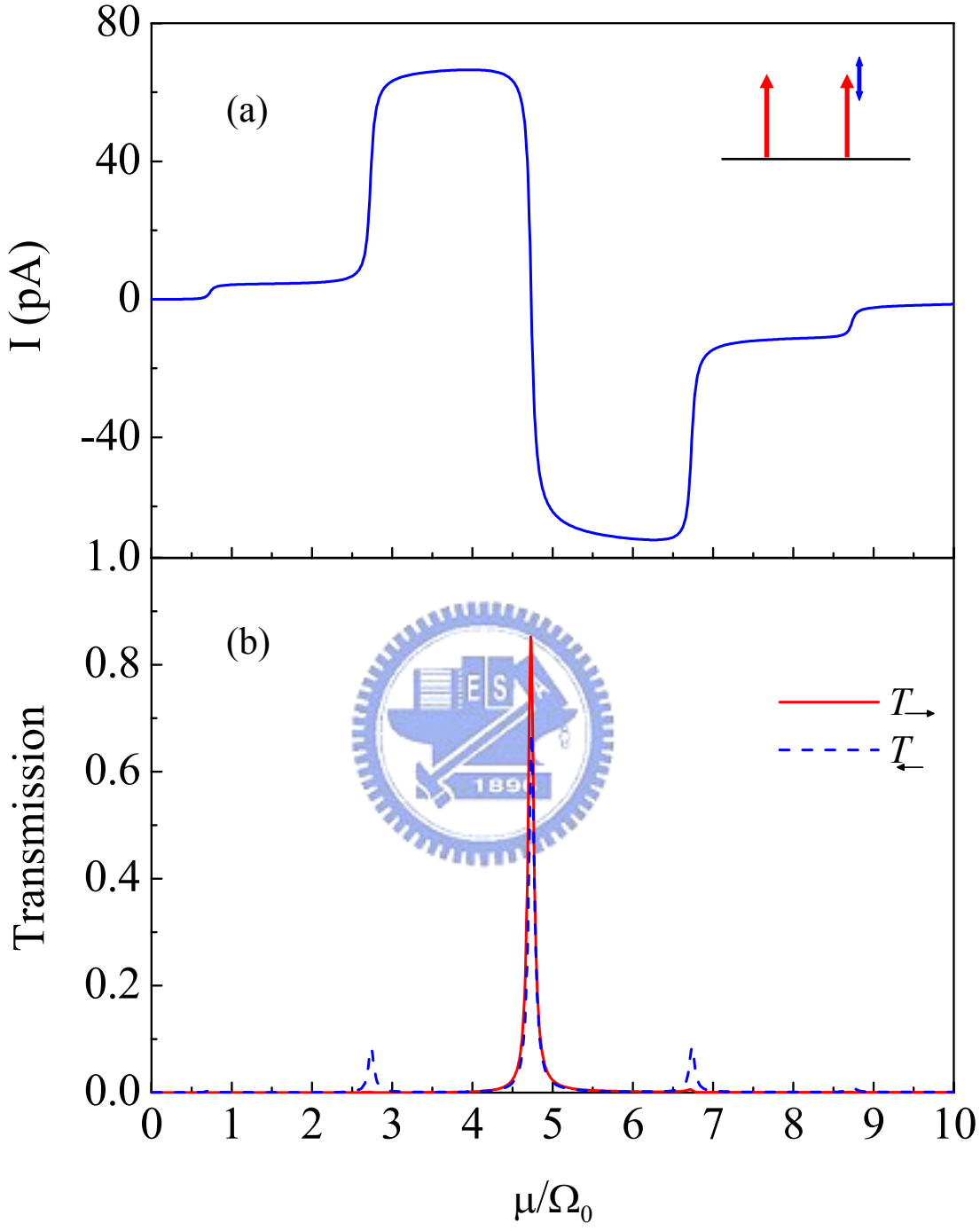

Fig. 6.3. (a) Pumped current for a=15, V_{s1}=V_{s2}=3, V_{d1}=0, V_{d2}=2, and Ω_2=2Ω_0=0.0168. (b) Transmission of the same parameters in (a).

Chapter 7
Unresolved Results

As mentioned in Ch. 3, we find an interesting feature when sidebands are near the subband bottom. As shown in Sec. 7.1, the relative magnitude of the sidepeaks next to the resonance state may reverse. In addition, quantum transport characteristics will be much different if the oscillation amplitude is greater than the static barrier.

Finally, we give the numerical result of oscillation frequency $\Omega < \Delta\varepsilon_n$ ($\Delta\varepsilon_n$ is the subband level spacing), where it is a complete different regime. Round time of electrons scattering between the barriers are much shorter than the oscillation frequency.

7.1 Near Subband Bottom Regime

From Fig. 7.1 and 7.2, oscillation frequency $\Omega_1=\Omega_2=0.0084$, the distance of two static barriers varies from 21 to 24 causing the resonance states and the sidebands, which we're interested in, move toward subband bottom. As shown in the figures, the relative strength of the two side peaks changes when the left sidepeak is approximately at energy of $1\Omega_1$. Fig. 7.3 and 7.4 are the transmission of frequency $\Omega_1=\Omega_2=0.042$. Fig. 7.5 to 7.7 demonstrate another oscillation frequency of $\Omega_1=\Omega_2=0.0672$.

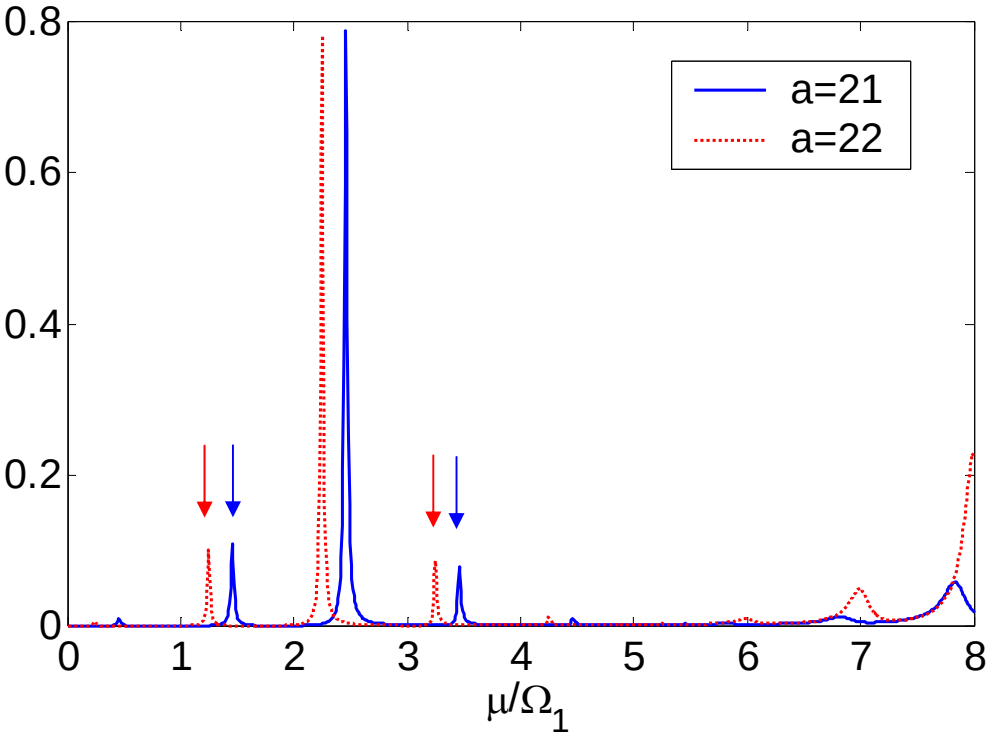

Fig. 7.1. Transmission as a function of μ for $V_{s1}=V_{s2}=3$, $V_{d1}=V_{d2}=2$, $\Omega_1=\Omega_2=0.0084$ under $a=21$, and $a=22$.

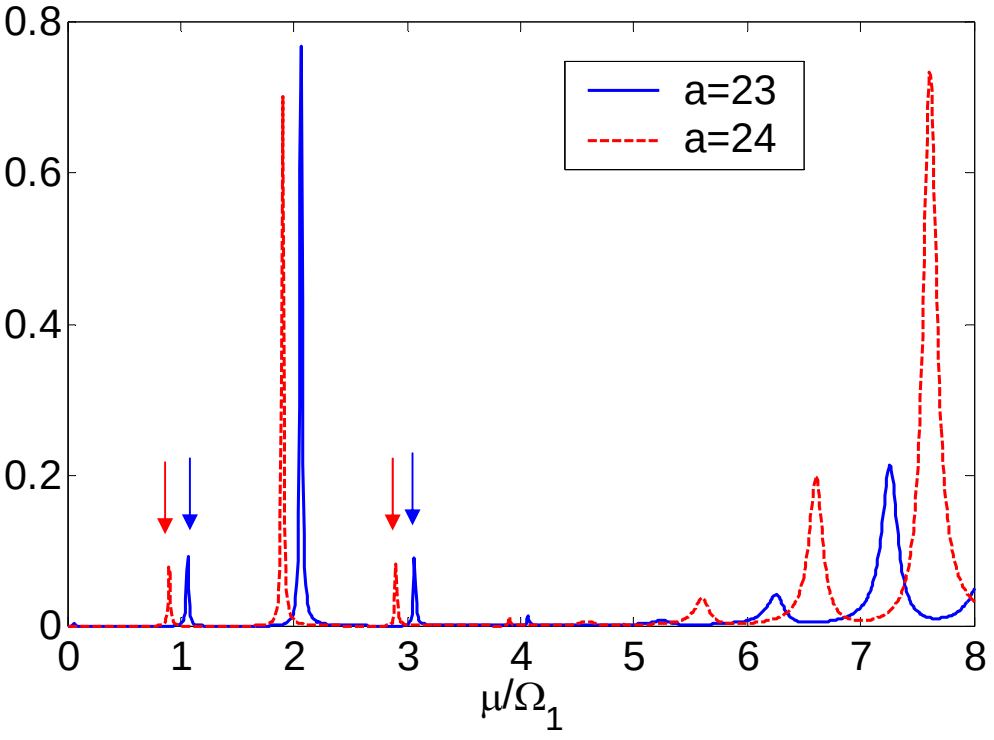

Fig. 7.2. Transmission as a function of μ for $V_{s1}=V_{s2}=3$, $V_{d1}=V_{d2}=2$, $\Omega_1=\Omega_2=0.0084$ under $a=23$, and $a=24$.

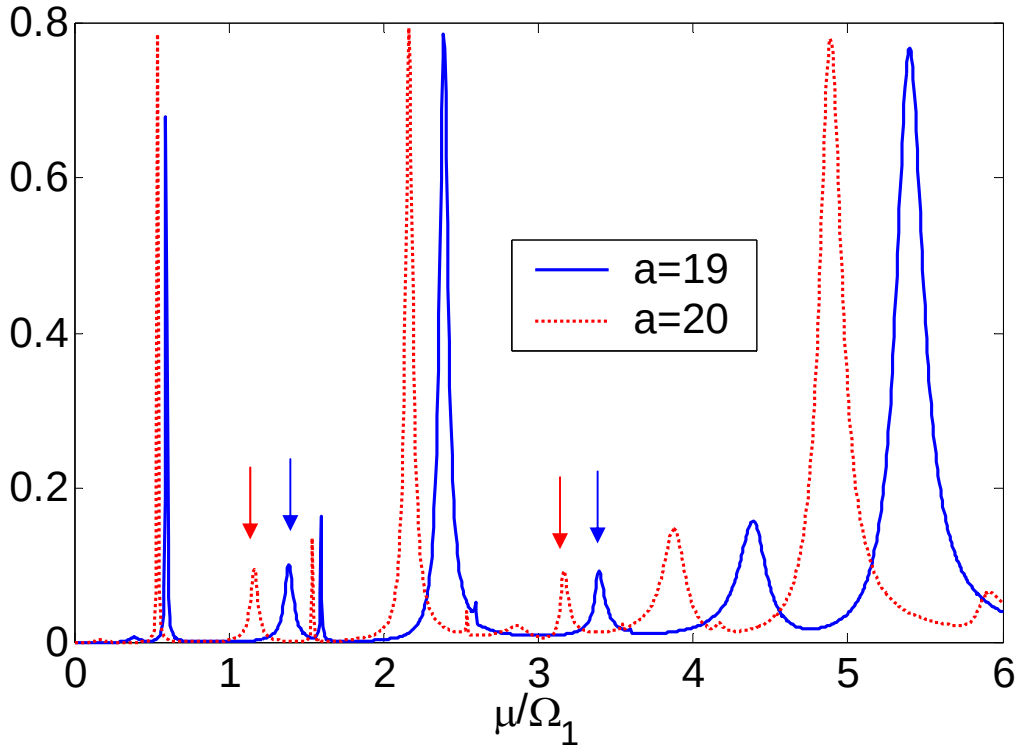

Fig. 7.3. Transmission of $V_{s1}=V_{s2}=3$, $V_{d1}=V_{d2}=2$, $\Omega_1=\Omega_2=0.042$ under $a=19$, and $a=20$.

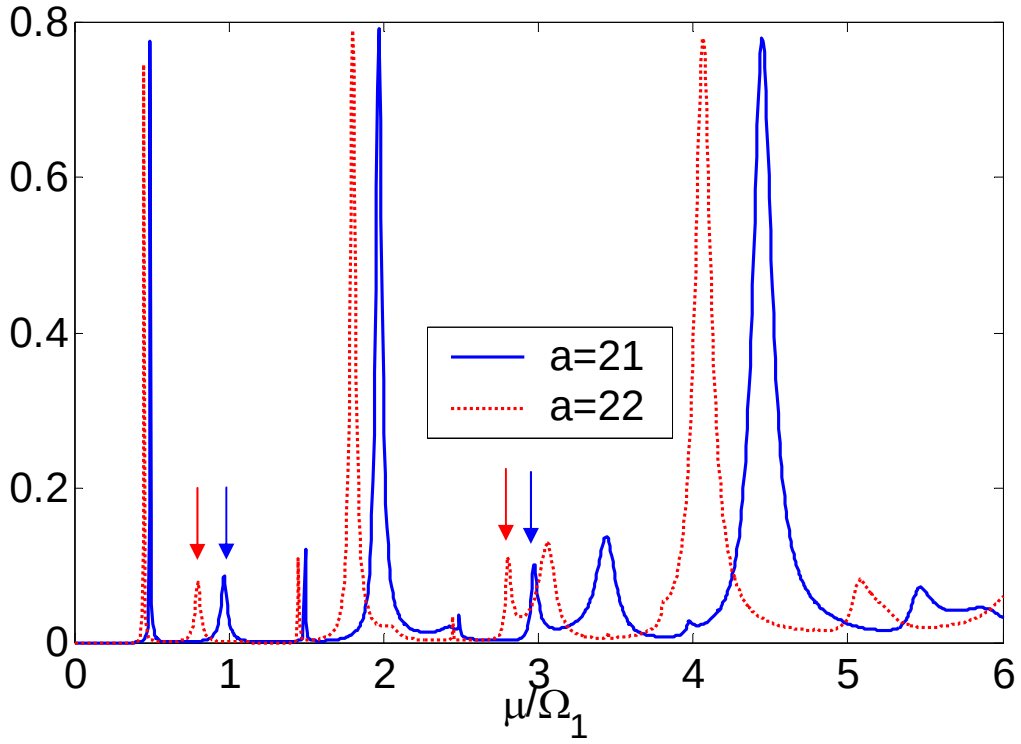

Fig. 7.4. Transmission of $V_{s1}=V_{s2}=3$, $V_{d1}=V_{d2}=2$, $\Omega_1=\Omega_2=0.042$ under $a=21$, and $a=22$.

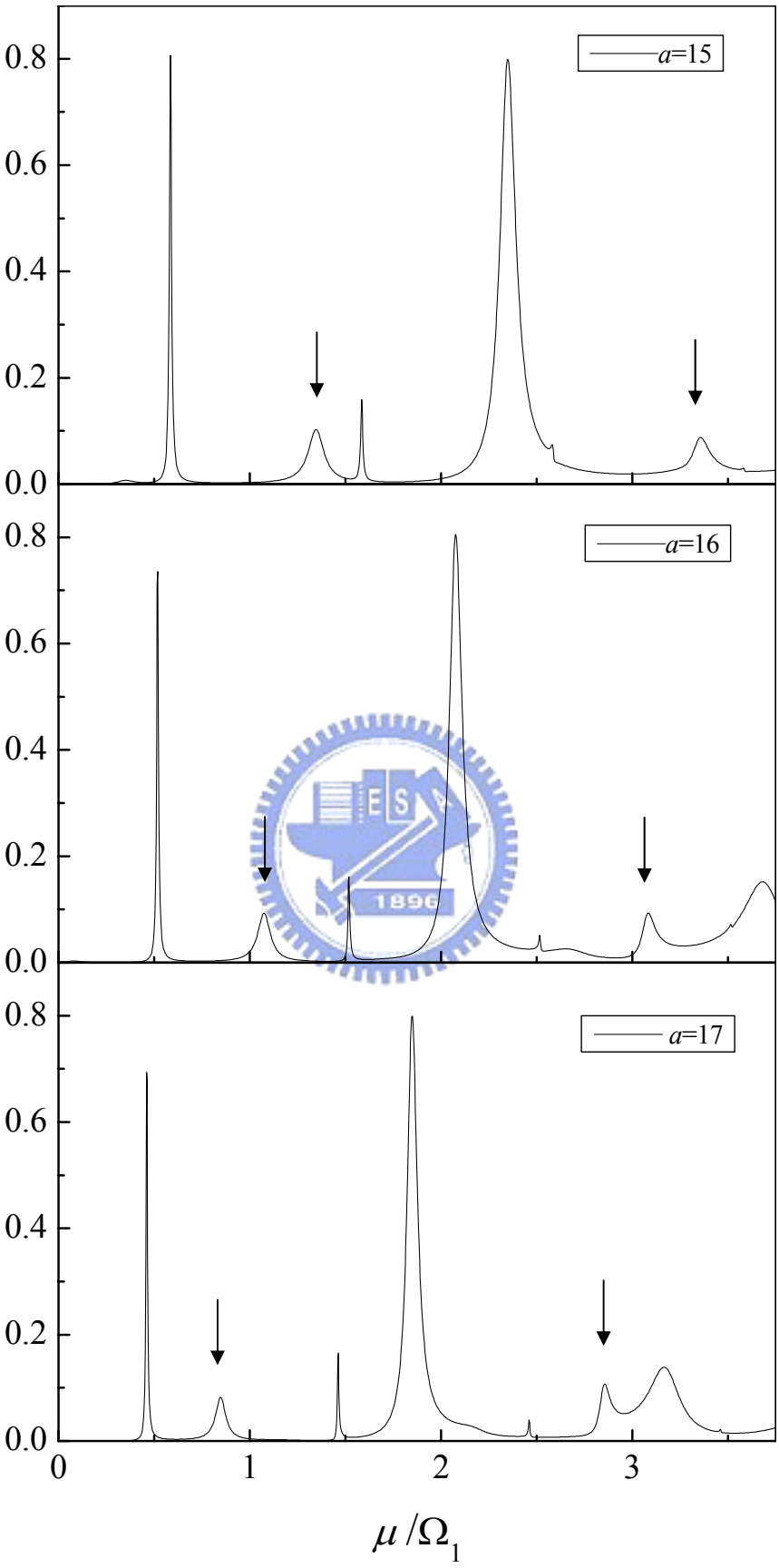

Fig. 7.5. Transmission as a function of μ for $V_{s1}=V_{s2}=3$, $V_{d1}=V_{d2}=2$, $\Omega_1=\Omega_2=0.0672$, and a=15 to 17.

7.2 Strong Oscillation

In Fig. 7.6 and 7.7, we find that resonance states shift towards higher energy levels when one of the oscillation amplitude is greater than that of the static barriers. In addition, for an electron that scatters with the strong oscillation potential first, its resonance transmission peak decreases rapidly. This feature is depicted by the dashed-line in Fig. 7.6 and 7.7. As to Fig. 7.8, under mono-frequency modulation, both of the oscillation amplitudes are strong, resonance peak shrinks to a small value.

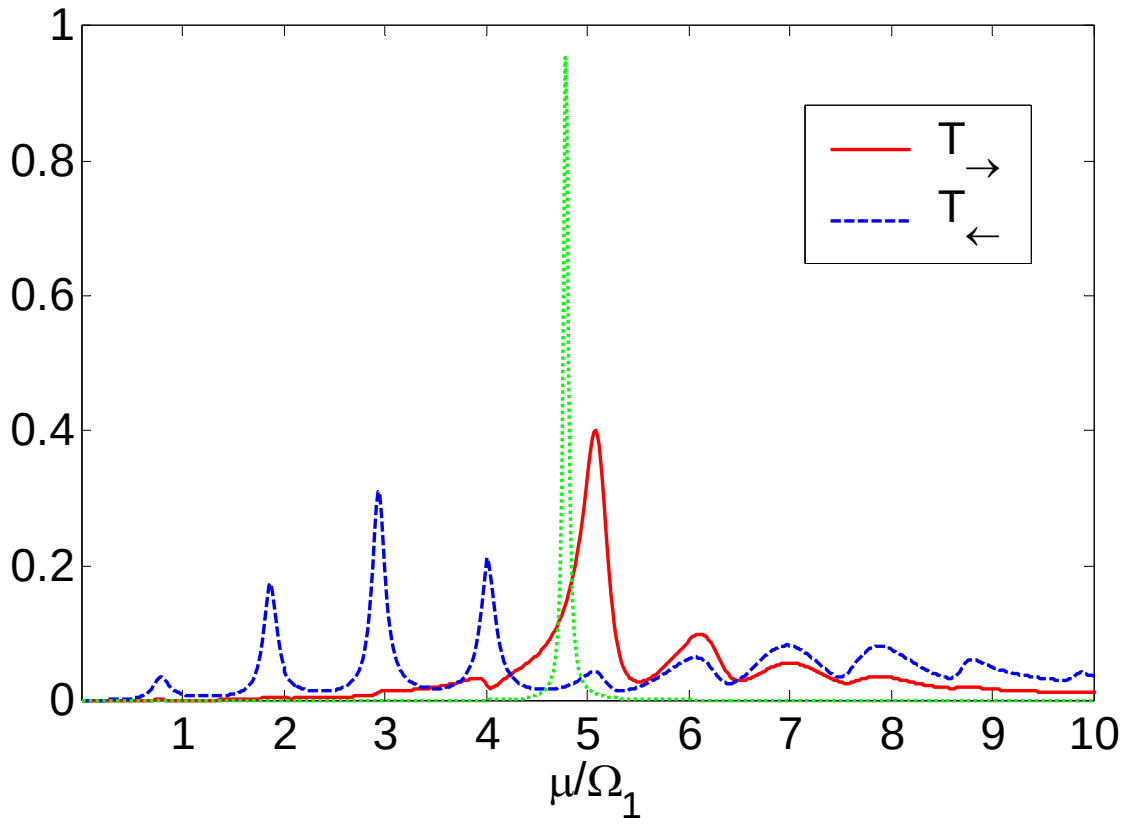

Fig. 7.6. Transmission as a function of μ for a=15, V_{s1}=V_{s2}=3, V_{d1}=2, V_{d2}=4, Ω_1=Ω_2=0.0084. Dotted line is the resonance state of double static barriers.

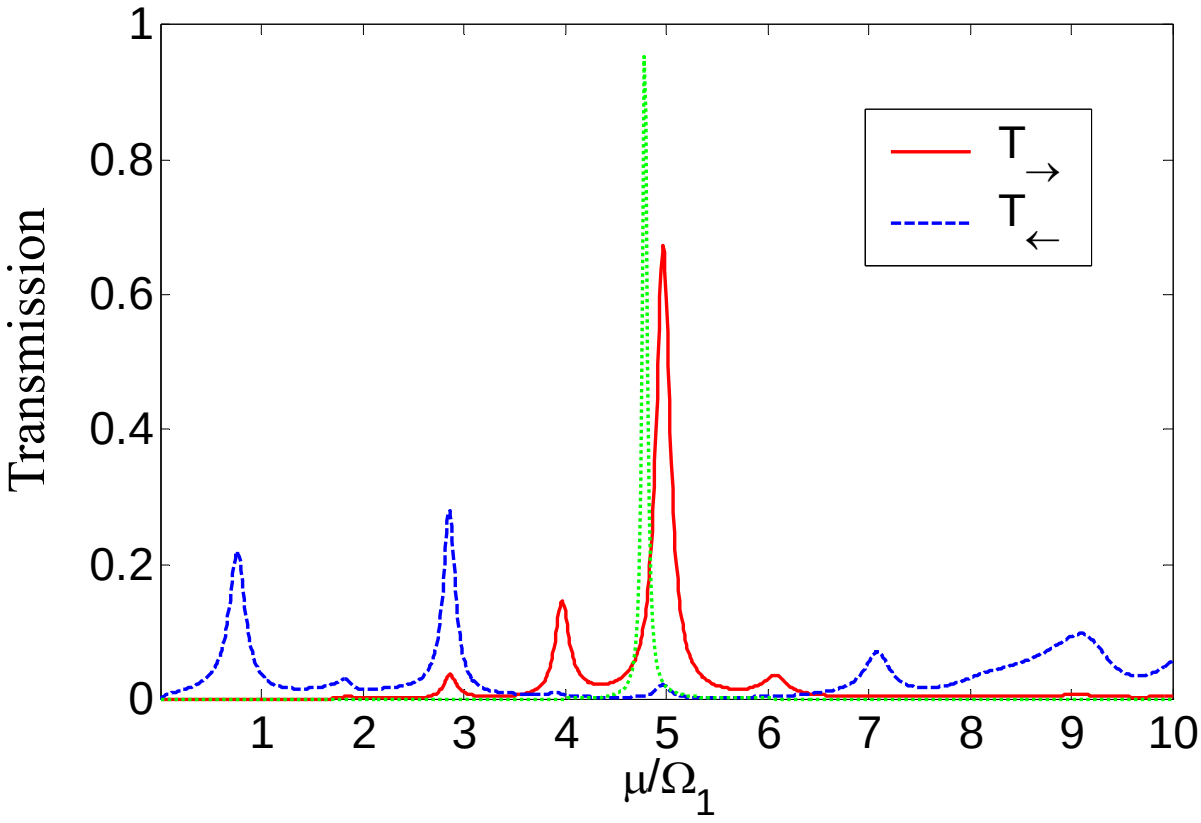

Fig. 7.7. Transmission as a function of μ a=15, V_{s1}=V_{s2}=3, V_{d1}=2, V_{d2}=4, Ω_1=0.0084, Ω_2=2Ω_1=0.0168. Dotted line is the resonance state of double static barriers.

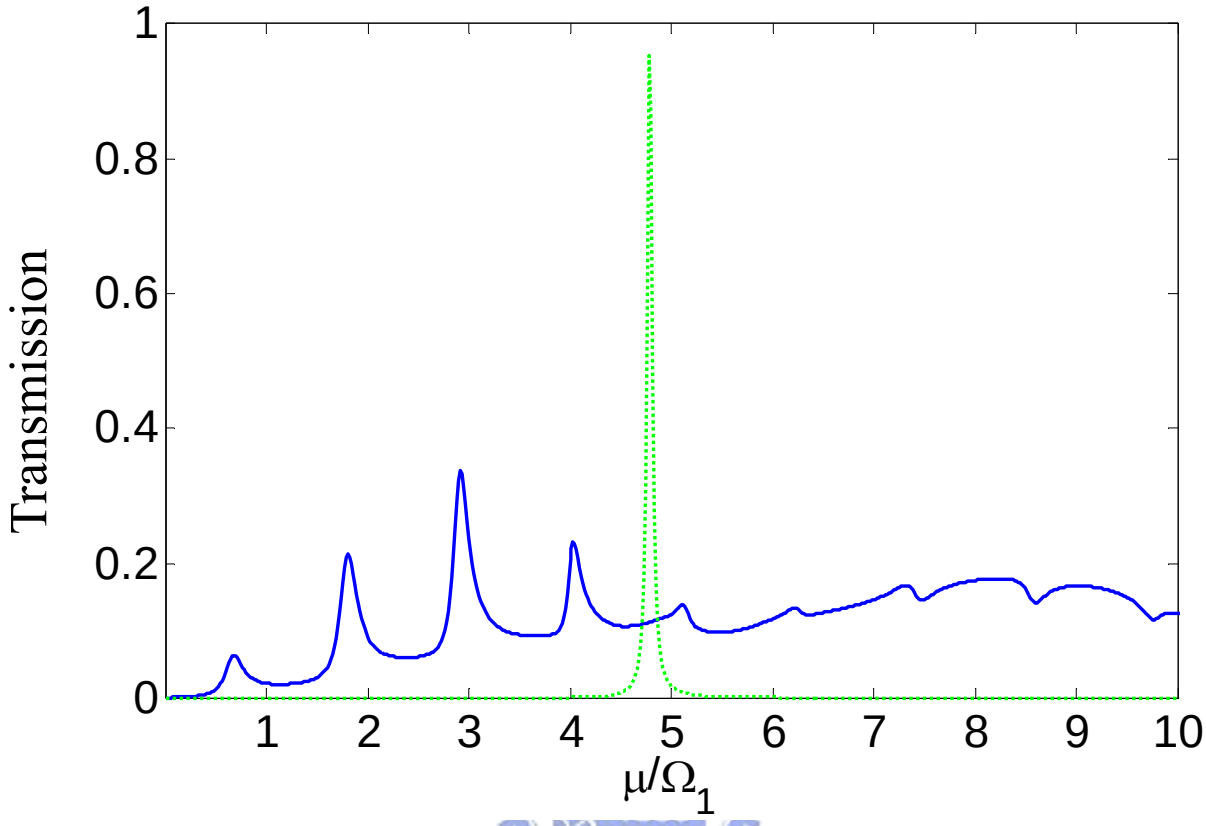

Fig. 7.8. Transmission as a function of μ a=15, V_{s1}=V_{s2}=3, V_{d1}=V_{d2}=4, Ω_1=Ω_2=0.0084. Dotted line is the resonance state of double static barriers.

7.3 Small Ω regime

In this subsection, we give the numerical results of a completely different regime, where oscillation frequency $\Omega < \Delta\varepsilon_n$ ($\Delta\varepsilon_n$ is the subband level spacing). Oscillation frequency in Fig. 7.9 and Fig. 7.10 are Ω_1=Ω_2=0.0014 and Ω_1=Ω_2=0.0028.

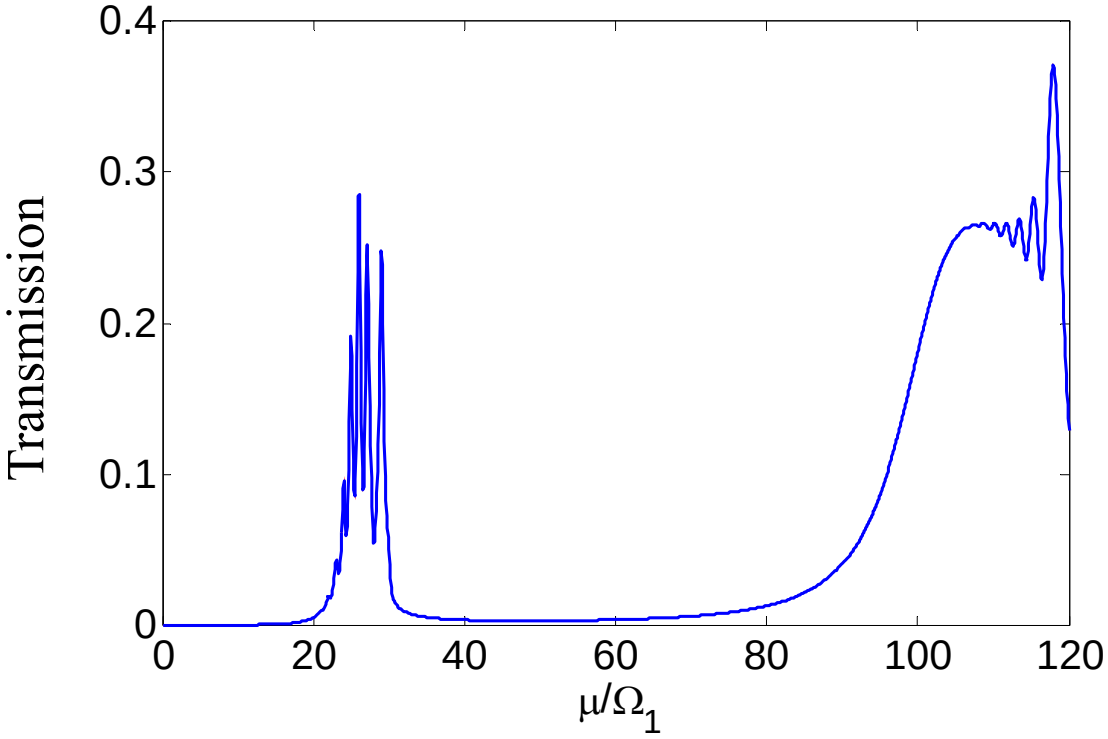

Fig. 7.9. Transmission as a function of μ for a=15, V_{s1}=V_{s2}=3, V_{d1}=V_{d2}=2, Ω_1=Ω_2=0.0014.

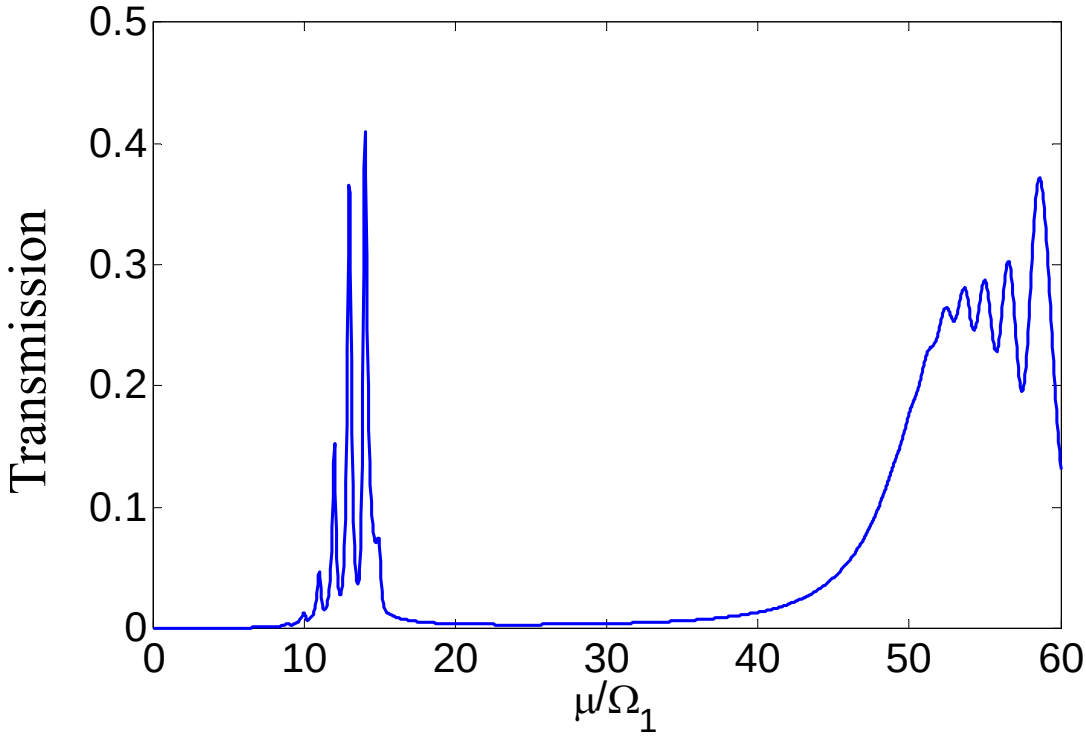

Fig. 7.10. Transmission as a function of μ for a=15, V_{s1}=V_{s2}=3, V_{d1}=V_{d2}=2, Ω_1=Ω_2=0.0028.

Chapter 8
Discussion and Future Research

It is an interesting feature to see characteristics of sideband asymmetry because many of us may, at the first time, intuitively take electrons to have the same probability of absorbing or emitting photons. For now, we can be sure that the electrons tend to absorb or emit photons under specific configurations, and the asymmetric sideband channels can be balanced when we introduce a phase difference into the system. Even electrons incident from the opposite sides of the system may exhibit different tendency of absorbing or emitting photons.

Under double-barrier configuration, it is now clear from one-photon approximation that the cause of asymmetric sidebands comes mainly from the interference terms. This approximation gives still good results even if the oscillation amplitudes are strong, that is, when higher-order sideband channels appear. We may conclude that of the two sideband channels we study, the most important interaction process is 1^{st}-order interaction.

In dual-frequency modulation, we see that electrons have more effective interaction with the time-dependent potential they meet first. $T_{\rightarrow}$ and $T_{\leftarrow}$ are different due to the fact that spatial-invariance is destroyed under dual-frequency modulation. Net pumped current can be achieved one translational-invariance is destroyed.

There are still features we like to understand. We are interested in the mechanism which reverses the relative strength of transmission for the sideband channels we study, and also the reasons why resonance transmission shrinks to a small value under strong oscillation conditions.

Appendix A

Set-up of Matrix Equations for Time-dependent Mode Matching

In this section, we give in detail the set-up of matrix equations given in Sec. 2.1. We program our numerical calculation program on the basis of these matrix equations.

After matching the boundary conditions in Sec. 2.1, we have Eq. (2.5) to (2.8). Eq. (2.5)×$k_n(m)$ + Eq. (2.6) gives

$$\begin{aligned}\delta_{m,0}\left(k_n+k_n(m)\right)e^{-ik_n\frac{a}{2}} &= 2A_n(m)k_n(m)e^{-ik_n(m)\frac{a}{2}} \\ &+iV_{s1}\left(A_n(m)e^{-ik(m)\frac{a}{2}}+B_n(m)e^{ik(m)\frac{a}{2}}\right) \\ &+\frac{i}{2}V_{d1}\left(A_n(m+1)e^{-ik_n(m+1)\frac{a}{2}}+A_n(m-1)e^{-ik_n(m-1)\frac{a}{2}}\right), \\ &+\frac{i}{2}V_{d1}\left(B_n(m+1)e^{k_n(m+1)\frac{a}{2}}+B_n(m-1)e^{ik_n(m-1)\frac{a}{2}}\right)\end{aligned} \tag{A.1}$$

and Eq. (2.7)×$k_n(m)$ – Eq. (2.8) gives

$$\begin{aligned}0 &= 2B_n(m)k_n(m)e^{-ik_n(m)\frac{a}{2}} \\ &+iV_{s2}\left(A_n(m)e^{ik_n(m)\frac{a}{2}}+B_n(m)e^{-ik_n(m)\frac{a}{2}}\right) \\ &+\frac{i}{2}V_{d2}\left(A_n(m+N)e^{i\phi}e^{ik_n(m+N)\frac{a}{2}}+A_n(m-N)e^{-i\phi}e^{ik_n(m-N)\frac{a}{2}}\right) \\ &+\frac{i}{2}V_{d2}\left(B_n(m+N)e^{i\phi}e^{-ik_n(m+N)\frac{a}{2}}+B_n(m-N)e^{-i\phi}e^{-ik_n(m-N)\frac{a}{2}}\right)\end{aligned} \tag{A.2}$$

In calculation of $A_n(m)$ and $B_n(m)$, we set up the matrix equation

$$\begin{bmatrix}C_1\\C_2\end{bmatrix}=\begin{bmatrix}M_{11} & M_{12}\\M_{21} & M_{22}\end{bmatrix}\begin{bmatrix}A\\B\end{bmatrix}$$

in Eq. (2.9).

When we consider 2M+1 sidebands, *l*=M… 0…－M, and *m*=M… 0…－M. Matrix elements in Eq. (2.9) will be

$$M_{11}=\delta_{l,m}\left[\left(2k_n(m)+iV_{s1}\right)e^{-ik_n(m)\frac{a}{2}}\right]+\delta_{l,m-1}\left[\frac{i}{2}V_{d1}e^{-ik_n(m)\frac{a}{2}}\right]+\delta_{l,m+1}\left[\frac{i}{2}V_{d1}e^{-ik_n(m)\frac{a}{2}}\right], \quad (A.3)$$

$$M_{12}=\delta_{l,m}\left[iV_{s1}e^{ik_n(m)\frac{a}{2}}\right]+\delta_{l,m-1}\left[\frac{iV_{d1}}{2}e^{ik_n(m)\frac{a}{2}}\right]+\delta_{l,m+1}\left[\frac{iV_{d1}}{2}e^{ik_n(m)\frac{a}{2}}\right], \quad (A.4)$$

$$M_{21}=\delta_{l,m}\left[iV_{s2}e^{ik_n(m)\frac{a}{2}}\right]+\delta_{l,m-N}\left[\frac{iV_{d2}}{2}e^{i\phi}e^{ik_n(m)\frac{a}{2}}\right]+\delta_{l,m+N}\left[\frac{iV_{d2}}{2}e^{-i\phi}e^{ik_n(m)\frac{a}{2}}\right], \quad (A.5)$$

$$M_{22}=\delta_{l,m}\left[\left(2k_n(m)+iV_{s2}\right)e^{-ik_n(m)\frac{a}{2}}\right]+\delta_{l,m-N}\left[\frac{iV_{d2}}{2}e^{i\phi}e^{-ik_n(m)\frac{a}{2}}\right]+\delta_{l,m+N}\left[\frac{iV_{d2}}{2}e^{-i\phi}e^{-ik_n(m)\frac{a}{2}}\right], \quad (A.6)$$

$$C_1=\begin{bmatrix}\vdots\\0\\2k_ne^{-ik_n\frac{a}{2}}\\0\\\vdots\end{bmatrix}, \quad (A.7)$$

$$C_2 = \begin{bmatrix} \vdots \\ 0 \\ \vdots \end{bmatrix}. \qquad \text{(A.8)}$$

From Eq. (2.10), we have

$$r_n(m) = A_n(m)e^{-ik_n(m)a} + B_n(m) - \delta_{p,0}e^{-i\left(k_n + k_n(m)\right)\frac{a}{2}}$$
$$t_n(m) = A_n(m) + B_n(m)e^{-ik_n(m)a}$$

We then set up the matrix equation as

$$\begin{bmatrix} r_n \\ t_n \end{bmatrix} = \begin{bmatrix} P_{11} & P_{12} \\ P_{21} & P_{22} \end{bmatrix} \begin{bmatrix} A_n \\ B_n \end{bmatrix} + \begin{bmatrix} D_1 \\ D_2 \end{bmatrix}$$

in calculation of $r_n(m)$ and $t_n(m)$. Again, for l=M… 0…－M, and m=M… 0…－M, matrix elements in the above equation will be

$$P_{11} = P_{22} = \delta_{l,m}e^{-ik_n(m)a},$$

$$P_{12} = P_{21} = I,$$

$$D_1 = \begin{bmatrix} \vdots \\ 0 \\ -e^{ik_n a} \\ 0 \\ \vdots \end{bmatrix},$$

$$D_2 = \begin{bmatrix} \vdots \\ 0 \\ \vdots \end{bmatrix}.$$

In calculation for $T_{\leftarrow}$, $\tilde{t}_n$ and $\tilde{r}_n$ can be solved in the similar way of setting up the matrix equations.

Appendix B

Analytical Expressions for One-photon Approximation

In this section, we give the analytical expression of reflection and transmission coefficients in one-sideband approximation. After matching the boundary conditions of a single oscillating barrier applied at x=0, we have

$$r_1^I(\mu) = t_1^I(\mu) \tag{B.1}$$

$$1 + r_0^I(\mu) = t_0^I(\mu) \tag{B.2}$$

$$r_{-1}^I(\mu) = t_{-1}^I(\mu) \tag{B.3}$$

$$-ik(1)\left[r_1^I(\mu) + t_1^I(\mu)\right] + V_s t_1^I(\mu) + \frac{V_d}{2} e^{-i\phi} t_0^I(\mu) = 0 \tag{B.4}$$

$$ik(0)\left[1 - r_0^I(\mu) - t_0^I(\mu)\right] + V_s t_0^I(\mu) + \frac{V_d}{2}\left[e^{i\phi} t_1^I(\mu) + e^{-i\phi} t_{-1}^I(\mu)\right] = 0 \tag{B.5}$$

$$-ik(-1)\left[r_{-1}^I(\mu) + t_{-1}^I(\mu)\right] + V_s t_1^I(\mu) + \frac{V_d}{2} e^{i\phi} t_0^I(\mu) = 0 \tag{B.6}$$

After solving the above equations, we have

$$t_1^I(\mu) = \frac{-2ik(0)Vd\left[iV_s + 2k(-1)\right]e^{-i\phi}}{2\left[2k(0) + iV_s\right]\left[iV_s + 2k(-1)\right]\left[iV_s + 2k(1)\right] + V_d^2\left[iV_s + k(-1) + k(1)\right]} \tag{B.7}$$

$$t_0^I(\mu) = \frac{4k(0)\left[iV_s + 2k(-1)\right]\left[iV_s + 2k(1)\right]}{2\left[2k(0) + iV_s\right]\left[iVs + 2k(-1)\right]\left[iV_s + 2k(1)\right] + V_d^2\left[iV_s + k(-1) + k(1)\right]} \tag{B.8}$$

$$t_{-1}^I(\mu) = \frac{-2ik(0)Vd\left[iV_s + 2k(1)\right]e^{i\phi}}{2\left[2k(0) + iV_s\right]\left[iV_s + 2k(-1)\right]\left[iV_s + 2k(1)\right] + V_d^2\left[iV_s + k(-1) + k(1)\right]} \tag{B.9}$$

$$r_1^I(\mu) = \frac{-2ik(0)Vd\left[iV_s + 2k(-1)\right]e^{-i\phi}}{2\left[2k(0) + iV_s\right]\left[iV_s + 2k(-1)\right]\left[iV_s + 2k(1)\right] + V_d^2\left[iV_s + k(-1) + k(1)\right]} \tag{B.10}$$

$$r_0^I(\mu)=\frac{-2iV_s\left[iV_s+2k(-1)\right]\left[iV_s+2k(1)\right]-V_d^2\left[iV_s+k(-1)+k(1)\right]}{2\left[2k(0)+iV_s\right]\left[iV_s+2k(-1)\right]\left[iV_s+2k(1)\right]+V_d^2\left[iV_s+k(-1)+k(1)\right]} \quad \text{(B.11)}$$

$$r_{-1}^I(\mu)=\frac{-2ik(0)Vd\left[iV_s+2k(1)\right]e^{i\phi}}{2\left[2k(0)+iV_s\right]\left[iV_s+2k(-1)\right]\left[iV_s+2k(1)\right]+V_d^2\left[iV_s+k(-1)+k(1)\right]} \quad \text{(B.12)}$$

We specially note that within Eq. (B.5) to (B.12), V_d^2 in the denominator can be expanded into series of $(V_d^2)^n$. Hence, we omit this term in each denominator of the coefficients for one-photon approximation. V_d^2 in Eq. (B.11) is omitted as well.

After doing the simplification, we have

$$t_1^I(\mu)=\frac{-ik(0)V_de^{-i\phi}}{\left[2k(0)+iV_s\right]\left[iV_s+2k(1)\right]} \quad \text{(B.13)}$$

$$t_0^I(\mu)=\frac{2k(0)}{\left[2k(0)+iV_s\right]} \quad \text{(B.14)}$$

$$t_{-1}^I(\mu)=\frac{-ik(0)V_de^{i\phi}}{\left[2k(0)+iV_s\right]\left[iV_s+2k(-1)\right]} \quad \text{(B.15)}$$

$$r_1^I(\mu)=\frac{-ik(0)V_de^{-i\phi}}{\left[2k(0)+iV_s\right]\left[iV_s+2k(1)\right]} \quad \text{(B.16)}$$

$$r_0^I(\mu)=\frac{-iV_s}{\left[2k(0)+iV_s\right]} \quad \text{(B.17)}$$

$$r_{-1}^I(\mu)=\frac{-ik(0)V_de^{i\phi}}{\left[2k(0)+iV_s\right]\left[iV_s+2k(-1)\right]} \quad \text{(B.18)}$$

As mentioned in Ch. 2, reflection and transmission coefficients of a barrier located at interface *II* ($x=a$) will be

$$\begin{cases} r_m^{II}(\mu)=r_m^I(\mu)e^{i[k(m)+k(0)]a} \\ t_m^{II}(\mu)=t_m^I(\mu)e^{-i[k(m)-k(0)]a} \end{cases}.$$

Thus, in Sec. 2.3, the 8 processes of one-photon approximation will be

$$t\left(t_1^I,\mu\right)=\frac{t_1^I(\mu)t_0^{II}(\mu+\Omega)}{1-r_0^{II}(\mu+\Omega)\tilde{r}_0^I(\mu+\Omega)}=\frac{t_1^I(\mu)t_0^I(\mu+\Omega)}{1-\left[r_0^I(\mu+\Omega)\right]^2e^{i2k(1)a}} \quad \text{(B.19)}$$

$$t\left(t_1^{II},\mu\right)=\frac{t_0^I(\mu)t_1^{II}(\mu)}{1-r_0^{II}(\mu)\tilde{r}_0^I(\mu)}=\frac{t_0^I(\mu)t_1^I(\mu)e^{-i\left[k(1)-k(0)\right]a}}{1-\left[r_0^I(\mu)\right]^2e^{i2k(0)a}} \tag{B.20}$$

$$t\left(\tilde{r}_1^I,\mu\right)=\frac{\dfrac{t_0^I(\mu)r_0^{II}(\mu)\tilde{r}_1^I(\mu)t_0^{II}(\mu+\Omega)}{1-\left[r_0^{II}(\mu+\Omega)\tilde{r}_0^I(\mu+\Omega)\right]}}{1-\left[\tilde{r}_0^I(\mu)r_0^{II}(\mu)\right]}$$

$$=\frac{\dfrac{t_0^I(\mu)r_0^I(\mu)r_1^I(\mu)t_0^I(\mu+\Omega)e^{i2k(0)a}}{1-\left[r_0^I(\mu+\Omega)\right]^2e^{i2k(1)a}}}{1-\left[r_0^I(\mu)\right]^2e^{i2k(0)a}} \tag{B.21}$$

$$t\left(r_1^{II},\mu\right)=\frac{\dfrac{t_0^I(\mu)r_1^{II}(\mu)\tilde{r}_0^I(\mu+\Omega)t_0^{II}(\mu+\Omega)}{1-\left[r_0^{II}(\mu+\Omega)\tilde{r}_0^I(\mu+\Omega)\right]}}{1-\left[r_0^{II}(\mu)\tilde{r}_0^I(\mu)\right]}$$

$$=\frac{\dfrac{t_0^I(\mu)r_1^I(\mu)r_0^I(\mu+\Omega)t_0^I(\mu+\Omega)e^{i\left[k(1)+k(0)\right]a}}{1-\left[r_0^I(\mu+\Omega)\right]^2e^{i2k(1)a}}}{1-\left[r_0^I(\mu)\right]^2e^{i2k(0)a}} \tag{B.22}$$

$$t\left(t_{-1}^I,\mu\right)=\frac{t_{-1}^I(\mu)t_0^{II}(\mu-\Omega)}{1-r_0^{II}(\mu-\Omega)\tilde{r}_0^I(\mu-\Omega)}=\frac{t_{-1}^I(\mu)t_0^I(\mu-\Omega)}{1-\left[r_0^I(\mu-\Omega)\right]^2e^{i2k(-1)a}} \tag{B.23}$$

$$t\left(t_{-1}^{II},\mu\right)=\frac{t_0^I(\mu)t_{-1}^{II}(\mu)}{1-r_0^{II}(\mu)\tilde{r}_0^I(\mu)}=\frac{t_0^I(\mu)t_{-1}^I(\mu)e^{-i\left[k(-1)-k(0)\right]a}}{1-\left[r_0^I(\mu)\right]^2e^{i2k(0)a}} \tag{B.24}$$

$$t\left(\tilde{r}_{-1}^{I},\mu\right)=\frac{\dfrac{t_0^I(\mu)r_0^{II}(\mu)\tilde{r}_{-1}^I(\mu)t_0^{II}(\mu-\Omega)}{1-\left[r_0^{II}(\mu-\Omega)\tilde{r}_0^I(\mu-\Omega)\right]}}{1-\left[\tilde{r}_0^I(\mu)r_0^{II}(\mu)\right]}$$

$$=\frac{\dfrac{t_0^I(\mu)r_0^I(\mu)r_{-1}^I(\mu)t_0^I(\mu-\Omega)e^{i2k(0)a}}{1-\left[r_0^I(\mu-\Omega)\right]^2e^{i2k(-1)a}}}{1-\left[r_0^I(\mu)\right]^2e^{i2k(0)a}} \tag{B.25}$$

$$t\left(r_{-1}^{II},\mu\right)=\frac{\dfrac{t_0^I(\mu)r_{-1}^{II}(\mu)\tilde{r}_0^I(\mu-\Omega)t_0^{II}(\mu-\Omega)}{1-\left[r_0^{II}(\mu-\Omega)\tilde{r}_0^I(\mu-\Omega)\right]}}{1-\left[r_0^{II}(\mu)\tilde{r}_0^I(\mu)\right]}$$

$$=\frac{\dfrac{t_0^I(\mu)r_{-1}^I(\mu)r_0^I(\mu-\Omega)t_0^I(\mu-\Omega)e^{i\left[k(-1)+k(0)\right]a}}{1-\left[r_0^I(\mu-\Omega)\right]^2e^{i2k(-1)a}}}{1-\left[r_0^I(\mu)\right]^2e^{i2k(0)a}} \tag{B.26}$$

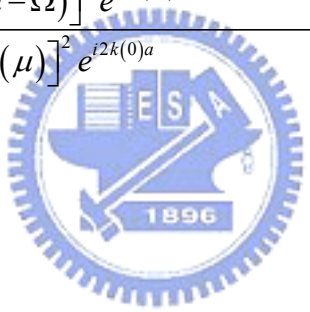

Appendix C

Analysis of Interference Terms of One-photon Approximation

In this section, we do some analysis of interference terms of Eq. (2.30) and (2.31) in Ch. 2. Eq. (2.30) gives

$$T_1(\mu)=\left|t\left(t_1^I,\mu\right)+t\left(t_1^{II},\mu\right)+t\left(\tilde{r}_1^I,\mu\right)+t\left(r_1^{II},\mu\right)\right|^2\frac{k(1)}{k(0)},$$

and Eq. (2.31) gives

$$T_{-1}(\mu)=\left|t\left(t_{-1}^I,\mu\right)+t\left(t_{-1}^{II},\mu\right)+t\left(\tilde{r}_{-1}^I,\mu\right)+t\left(r_{-1}^{II},\mu\right)\right|^2\frac{k(-1)}{k(0)}.$$

In addition,

$$\begin{aligned}&\left|t\left(t_1^I,\mu\right)+t\left(t_1^{II},\mu\right)+t\left(\tilde{r}_1^I,\mu\right)+t\left(r_1^{II},\mu\right)\right|^2\\&=\left(\left|t\left(t_1^I,\mu\right)\right|^2+\left|t\left(t_1^{II},\mu\right)\right|^2+\left|t\left(\tilde{r}_1^I,\mu\right)\right|^2+\left|t\left(r_1^{II},\mu\right)\right|^2\right)\\&+2\,\mathrm{Re}\left[t\left(t_1^I,\mu\right)t\left(t_1^{II},\mu\right)^*\right]+2\,\mathrm{Re}\left[t\left(t_1^I,\mu\right)t\left(\tilde{r}_1^I,\mu\right)^*\right]+2\,\mathrm{Re}\left[t\left(t_1^I,\mu\right)t\left(r_1^{II},\mu\right)\right]\\&+2\,\mathrm{Re}\left[t\left(t_1^{II},\mu\right)t\left(\tilde{r}_1^I,\mu\right)^*\right]+2\,\mathrm{Re}\left[t\left(t_1^{II},\mu\right)t\left(r_1^{II},\mu\right)^*\right]+2\,\mathrm{Re}\left[t\left(\tilde{r}_1^I,\mu\right)t\left(r_1^{II},\mu\right)^*\right]\end{aligned},$$

and

$$\begin{aligned}&\left|t\left(t_{-1}^I,\mu\right)+t\left(t_{-1}^{II},\mu\right)+t\left(\tilde{r}_{-1}^I,\mu\right)+t\left(r_{-1}^{II},\mu\right)\right|^2\\&=\left(\left|t\left(t_{-1}^I,\mu\right)\right|^2+\left|t\left(t_{-1}^{II},\mu\right)\right|^2+\left|t\left(\tilde{r}_{-1}^I,\mu\right)\right|^2+\left|t\left(r_{-1}^{II},\mu\right)\right|^2\right)\\&+2\,\mathrm{Re}\left[t\left(t_{-1}^I,\mu\right)t\left(t_{-1}^{II},\mu\right)^*\right]+2\,\mathrm{Re}\left[t\left(t_{-1}^I,\mu\right)t\left(\tilde{r}_{-1}^I,\mu\right)^*\right]+2\,\mathrm{Re}\left[t\left(t_{-1}^I,\mu\right)t\left(r_{-1}^{II},\mu\right)\right]\\&+2\,\mathrm{Re}\left[t\left(t_{-1}^{II},\mu\right)t\left(\tilde{r}_{-1}^I,\mu\right)^*\right]+2\,\mathrm{Re}\left[t\left(t_{-1}^{II},\mu\right)t\left(r_{-1}^{II},\mu\right)^*\right]+2\,\mathrm{Re}\left[t\left(\tilde{r}_{-1}^I,\mu\right)t\left(r_{-1}^{II},\mu\right)^*\right]\end{aligned}.$$

We know from Fig. 3.14 and 3.15 that $2\,\mathrm{Re}\left[t\left(t_1^I,\mu\right)t\left(\tilde{r}_1^I,\mu\right)^*\right]\frac{k(1)}{k(0)}$, and

$2\,\mathrm{Re}\left[t\left(t_1^I,\mu\right)t\left(r_1^{II},\mu\right)\right]\dfrac{k(1)}{k(0)}$ have the most effect on $\varepsilon_r-\Omega_1$ channel, while $2\,\mathrm{Re}\left[t\left(t_{-1}^I,\mu\right)t\left(\tilde{r}_{-1}^I,\mu\right)^*\right]\dfrac{k(-1)}{k(0)}$ and $2\,\mathrm{Re}\left[t\left(t_{-1}^I,\mu\right)t\left(r_{-1}^{II},\mu\right)\right]\dfrac{k(-1)}{k(0)}$ have the most (negative) effect on $\varepsilon_r+\Omega_1$ channel. We then do the analysis of these four interference terms. Acquiring the analytical expression for reflection and transmission coefficients in appendix B, we have

$$2\,\mathrm{Re}\left[t(t_1^I,\mu)t\left(\tilde{r}_1^I,\mu\right)^*\right]$$
$$=2\left[\frac{\left|t_0^I\left(\mu+\Omega\right)\right|^2}{\left|1-r_0^I\left(\mu+\Omega\right)^2e^{i2k(1)a}\right|^2}\frac{k(0)^2V_d^2}{\left|iV_s+2k(0)\right|^2\left|iV_s+2k(1)\right|^2}\right]\times\mathrm{Re}\left[\left(\frac{t_0^I(\mu)r_0^{II}(\mu)}{1-r_0^{II}(\mu)\tilde{r}_0^I}\right)^*\right], \quad (C.1)$$

$$2\,\mathrm{Re}\left[t(t_1^I,\mu)t\left(r_1^{II},\mu\right)^*\right]$$
$$=2\left[\frac{\left|t_0^I\left(\mu+\Omega\right)\right|^2}{\left|1-r_0^I\left(\mu+\Omega\right)^2e^{i2k(1)a}\right|^2}\frac{k(0)^2V_d^2}{\left|iV_s+2k(0)\right|^2\left|iV_s+2k(1)\right|^2}\right]\times\mathrm{Re}\left[\left(\frac{t_0^I(\mu)t_1^{II}(\mu)}{1-r_0^{II}(\mu)\tilde{r}_0^I(\mu)}\right)^*\right], \quad (C.2)$$

$$2\,\mathrm{Re}\left[t(t_{-1}^I,\mu)t\left(\tilde{r}_{-1}^I,\mu\right)^*\right]$$
$$=2\left[\frac{\left|t_0^I\left(\mu-\Omega\right)\right|^2}{\left|1-r_0^I\left(\mu-\Omega\right)^2e^{i2k(-1)a}\right|^2}\frac{k(0)^2V_d^2}{\left|iV_s+2k(0)\right|^2\left|iV_s+2k(-1)\right|^2}\right]\times\mathrm{Re}\left[\left(\frac{t_0^I(\mu)r_0^{II}(\mu)}{1-r_0^{II}(\mu)\tilde{r}_0^I}\right)^*\right], \quad (C.3)$$

and

$$2\,\mathrm{Re}\left[t(t_{-1}^I,\mu)t\left(r_{-1}^{II},\mu\right)^*\right]$$
$$=2\left[\frac{\left|t_0^I\left(\mu-\Omega\right)\right|^2}{\left|1-r_0^I\left(\mu-\Omega\right)^2e^{i2k(-1)a}\right|^2}\frac{k(0)^2V_d^2}{\left|iV_s+2k(0)\right|^2\left|iV_s+2k(-1)\right|^2}\right]\times\mathrm{Re}\left[\left(\frac{t_0^I(\mu)t_{-1}^{II}(\mu)}{1-r_0^{II}(\mu)\tilde{r}_0^I(\mu)}\right)^*\right]. \quad (C.4)$$

We do the analysis of the common factor,

$$\mathrm{Re}\left[\left(\frac{t_0^I(\mu)r_0^{II}(\mu)}{1-r_0^{II}(\mu)\tilde{r}_0^I}\right)^*\right],$$

of (C.1) and (C.3). Define

$$F = \frac{t_0^I(\mu) r_0^{II}(\mu)}{1 - r_0^{II}(\mu) \tilde{r}_0^I(\mu)} = \frac{-2ik(0) V_s e^{i2k(0)a}}{\left[2k(0) + iV_s\right]^2 \left[1 - r_0^I(\mu)^2 e^{i2k(0)a}\right]}. \quad \text{(C.5)}$$

After expansion and simplification, we have

$$\mathrm{Re}[F^*] = \frac{2V_s k\left[4k^2 \sin 2ak - V_s^2 \sin 2ak - 4kV_s \cos 2ak\right]}{2V_s^4(1-\cos 2ak) + 8k^2V_s^2(1+\cos 2ak) + 8kV_s^3 \sin 2ak + 16k^4}. \quad \text{(C.6)}$$

With $\beta \equiv 2ak$ and $\kappa \equiv aV_s$, Re[F^*] can be modified as

$$\frac{\kappa\beta\left[\left(\beta^2 - \kappa^2\right)\sin\beta - 2\kappa\beta\cos\beta\right]}{\left[2\kappa^2(1-\cos\beta) + 2\beta^2\kappa^2(1+\cos\beta) + 4\beta\kappa^3\sin\beta + \beta^4\right]} = \frac{f_n(\beta,\kappa)}{f_d(\beta,\kappa)}. \quad \text{(C.7)}$$

For V_s=3 and a=15, numerical plot of Eq. (C.7) is given in Fig. C.1.

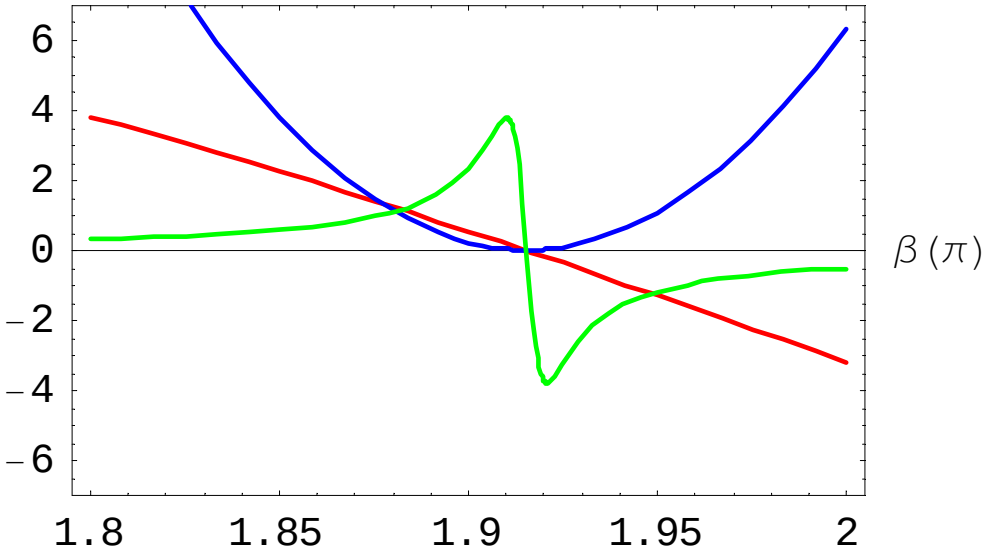

Fig. C.1. $\kappa = aV_s$=45. Green line is Re[F^*], blue one is $f_d(\beta,\kappa)$, and red one is $f_n(\beta,\kappa)$. Re[F^*]=0 when β=1.9153π, and this is the condition where resonance state is.

The lowest resonance state of double static barriers is β=2π when $V_s \to \infty$.

Thus, we start to look for the conditions where $f_n(\beta,\kappa) = 0$.

$$f_n(\beta,\kappa)=\left(\beta^2-\kappa^2\right)\sin\beta-2\kappa\beta\cos\beta=0$$
$$\Rightarrow \tan\beta=\frac{2\kappa\beta}{\beta^2-\kappa^2} \qquad \text{(C.8)}$$

Thus,

$$\mathrm{Re}[F^*]=0$$
$$\Rightarrow f_n(\beta,\kappa)=0 \quad .$$
$$\Rightarrow \tan\beta=\frac{2\kappa\beta}{\beta^2-\kappa^2}$$

We then try to find of the first-order correction term of $f_n(\beta,\kappa)$. Since the lowest resonance level is $\beta\sim 2\pi$. We start our approximation from $\beta_0=2\pi$. Setting

$\beta=\beta_0+\Delta\beta_n=2\pi+\Delta\beta_n$, then we have

$$f_n(\beta,\kappa)\approx$$
$$\left[\left(\beta_0^2+2\beta_0\Delta\beta_n\right)\left(\sin\beta_0+\cos\beta_0\Delta\beta_n\right)-\kappa^2\left(\sin\beta_0+\cos\beta_0\Delta\beta_n\right)-2\kappa\left(\beta_0+\Delta\beta_n\right)\left(\cos\beta_0-\sin\beta_0\Delta\beta_n\right)\right]$$
$$=\left[\beta_0^2\sin\beta_0-\kappa^2\sin\beta_0-2\beta_0\kappa\cos\beta_0\right]+\Delta\beta_n\left[\cos\beta_0\left(\beta_0^2-\kappa^2-2\kappa\right)+\sin\beta_0\left(2\beta_0+2\kappa\beta_0\right)\right]$$

Thus,

$$\text{for } f_n(\beta,\kappa)=0$$
$$\Rightarrow \Delta\beta_n=\frac{2\beta_0\kappa}{\beta_0^2-\kappa^2-2\kappa}\,.$$

Then we start to examine the first-order correction for β where $f_d(\beta)$ has its minimum value. Given that

$f_d(\beta,\kappa)=2\kappa^4\left(1-\cos\beta\right)+2\beta^2\kappa^2\left(1+\cos\beta\right)+4\beta\kappa^3\sin\beta+\beta^4$, then we have

$$f_d'(\beta,\kappa)=2\kappa^4\sin\beta+4\beta\kappa^2\left(1+\cos\beta\right)-2\beta^2\kappa^2\sin\beta+4\kappa^3\sin\beta+4\beta\kappa^3\cos\beta+4\beta^3\,.$$

For $\beta=\beta_0+\Delta\beta_d=2\pi+\Delta\beta_d$, and let $f'_d(\beta,\kappa)=0$, we have

$$f_d'(\beta,\kappa)=2\kappa^4\Delta\beta_d+4\left(\beta_0+\Delta\beta_d\right)\kappa^2\cdot 2-2\kappa^2\left(\beta_0^2+2\beta_0\Delta\beta_d\right)\Delta\beta_d+4\beta_0^3+12\beta_0^2\Delta\beta_d=0$$
$$\Rightarrow \Delta\beta_d=-\frac{2\beta_0^3+4\kappa^2\beta_0+2\kappa^3\beta_0}{\kappa^4+6\beta_0^2+4\kappa^2-\kappa^2\beta_0^2+4\kappa^3}$$

Under numerical calculation, we have

$\Delta\beta_n = -0.2725\pi$,

$\Delta\beta_d = -0.2676\pi$, and

$2\pi - \Delta\beta_n \sim 2\pi - \Delta\beta_d \sim 1.9153\pi$.

Hence, Thus, $f_n(\beta,\kappa)$ changes sign almost exactly when $f_d(\beta,\kappa)$ is at its minimum value. Leading factors of Eq. (C.1) to (C.4) are always positive. This is the main reason for different parity of contribution to total current transmission.

Reference

[1] R. Landauer, IBM J. Rex. Dev. **1**, 223 (1957).

[2] R. Landauer, Phil. Mag. **21**, 863 (1970).

[3] R. Landauer, Phys. Scr. T42, 110 (1992).

[4] M. Büttiker, Y. Imry, R. Landauer, and S. Pinhas, Phys. Rev. B **31**, 6207 (1985).

[5] M. Büttiker, Phys. Rev. Lett. **57**, 1761 (1986).

[6] M. Büttiker, Phys.Rev. B **38**, 9375 (1988).

[7] D. J. Thouless, Phys. Rev. B **27**, 6803 (1983).

[8] Q. Niu, Phys. Rev. Lett. **64**, 1812 (1990).

[9] P. W. Brouwer, Phys. Rev. Lett. **58**, R10 135 (1998).

[10] M. Switkes, C. M. Marcus, K. Campman, and A. C. Gossard, Science **283**, 1905 (1999).

[11] C. S. Tang and C. S. Chu, Solit State Commun. **120**, 353 (2001)

[12] S. W. Chung, C. S. Tang, C. S. Chu, and C. Y. Chang, Phys. Rev. B **70**, 085315 (2004)

[13] P. F. Bagwell and R. K. Lake, Phys. Rev. B **46**, 15 329 (1992).